PUBLICATIONS OF
THE UNIVERSITY OF EASTERN FINLAND

Dissertations in Science, Forestry and Technology

TIMOFEI EREMIN

Exciton dynamics in functionalized carbon nanotubes

Exciton dynamics in functionalized carbon nanotubes

Timofei Eremin

Exciton dynamics in functionalized carbon nanotubes

Publications of the University of Eastern Finland
Dissertations in Science, Forestry and Technology
No 62

University of Eastern Finland
Joensuu
2024

Academic dissertation
To be presented by permission
of the Faculty of Science, Forestry and Technology
for public examination in the Auditorium M100 in the Metria Building
at the University of Eastern Finland, Joensuu,
on 8 November 2024, at 12 o'clock noon

Punamusta Oy
Joensuu, 2024
Editor: Nina Hakulinen

ISBN: 978-952-61-5368-1 (Print)
ISBN: 978-952-61-5369-8 (PDF)
ISSNL: 2954-131X
ISSN: 2954-131X (Print)
ISSN: 2954-1484 (PDF)

Author's address: Timofei Eremin
University of Eastern Finland
Depart. of Physics and Mathematics
P.O. Box 111
80101 Joensuu, Finland
email: timofei.eremin@uef.fi

Supervisors: Academy Research Fellow, Ph.D. Petr Obraztsov
University of Eastern Finland
Depart. of Physics and Mathematics
P.O. Box 111
80101 Joensuu, Finland
email: petr.obraztsov@uef.fi

Professor Yuri Svirko, Ph.D.
University of Eastern Finland
Depart. of Physics and Mathematics
P.O. Box 111
80101 Joensuu, Finland
email: yuri.svirko@uef.fi

Reviewers: Professor Louise Bradley, Ph.D
School of Physics and CRANN, Trinity College Dublin,
Dublin, Ireland
email: louise.bradley@tcd.ie

Assistant Professor Yusong Bai, Ph.D
Brown University, Department of Chemistry,
Providence, USA
email: yusong_bai@brown.edu

Opponent: Professor Harri Lipsanen, Ph.D
Aalto University
Depart. of Electronics and Nanoengineering
P.O. Box 1000, 00076 AALTO, FINLAND
email: harri.lipsanen@aalto.fi

Eremin, Timofei
Exciton dynamics in functionalized carbon nanotubes
Joensuu: University Of Eastern Finland, 2024
Publications of the University of Eastern Finland
Dissertations in Science, Forestry and Technology; 62
ISBN: 978-952-61-5368-1 (Print)
ISBN: 978-952-61-5369-8 (PDF)
ISSNL: 2954-131X
ISSN: 2954-131X (Print)
ISSN: 2954-1484 (PDF)

ABSTRACT

Single-walled carbon nanotubes have diverse applications in telecommunications, quantum technologies, biosensing, and more, owing to their broad light emission and absorption capabilities. However, their low photoluminescence efficiency poses a significant challenge. Recent research focuses on localizing excitons within artificial traps to enhance photoluminescence brightness and exploit benefits like photon antibunching. Despite progress, challenges persist in the development of efficient, simple, and scalable techniques of integrating these traps into nanotubes and understanding fundamental processes taking place in such unique structures. This study focuses on investigating the structure of energy levels within localizing potentials, including both the energy arrangements and the physical nature of these states. It also aims to propose improved methods for integrating localizing potentials into carbon nanotubes and to examine the interaction processes of photoexcited excitons with these potentials.

Keywords: single-walled carbon nanotubes, doping, quantum defects, exciton, ultrafast dynamics, photoluminescence, transient absorption

Acknowledgements

This work would not have been done without the support and contributions of many individuals who helped me at various stages of my research and dissertation writing process.

First and foremost, I would like to express my deepest gratitude to my supervisors, Petr Obraztsov and Yuri Svirko, whose expertise, guidance, and unwavering support have been invaluable throughout this research process. I am particularly thankful to Petr Obraztsov for securing the funding necessary for this work.

I am also grateful to the Department of Physics and Mathematics of the University of Eastern Finland and particularly Jyrki Saarinen for providing the resources and facilities essential for conducting my research. My sincere appreciation goes to the scientific and technical staff of the university, especially Pertti Pääkkönen, Igor Reduto, Petri Karvinen, Tommi Itkonen, Sari Suvanto and many others for their help in mastering experimental equipment and solving engineering and design problems. I extend my thanks to the university's administrative staff, particularly Katri Mustonen, Noora Heikkilä, and Hannele Karppinen for their assistance with organizational matters, which allowed me to focus on scientific challenges.

I would like to acknowledge and thank all the co-authors of the published works for their valuable contributions.

Joensuu, 25 September 2024
Timofei Eremin

LIST OF ABBREVIATIONS

SWCNT	single-walled carbon nanotube
PL	photoluminescence
TA	transient absorption
NIR	near-infrared
UV	ultraviolet
PSB	phonon side band
SDS	sodium dodecyl sulfate
O-SWCNT	oxygen-functionalized single-walled carbon nanotubes
SPS	single photon source
OPA	optical parametric amplifier
CW	continuous wavelength
LED	light emitting diode
RBM	radial breathing mode
Ti:Sa	Titanium-sapphire
HCl	hydrochloric acid

LIST OF ORIGINAL PUBLICATIONS

This thesis is based on data presented in the following articles, referred to by the Roman Numerals I-III.

I Eremin, T.V., Obraztsov, P.A., Velikanov, V.A., Shubina, T.V. & Obraztsova, E.D. (2019). Many-particle excitations in non-covalently doped single-walled carbon nanotubes, *Scientific Reports*, 9, 1-8.

II Eremin, T., Eremina, V., Svirko, Y., & Obraztsov, P. (2023). Over Two-Fold Photoluminescence Enhancement from Single-Walled Carbon Nanotubes Induced by Oxygen Doping. *Nanomaterials*, *13*(9), 1561.

III Eremin, T., Dhama, R., Caglayan, H., & Obraztsov, P. (2024). Ultrafast exciton trapping dynamics in oxygen-functionalized single-walled carbon nanotubes. *Carbon*, 220, 118837.

The above publications have been included at the end of this thesis. No permissions from copyright holders or publisher are needed for reuse, reproduction or reprint of the mentioned articles.

AUTHOR'S CONTRIBUTION

I) Idea generation (with coauthors), experiment design (with coauthors), samples preparation, photoluminescence, Raman and static absorption measurements, data analysis (with coauthors), writing the original draft of the manuscript.

II) Idea generation (with coauthors), experiment design, samples preparation (with coauthors), photoluminescence, Raman and static absorption measurements, data analysis, writing the original draft of the manuscript.

III) Idea generation, experiment design (with coauthors), samples preparation, photoluminescence, Raman and static absorption measurements, pump-probe measurements (with coauthors), data analysis, writing the original draft of the manuscript.

Table of contents

INTRODUCTION **15**

1 Literature overview **17**

1.1 The crystal and band structure of single walled carbon nanotubes 17

1.2 Excitonic effect in single walled carbon nanotubes 19

1.3 Optical properties of single walled carbon nanotubes 22

1.3.1 Raman scattering 22

1.3.2 Light absorption 24

1.3.3 Photoluminescence 26

1.3.3 Relaxation dynamics of photoexcitations 29

1.4 Trapped quantum states in doped and functionalized single walled carbon nanotubes 32

1.4.1 Quantum traps fabrication methods 32

1.4.2 The structure of energy levels in quantum traps 33

1.4.3 Dynamics of photoexcitations in single walled carbon nanotubes with quantum traps 34

1.4.4 Progress in creating single-photon sources based on single walled carbon nanotubes with quantum defects 35

1.4.5 Problems, tasks, and open questions. 38

2 Materials, Measurement techniques and Experimental methods 39

2.1 Preparation of the suspensions of single walled carbon nanotubes with high optical quality 39

2.2 Doping and functionalization of single walled carbon nanotubes 40

2.3 Optical absorption spectroscopy 40

2.4 Raman spectroscopy 42

2.5 Photoluminescence spectroscopy 42

2.6 Ultrafast transient absorption spectroscopy 43

3 Non-covalent doping of single walled carbon nanotubes in acid medium 45

3.1 Photoluminescence studies 45

3.2 Optical absorption studies 53

3.3 Raman spectroscopy studies 55

3.4 The mechanism of single walled carbon nanotubes doping via addition of HCl..... 57
3.5 Ultrafast transient absorption spectroscopy studies..... 58
3.6 Discussion on the physical nature of doping induced energy levels in carbon nanotubes doped with HCl..... 65

4 Functionalization of single walled carbon nanotubes with oxygen quantum defects..... 69
4.1 Photoluminescence studies..... 69
4.2 Determination of optimum parameters of oxygen functionalization 70
4.3 Comparison of photoluminescence brightening efficiency to previously reported data..... 72
4.4 Discussion on the reason for the advanced PL intensity enhancement 76
4.5 Ultrafast exciton dynamics in oxygen-functionalized single-walled carbon nanotubes..... 81

CONCLUSION..... 93

BIBLIOGRAPHY..... 95

Appendices..... 109

ARTICLES..... 121

INTRODUCTION

Single-walled carbon nanotubes (SWCNTs) are cylindrical nanostructures with diameters typically between 0.5 to 2 nanometers and lengths ranging from hundreds of nanometers to several micrometers. Their walls consist of a single layer of carbon atoms arranged in a hexagonal lattice. This unique crystalline structure of SWCNTs gives rise to their distinct electronic and optical properties. In particular, they can both emit and absorb light across a range of wavelengths, from 700 to 2500 nanometers, depending on their diameter and chiral angle—the angle between the zigzag direction and the circumference of the carbon nanotube.

Since SWCNT are optically active in such a broad spectral range, they are considered as a promising material for numerous applications in such fields as telecommunications, bioimaging, and single-photon generation for quantum technologies. This potential has sustained a high level of interest in SWCNTs within the scientific community for nearly three decades.

One of the major challenges hindering the widespread use of SWCNTs is their relatively low efficiency of light emission. This is primarily due to the peculiar structure of excitonic energy levels within SWCNTs, where the lowest energy level is "dark," meaning that radiative recombination is restricted by selection rules for excitons at this level. Additionally, defects within SWCNTs act as centers that quench fluorescence, further reducing light emission efficiency.

In recent years, researchers have been actively developing methods to address this challenge by localizing excitons within artificially created potential traps. By confining excitons within these traps, their movement along the SWCNT is restricted, preventing them from reaching fluorescence quenching centers. Additionally, exciton trapping may also alter energetic arrangements of excitonic states and even rearrange bright and dark exciton states, potentially enhancing the efficiency of light emission.

Exciton localization provides several benefits beyond improving light emission efficiency. These include photon antibunching, which allows

SWCNTs to act as single-photon sources. Additionally, the spectral separation of absorption and emission bands in SWCNTs with trapping defects simplifies achieving population inversion for ultracompact SWCNT-based lasers and enhances the performance of these SWCNTs as fluorescent markers in bioimaging.

Even with these advancements, there are still major obstacles to overcome before SWCNTs with localized traps can be effectively used in real-world applications. This includes developing straightforward, scalable methods to incorporate trapping defects into SWCNT structures and gaining a deeper understanding of exciton interactions with these traps.

This study aims to address these challenges by investigating the structure of energy levels within localizing potentials (Chapter 3), proposing improved methods for integrating localizing potentials into SWCNTs and examining the interaction processes of excitons with localizing sites within SWCNTs (Chapter 4). The discussion of the results is preceded by a comprehensive review of relevant literature (Chapter 1) and a description of the experimental techniques employed (Chapter 2).

1 Literature overview

1.1 The crystal and band structure of single walled carbon nanotubes

A single-walled carbon nanotube (SWCNT) is a hollow cylindrical crystalline structure with a diameter on the order of 1-2 nanometers. [1] The length of an SWCNT exceeds its diameter by several orders of magnitude and, depending on the synthesis method and post-synthesis treatment, can range from hundreds of nanometers to hundreds of millimeters, allowing SWCNTs to be considered quasi-one-dimensional objects. [2] The wall of an SWCNT consists of a single layer of carbon atoms in sp^2 hybridization, and the ends of an SWCNT can either be capped with hemispherical "caps," resembling half of a fullerene molecule, or left open. [3]

The physical properties of SWCNTs are determined by their geometric structure. To describe this relationship, one can exploit zone-folding approximation according to which SWCNT is represented as a rolled-up graphene sheet at specific angles with certain widths (see Fig. 1.1a) [4][5]. In this model, the coordinates (n, m) of the chiral vector $\overrightarrow{C_h}$ in the basis of vectors $\overrightarrow{a_1}$ and $\overrightarrow{a_2}$ fully determine the geometric structure of the SWCNT, including its diameter d_t, the number of atoms in the unit cell, and so on (see Fig. 1.1b). [1][6]

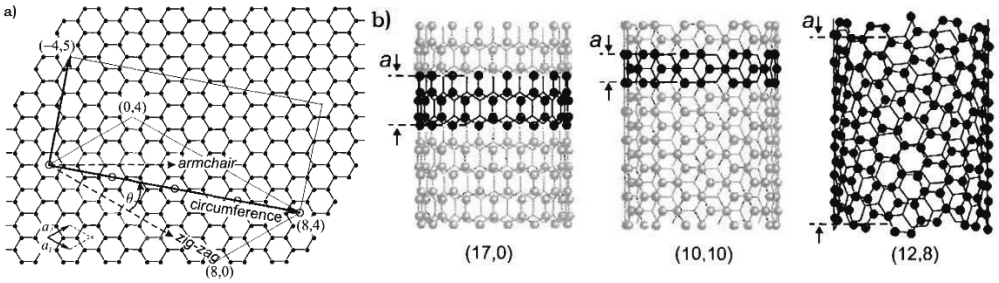

Figure 1.1. a) Illustration of the structural relationship between graphene and SWCNTs. b) Schematic representation of SWCNTs of different geometries: Bold-colored elementary cells are highlighted. Arrows denote translation vectors $\vec{T}$. Reprinted with permission from [1]

The direction perpendicular to the chiral vector C_h is the direction of translational symmetry in SWCNTs. The smallest lattice vector of graphene in this direction determines the translation period ($\vec{T}$ in Fig. 1.1). The primitive vectors of SWCNTs in reciprocal space, $\overrightarrow{K_c}$ и $\overrightarrow{K_T}$, are determined by the conditions $\overrightarrow{K_c} * \overrightarrow{C_h} = 2\pi,\ \overrightarrow{K_c} * \vec{T} = 0,\ \overrightarrow{K_T} * \vec{T} = 2\pi,\ \overrightarrow{K_T} * \overrightarrow{C_h} = 0$, and are also expressed in terms of the chiral indices (n, m). [1][6]

Due to the boundary conditions along the chiral vector direction, the projection of the wave vector $\vec{K}$ in this direction can only take values of μK_c where μ is an integer from the segment $[-\frac{N}{2}+1;\frac{N}{2}]$., thus having a discrete spectrum. Conversely, the projection of the wave vector onto the direction of translational symmetry has a continuous spectrum in the segment $[-\frac{\pi}{T};\frac{\pi}{T}]$ for an infinitely long SWCNT model. [1]

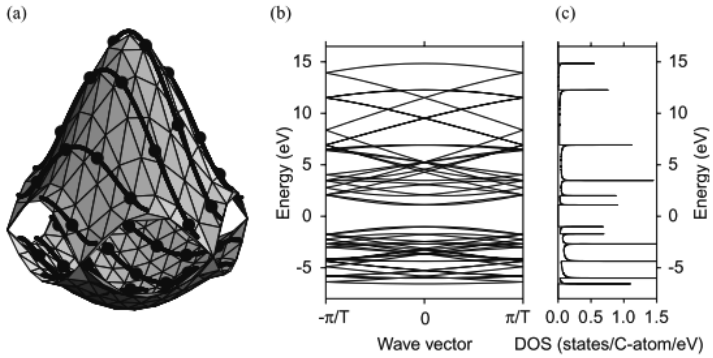

Figure 1.2. a) Dispersion surface of graphene with overlaid cut lines. b) Example set of dispersion curves of a semiconductor SWCNT. c) corresponding density of states. Reprinted with permission from [6]

In a simplified approach, the electron dispersion law $E_\mu(k)$ in SWCNTs can be derived from graphene's by folding the zone [7], considering the mentioned wave vector constraints. Figure 1.2a schematically illustrates the cut lines of graphene's dispersion surface for various μ values. The chiral indices (n, m) determine these lines on the dispersion surface, hence shaping the electronic structure of SWCNTs. Notably, when (n-m) is divisible by 3 without remainder, the cut line passes through graphene's K-point, rendering the SWCNT metallic; otherwise, it behaves as a semiconductor [8]. (see Fig. 1.2b) Many unique optical properties of SWCNTs are linked to

narrow peaks in the density of electronic states (see Fig. 1.2c), known as Van Hove singularities, which arise due to SWCNTs' one-dimensional nature.

1.2 Excitonic effect in single walled carbon nanotubes

The one-dimensional structure of SWCNTs results in weak screening of the Coulomb potential, necessitating the consideration of electron-electron interactions in describing their physical properties [9], [10]. Such interactions lead to electrons and holes in SWCNTs existing as bound states called excitons, which significantly influence many optical properties of SWCNT [11].

Both theoretical and experimental studies indicate that the exciton binding energy in SWCNTs is on the order of hundreds of meV, which constitutes a significant portion of the bandgap of SWCNTs [12], [13], [14]. Thus, unlike in bulk semiconductors, excitonic effects in SWCNTs can be observed even at room temperature.

Excitonic states in SWCNTs that can recombine with photon emission or be optically excited upon photon absorption are called bright excitons. Other excitonic states cannot participate in such optical transitions due to reasons discussed below and are termed dark excitons. [15]

The spectrum of excitonic states in SWCNTs exhibits a complex structure. In the first approximation, it consists of a set of energy levels E_{ij}, where the indices *i* and *j* denote the numbers (counting from the K or K' point) of the cut lines in the valence and conduction bands of graphene on which the electron and hole are located. [5] Only states with *i=j* correspond to direct optical transitions. [16] Each of these excitonic levels E_{ij} splits into 4 sub-levels depending on the valleys in which the electron and hole are situated (see Fig. 1.3). [17]

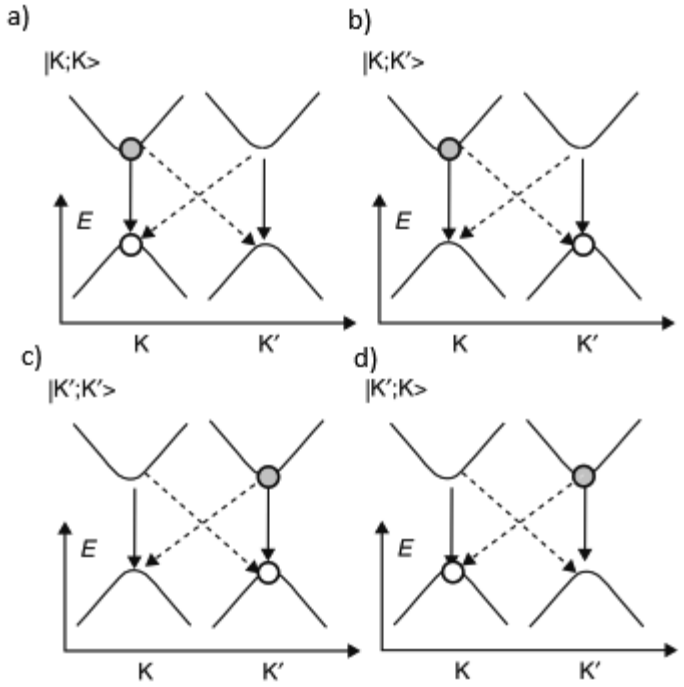

Figure 1.3 Various configurations of electron-hole pairs in SWCNT forming excitons. Reprinted with permission from [17]

If the electron and hole are in different valleys (Fig. 1.3a, b), the excitons correspond to an indirect optical transition and are called K-momentum dark excitons. [17] However, if both the electron and the hole are situated in the K (or K') valley, then two possible eigenstates of the exciton, denoted as A_p are obtained by mixing the states $\psi_{K'}$ (Fig. 1.3c) and ψ_K (Fig. 1.3d). [16]

$$A_2 = \frac{1}{\sqrt{2}}\left(\psi_K + \psi_{K'}\right), \tag{1}$$

$$A_1 = \frac{1}{\sqrt{2}}\left(\psi_K - \psi_{K'}\right). \tag{2}$$

Of these two states, only A_2 can be bright, as state A_1 is dark due to symmetry-related selection rules. If the electron and hole spins are anti-parallel, the exciton spin S equals 0, indicating a singlet exciton that can be bright. Conversely, if the electron and hole spins are parallel, S=1, resulting

in a triplet state, which is dark. State A_1 has the same anergy for S=0 and S=1 cases, while state A_2 splits into singlet and triplet states. [16]

To identify a specific excitonic band, we use the notation $E_{ii}^{s}(A_p^{\nu})$. The indices S, p, and i represent spin, parity, and the graphene cutting line to which the electron and hole belong, respectively (see Fig. 1.4). Each exciton characterized by the triplet of indices S, p, and i can occupy a set of levels indexed by the quantum number ν, which is analogous to the principal quantum number n in a hydrogen atom. [18] The energy of the exciton at each $E_{ii}^{s}(A_p^{\nu})$ band varies with the momentum of the electron-hole center of mass $\overrightarrow{K_{ex}}$, reflecting the exciton's overall translational motion. [16]

In Fig. 1.4a, b, c, excitonic dispersion curves computed in [18] for a (6,5) SWCNT are depicted. Excitonic states with $\overrightarrow{K_{ex}}$ close to 0 correspond to direct optical transitions and can be bright, while states with $K_{ex} \neq 0$ correspond to indirect optical transitions and are dark. [18]

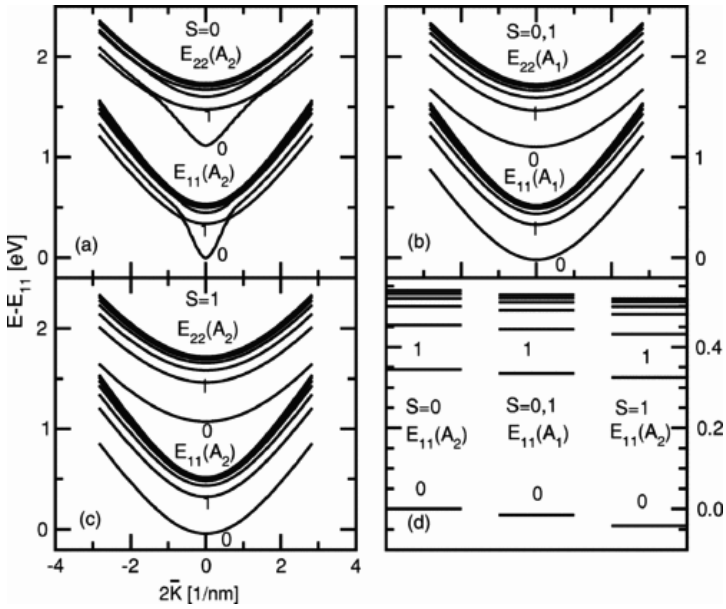

Figure 1.4 a, b, c) Exciton dispersion curves in a (6,5) SWCNT. d) Structure of excitonic states with $K_{ex} = 0$. Reprinted with permission from [18]

In Fig. 1.4d, the energy levels of excitons at $K_{ex} = 0$ are presented relative to the energy level $E_{11}^{0}(A_2^{0})$ of the exciton. A distinguishing feature of SWCNTs is that dark excitonic states $E_{11}^{1}(A_2^{0})$, $E_{11}^{1}(A_1^{0})$, $E_{11}^{0}(A_1^{0})$, lie energetically lower than the bright excitonic state $E_{11}^{0}(A_2^{0})$. However, it should be noted that

the K-momentum dark exciton from the set E_{11} lies energetically higher than the bright excitonic state $E_{11}^0(A_2^0)$. [18]

For convenience, in the subsequent text, the excitonic states $E_{ii}^0(A_2^0)$ will be referred to as bright excitons, $E_{ii}^1(A_2^0)$ as dark triplet excitons, and $E_{ii}^1(A_1^0)$ and $E_{ii}^0(A_1^0)$) as dark singlet excitons.

1.3 Optical properties of single walled carbon nanotubes

1.3.1 Raman scattering

Raman spectroscopy stands out as a widely used method within laser spectroscopy, extensively employed in the study of SWCNTs. [6] A distinctive spectroscopic hallmark enabling the identification of SWCNT presence within a sample is the radial breathing modes (RBMs), indicative of the collective oscillations of carbon atoms along the radial axis (see Fig. 1.5b).[19] These low-frequency vibrations are discernible within Raman spectra within the frequency range of 100-400 cm^{-1}. The frequency w_{rbm} of the RBM mode can be expressed empirically as a function of the SWCNT diameter

$$w_{rbm} = \frac{A}{d_t} + B, \tag{3}$$

where d_t is expressed in nanometers, w_{rbm} in cm^{-1}, A and B are parameters dependent on the environment surrounding the SWCNT. [20] For instance, for SWCNTs in bundles, experimentally determined values are A = 234 and B = 10 [21]. In Raman spectra of SWCNT ensembles, RBM modes can merge into broad bands. The line width is determined by the distribution width of SWCNT diameters present in the sample. Such sensitivity of RBM modes to SWCNT structure makes Raman spectroscopy in the corresponding frequency range a convenient tool for assessing the distribution of SWCNTs in the sample by diameter. [20] It is important to note that SWCNTs with absorption bands that match the excitation laser photon energy contribute disproportionately to the final Raman scattering spectrum compared to other SWCNTs. Consequently, varying the excitation laser's wavelength can provide more detailed information about the SWCNT

material by selectively probing different diameter fractions of the SWCNTs. [22]

The tangential mode of graphene active in Raman scattering (G-mode) resonates at 1582 cm^{-1}.[23] Different configurations of tangential vibrations within SWCNTs can appear as distinct bands in Raman spectra. Symmetry breaking occurs when graphene folds into SWCNTs, lifting the degeneracy between the two most intense tangential modes known as G+ and G-. Specifically, the G+ mode reflects atomic vibrations along the axis of the SWCNT, while the G- mode corresponds to vibrations along the folding direction (see Fig. 1.5a). [6]

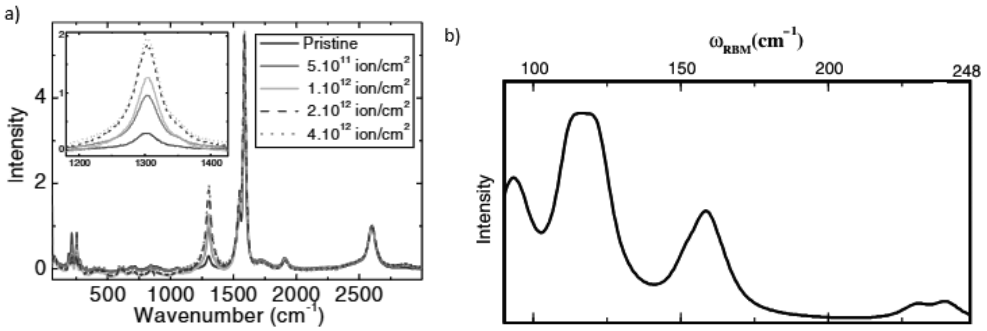

Figure 1.5 a) The growth of the defect mode in RS (~1300 cm^-1) while maintaining the tangential mode in RS (~1590 cm^-1) due to increased defectiveness of SWCNTs under Ar+ ion bombardment. reprinted with permission from [24]. b) Calculated RS spectrum in the region of RBM modes in a sample containing an equal number of SWCNTs of each geometry at an excitation energy of 1.58 eV. Reprinted with permission [25].

Another characteristic feature of SWCNTs in Raman spectra is the defect mode (D-mode), which indicates the presence of defects in SWCNT structure [26]. In Raman spectra, the D-mode appears as a peak around 1300 cm^{-1} (see Fig. 1.5a).

Because the intensity of the G-mode correlates with the concentration of carbon atoms, while the intensity of the D-mode reflects the concentration of defects in SWCNT structure, the ratio of these peak intensities is often used to gauge the degree of SWCNT defectiveness. This defectiveness is influenced by both the method of SWCNT synthesis and post-synthesis treatments: aggressive chemical environments, high

temperatures, oxidation, and so forth, typically contribute to increased SWCNT defectiveness [27].

1.3.2 Light absorption

Figure 1.6 depicts the absorption spectra in samples of SWCNTs synthesized using chemical vapor deposition (CVD) methods (Fig. 1.6a, b) and the high-pressure carbon monoxide decomposition (HiPCO) growth method (Fig. 1.6c, d) [28]. Absorption peaks in the range of 1000-1500 nm correspond to excitonic transitions $E_{11}(A_2^0)$ in SWCNTs of various geometries present in the samples, while peaks in the range of 500-1000 nm correspond to excitonic transitions $E_{22}(A_2^0)$. As noted earlier, the energy of excitonic transitions depends on the diameter and chiral indices (n,m) of SWCNTs, allowing the distribution of SWCNTs in the samples by diameter to be estimated from the optical absorption spectrum [29]. In all cases presented in Figure 1.6, SWCNTs in the samples have a diameter of about 1 nm. The differences in the spectra are due to variations in the distribution of SWCNTs in the samples by diameter and chiral indices, depending on the method of SWCNT synthesis.

In addition to the synthesis methods of SWCNTs, the absorption spectrum is also significantly influenced by interactions between neighboring SWCNTs aggregated into bundles [31]. In the absorption spectrum of SWCNT film (Fig. 1.6a), where nanotubes are predominantly in bundles, as well as in the absorption spectrum of SWCNT suspension, where nanotube bundles are present (Fig. 1.6d), broad absorption bands are observed. In spectra of samples where SWCNTs are isolated from each other using surfactants (Fig. 1.6b, c), sets of narrow, well-resolved peaks are observed, each corresponding to a specific SWCNT geometry. The substantial difference in the absorption spectra of isolated SWCNTs and SWCNT bundles is due to spectral broadening of optical transitions in SWCNTs interacting with neighboring nanotubes.

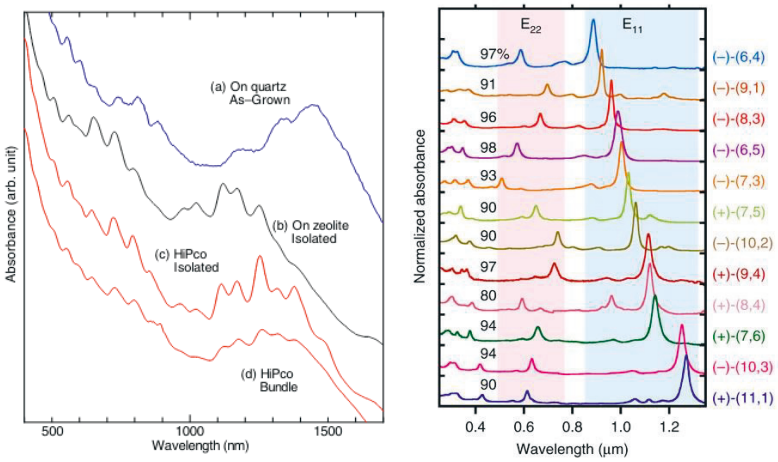

Figure 1.6 Left panel: Absorption spectra of SWCNT samples obtained by different methods: a) CVD SWCNT film on a quartz substrate, b) isolated CVD SWCNTs on a zeolite substrate, c) isolated HiPCO SWCNTs in suspension, d) HiPCO SWCNT bundles in suspension. Reprinted with permission from [28] Right panel: Absorption spectra of nearly monochiral SWCNT suspensions obtained through advanced gel column chromatography as a post-synthesis treatment. Reprinted with permission from[30]

Advanced techniques in SWCNT synthesis and post-synthesis treatment result in nearly monochiral SWCNT samples, with their optical absorption spectra shown in the right panel of Figure 6. Optical absorption in SWCNTs is also influenced by the interaction between excitons and phonons. Specifically, simultaneous optical excitation of a K-point dark exciton and a K-point phonon is possible, leading to the emergence of phonon sideband (PSB) peaks in the absorption spectra, which have energy of approximately 200 meV higher than bright E_{11} transition. [32], [33], [34] [32], [33], [34] These PSB peaks are clearly seen in the right panel of Figure 6 as broad peak between prominent sharp E_{11} and E_{22} peaks.

The absorption cross-section at resonant excitation of the E_{22} exciton in SWCNT bundles is approximately 10^{-18} cm^2 per carbon atom [35], [36]. For isolated SWCNTs, this value is usually 1-2 orders of magnitude higher [37], [38], [39], [40], [41], presumably due to the narrower absorption line of isolated SWCNTs.

1.3.3 Photoluminescence

Photoluminescence (PL) in semiconductor SWCNTs involves radiative recombination of the bright E_{11} exciton accompanied by photon emission following optical excitation of the SWCNT. This excitation can be resonant provided that the energy of the excitation radiation is close to the energy of one of the higher excitonic levels with a significant oscillator strength, such as E_{22} or E_{33}.

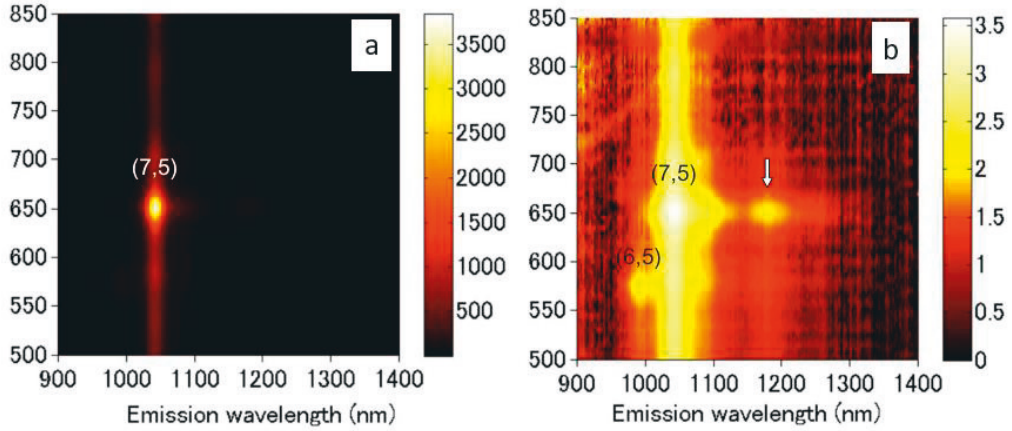

Figure 1.7 PL map of polyfluorene-SWCNT suspension/toluene. The color represents the intensity of PL in a) linear and b) logarithmic scale. Reprinted with permission from [43]

One commonly used method of PL spectroscopy is PL mapping, where PL spectra are acquired at several different excitation wavelengths, ultimately allowing the generation of a colour map where the intensity of PL, represented by colour, is plotted as a function of excitation and emission wavelengths (or energies).

In Figure 1.7a, a PL map of a suspension of SWCNTs in toluene is presented, predominantly containing (7,5)-chirality SWCNTs [42]. The prominent peak with an emission wavelength around 1050 nm corresponds to the radiative recombination of the bright E_{11} exciton. The intensity of this peak reaches its maximum at an excitation wavelength of 650 nm, which corresponds to resonant excitation of the E_{22} exciton. At other excitation wavelengths, the PL brightness is substantially lower, as non-resonant excitation of PL occurs.

A more diverse set of spectral features can be observed when using a logarithmic scale for PL intensity (Fig. 1.7b). Firstly, the peak from (6,5)-chirality SWCNTs becomes noticeable, although their concentration in this sample is significantly lower than that of (7,5)-chirality SWCNTs. Secondly, a weak signal with an emission wavelength around 1180 nm is observed, resonant with the excitation matching E_{11}(7,5). This spectral feature is called a phonon sideband (PSB) emission and corresponds to the radiative recombination of a dark K-point exciton, made possible by the involvement of another particle — a phonon located at the Brillouin zone boundary (K-point phonon) — which imparts the momentum necessary to satisfy the momentum conservation law (Fig. 1.8a). In addition to K-point phonons, other phonons can also participate in similar processes (Fig. 1.8b). For example, sideband phonon peaks are observed, corresponding to the interaction of excitons with tangential phonons, and presumably with radial breathing phonons as well [44].

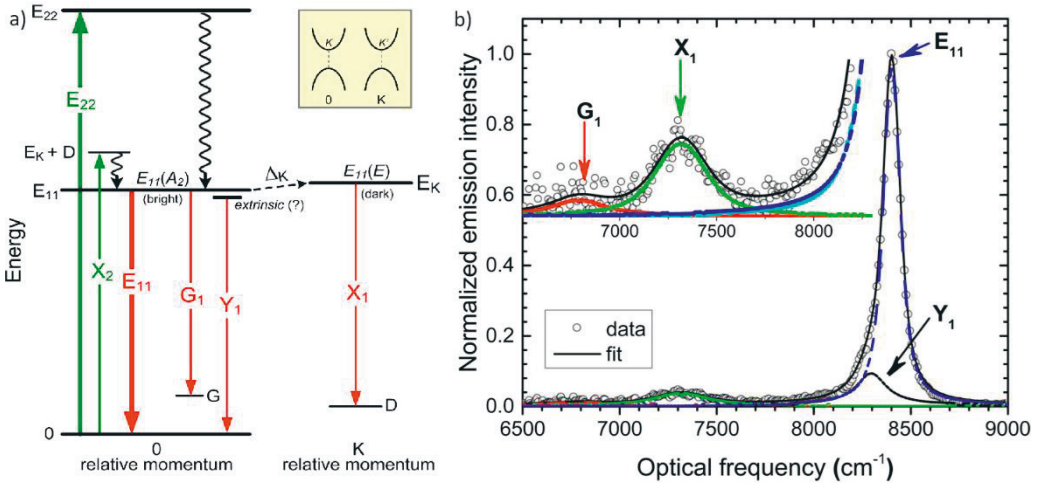

Figure 1.8 a) Schematic representation of the energy levels and optical transitions responsible for PSB peaks. b) PL spectrum with labeled PSB peaks associated with RB, tangential, and defect phonons. Reprinted with permission from [44].

These coupled exciton-phonon states were theoretically predicted in a study [45]. Direct experimental confirmation of the nature of these spectral features was achieved by comparing differences in the Raman spectra and PL maps of regular SWCNTs and SWCNTs composed of the ^{13}C isotope (^{13}SWCNTs) [32]. It was found that both the positions of the sideband phonon peaks in the PL maps of ^{13}SWCNTs and the positions of the peaks in

the Raman spectra of ^{13}SWCNTs could be obtained from those of regular SWCNTs by considering a factor of √(12/13), reflecting the difference in the masses of carbon atoms in regular SWCNTs and ^{13}SWCNTs.

Since electron-electron and electron-hole interactions largely determine the optical properties of SWCNTs, the energy of optical transitions is sensitive to changes in the dielectric constant of the medium directly surrounding the SWCNTs due to aggregation [46], formation of surfactant micelles around SWCNTs [47], [48], [49], and so on. Typically, in such cases, a redshift is observed in the spectroscopic features compared to isolated SWCNTs suspended in vacuum [42], [46], [47], [48], [50], [51].

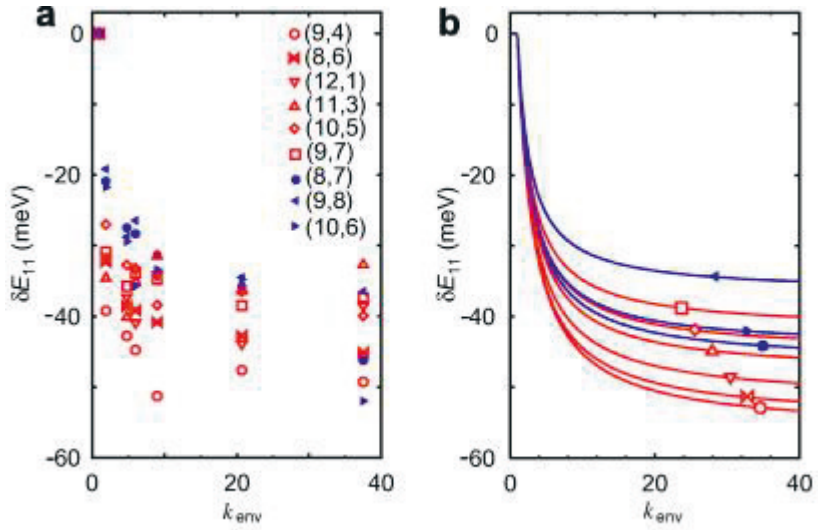

Figure 1.9 Experimental (a) and theoretical (b) dependencies of the change in energy of the E_{11} exciton on the dielectric constant of the medium. Reprinted with permission form [51]

In Figure 1.9, both experimental and theoretical dependencies of the energy of the E_{11} exciton in individual suspended SWCNTs on the dielectric constant of the surrounding medium are presented [51]. The model, where Coulomb interaction screening was considered as a linear combination of screening by the tube itself and the surrounding medium, qualitatively reproduces the experimental results: even with the same dielectric constant value of the surrounding medium, different geometries of SWCNTs exhibit distinct shifts in the position of the excitonic peak.

The PL peaks of even well-isolated SWCNT ensembles are significantly broadened due to the heterogeneous influence of the local environment on individual nanotubes. Figure 1.10 shows the PL spectra of a single SWCNT suspended over a slit in a substrate and an ensemble of SWCNTs dissolved in gelatin. Compared to the PL peaks of a single SWCNT, the PL peaks of the SWCNT ensemble are markedly heterogeneous, reflecting the high sensitivity of SWCNT PL to local environmental effects and the heterogeneity of the local environment for different SWCNTs in the ensemble [52].

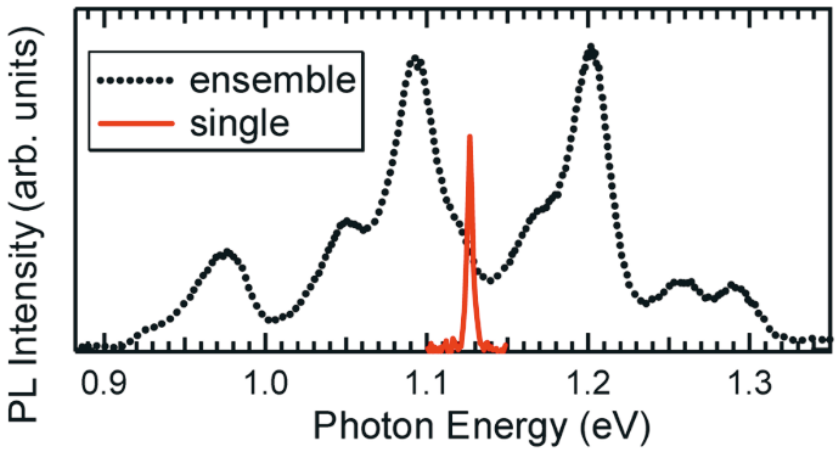

Figure 1.10 PL spectra of an ensemble of SWCNTs (a) and a single SWCNT (b). Reprinted with permission form [52]

1.3.3 Relaxation dynamics of photoexcitations

Like other optical properties of semiconductor SWCNTs, the dynamics of photoexcitation relaxation in this material are strongly influenced by the excitonic effect. The relaxation dynamics of excitons in semiconductor SWCNTs are determined by the interaction of excitons with phonons, defect and impurity potentials, free carriers, as well as with other excitons.

Intraband relaxation of excitons from the E_{22} level to the E_{11} level mainly occurs due to scattering on phonons with characteristic timescales in the subpicosecond range [53], [54], [55], [56], [57], [58].

Interband relaxation of the exciton from the E_{11} level to the ground state can occur either as radiative recombination with photon emission in the near-infrared range or as non-radiative relaxation. The exciton lifetime with respect to radiative recombination is on the order of tens of nanoseconds [59], [60], [61], whereas the characteristic timescales for non-radiative recombination typically lie in the picosecond range [55], [62], [63], [64]. This is associated with the extremely low PL QY of SWCNTs, which for a suspension of individual SWCNTs stabilized with surfactant usually amounts to tenths and hundredths of a percent [31], [59], [65], unexpectedly low for a direct bandgap semiconductor.

There are several channels of non-radiative interband exciton relaxation, some of which are governed by internal factors, i.e., the fundamental physical nature of SWCNTs, while others are influenced by external factors, determined by the specific characteristics of the sample.

Among the external factors, the synthesis method of SWCNTs and post-synthesis treatments can be highlighted, which affect the length [66] and defect density in their structure [49], [67], [68]. There is a direct relationship between the defect density in SWCNT structure and the rate of exciton relaxation. Another external factor is the local surrounding environment. For instance, the exciton lifetime in individual SWCNTs is longer compared to SWCNT bundles due to the absence of relaxation channels via energy transfer to neighboring SWCNTs [63]. Additionally, suspensions of SWCNTs stabilized using various surfactants demonstrate different dynamics of interband relaxation, which is attributed to differences in the dielectric permittivity of the medium and the effectiveness of screening the Coulomb potential.[62], [68]

Despite the significant contribution of external factors to the efficiency of nonradiative exciton relaxation in SWCNTs [69], the low QY even in individual, low-defect SWCNTs underscores the importance of internal (fundamental) channels of nonradiative exciton relaxation [70], [71], [72].

One of the fundamental channels could be nonradiative relaxation through a dark singlet exciton, located energetically lower than the bright exciton [73], [74], [75]. However, some researchers question the efficiency of this nonradiative relaxation channel at room temperature due to the

relatively small energy gap between these energy levels [60], [61], [73], [76], [77] .

Another fundamental channel of nonradiative relaxation in carbon nanotubes is exciton-exciton annihilation. Due to the high absorption cross-section of carbon nanotubes (on the order of 10^{-16} cm^2 per carbon atom) [35], [41], even at relatively low excitation powers, multiple excitons can be generated on a single nanotube, allowing for exciton-exciton interactions. During exciton-exciton annihilation, one exciton recombines, transferring its released energy to another exciton, exciting it to a higher energy level [78].

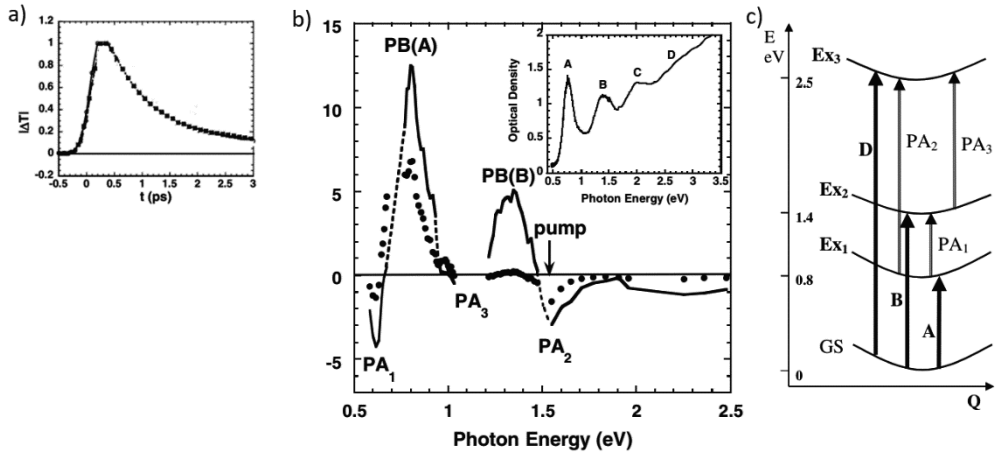

Figure 1.11 a) Dependence of the induced transmittance signal at the E11 energy level on the time elapsed after pumping carbon nanotubes to the E22 level. b) Differential absorption spectrum at delay times of 0 fs (solid line) and 500 fs (dots). c) Schematic representation of excitonic levels and optical transitions observed in the spectra of differential absorption. Reprinted with permission [64]

One of the widely used methods for investigating exciton relaxation dynamics in carbon nanotubes is pump-probe spectroscopy. This method relies on the principle that the population of an energy level can be determined by changes in the sample's transparency to a low-power laser pulse resonant with that level (the probe pulse), which is caused by prior excitation of the excitonic structure of the carbon nanotube with a powerful pump pulse.

The typical dependence of the induced transmittance signal at the E_{11} level on the time elapsed after pumping excitons into the E_{22} level in carbon nanotubes is shown in Figure 1.11a. The rapid increase in population during

the first few hundred femtoseconds correspond to the fast thermalization of excitons from the E_{22} level to the E_{11} level. The subsequent decay is attributed to the abundance of various interband exciton relaxation channels discussed above and is often approximated by a biexponential decay with two effective relaxation times: a fast one on the order of 1 picosecond and a slow one on the order of tens of picoseconds. [62], [69], [74]

It's important to note that in experiments using the pump-probe method, induced absorption signals are also observed (negative signals PA_1, PA_2, PA_3 in Figure 1.11b), which are caused by the fact that pumped excitonic levels can absorb the radiation from the probing pulse, causing the exciton to transition to a higher lying state. (see Figure 1.11c). Several different interpretations of the physical nature of such optical transitions are found in the scientific literature: transition of the exciton from level E_{11} to level E_{22}, [64] transition from a level with one dark singlet exciton to a level with one dark and one bright singlet exciton, [57] formation of a biexciton.[79] Transitions between triplet excitonic states are also reported.[80]

1.4 Trapped quantum states in doped and functionalized single walled carbon nanotubes

As mentioned earlier, one of the obstacles to many practical applications of SWCNTs is their low PL QY. One possible solution to this problem is the localization of excitons in the vicinity of artificially created traps. This chapter will discuss methods for creating such traps, the structure of energy levels in localizing potentials, as well as the dynamics of photoexcitations in SWCNTs with such traps.

1.4.1 Quantum traps fabrication methods

There are two main approaches to engineering artificial emissive defects in SWCNTs. The first approach is usually referred to as sp3 functionalization and involves attaching a large functional group (aryl, alkyl

etc.) to a carbon atom on the SWCNT surface. In the vicinity of such defect the exciton can be trapped by defect potential and will radiatively recombine before quenching on intrinsic SWCNT defects [81], [82], [83], [84], [85], [86], [87], [88]. The energy level of such a trapped exciton might be energetically downshifted compared to the dark exciton level thus preventing the QY suppression. Eventually, such sp3 functionalization of SWCNTs may lead to an improvement in the PL brightness of the SWCNTs by a factor of 4.2 [89]

Oxygen functionalization provides an alternative method for creating zero-dimensional traps in SWCNTs. Oxygen adducts in oxygen-functionalized carbon nanotubes can take on several chemical configurations, including the formation of an epoxide bond between an oxygen atom and two adjacent sp^3 carbon atoms and the formation of an ether bond between an oxygen atom and two sp^2 carbon atoms nearly parallel (ether-l) or perpendicular (ether-d) to the nanotube axis through C-O-C bonds [90]

It is important to note that localization of excitons is not limited to the vicinity of defects induced by a covalent functionalization. A theoretical investigation by Tayo at al. indicated that charged particles, physisorbed on the surface of SWNTs, might play the role of localization centres for excitons [91]. It was also found experimentally in electrochemically doped nanotubes that both excitons and trions are spatially confined because of adsorbed ions, even without chemical bonding with the nanotube wall. [92] The temperature dependence of new doping-induced peaks in PL spectra confirmed the spatial localization of corresponding quasiparticles. [93]

1.4.2 The structure of energy levels in quantum traps

Theoretical studies by Rønnow et al. showed that the interaction of an exciton with either an electron or a hole in a SWNT may lead to the formation of a negatively or positively charged quasiparticle (known as a trion), respectively, detectable even at room temperature [94]. The first

experimental confirmation of this prediction was done by Matsunaga et al., who observed new peaks in absorption and PL spectra of SWNTs after p-doping with 2,3,5,6-tetrafluoro-7,7,8,8-tetracyanoquinodimethane (F4TCNQ) and hydrochloric acid (HCl) [95]. These new peaks were assigned to the optical transitions between the ground (non-excited) energy state of the nanotubes and a new doping-induced energy state, located approximately 100–200 meV (depending on the nanotube diameter) below the bright exciton, and attributed to the positive trion. It was also reported later that trions can be generated by all-optical excitations [79], [96].

Later, applying doping methods such as gate-doping, electrochemical doping, chemical doping with F4TCNQ and HCl, several groups reported new features in linear absorption [97], [98], [99]

On the other hand, a set of works have shown that the covalent functionalization of SWNTs leads to the appearance of very similar spectral features, i.e. the satellite peaks located 100–200 meV below the main exciton peak. [100], [101], [102], [103], [104], [105]

Brozena et al. observed defect-localized excitons in diazonium-functionalized SWNTs and the appearance of a second extra PL peak after chemical doping (reducing) of diazonium-functionalized SWNTs. [106]

1.4.3 Dynamics of photoexcitations in single walled carbon nanotubes with quantum traps

Successful industrial applications of the advanced physical properties of SWCNTs with quantum defects demand a deep understanding of fundamental processes, such as the conversion of ordinary exciton states E_{11} and E_{22} to the functionalization-induced excitonic state E_{11}*, including the formation and recombination dynamics of these states. Over the last decade, persistent efforts have been made to unveil these topics. Investigations utilizing time-resolved PL (TR PL) spectroscopy have demonstrated that the lifetime of functionalization-induced excitons in sp^3-SWCNTs is on the order of several tens of picoseconds, significantly higher than the measured lifetime of pristine band-edge excitons, while the lifetime

of band-edge excitons is shortened in sp^3-SWCNTs compared to pristine SWCNTs [85],[84], [85], [87], [107], [108], [109]

The understanding of exciton dynamics in SWCNTs functionalized through the widely used and promising approach of oxygen functionalization is currently not as well-established as in the case of sp3-SWCNTs. Only one previously published study has investigated the time-domain behavior of excitons in O-SWCNTs [110]. That study utilized TR PL spectroscopy, revealing that in O-SWCNTs, the lifetime of excitons induced by functionalization is significantly longer compared to the lifetime of free excitons. This behavior is reminiscent of what is observed in sp3-SWCNTs. However, no significant impact of oxygen functionalization on the lifetime of free excitons themselves was reported [110]. This lack of observation may be attributed to limitations in the time resolution of the equipment used. Consequently, there has been no thorough investigation into whether the emissive excitonic states induced by functionalization in O-SWCNTs are defect-localized in nature and whether they are populated through the diffusive trapping of free excitons. Furthermore, none of the previously published studies have explored the impact of embedding artificial defects on the dynamics of E_{22} excitons. This is relevant for both sp3 and O-functionalization, with existing research primarily focusing on changes in the E_{11} exciton manifold.

1.4.4 Progress in creating single-photon sources based on single walled carbon nanotubes with quantum defects

Nowadays, when light has become a common information carrier in high-speed worldwide networks, a principal way to achieve absolute security in transferring information is by employing quantum states of light. [111] In quantum communication, the act of measuring a single photon can alter its state, making it impossible for an eavesdropper to intercept the information without being detected. [112] Such unbreakable quantum communication technologies rely on single-photon sources (SPS) as indispensable building blocks.

The general problematics in the field of industrial SPS development lies in simultaneously meeting stringent requirements for successful real-life applications such as compactness, electrical triggering, room-temperature operation, emission at wavelengths of 2nd (~1.3 μm) and 3rd (~1.5 μm) telecom windows.

Since the demonstration of the first SPS in the 1980s, many efforts have been made to satisfy such requirements as compactness, electrical triggering, room temperature operation, and emission at telecom wavelengths. [113], [114], [115] In the last decade, the most promising approach to achieve these goals appears to be based on the use of single-walled carbon nanotubes (SWNT), which are cylindrical nanostructures composed of a single layer of carbon atoms arranged in a hexagonal lattice.

It was demonstrated as early as in 2002, that SWNTs possess robust and stable excitonic PL at diameter-defined wavelengths in the spectral range from ~800 nm to 2.5 μm, which includes so-called telecommunication transparency windows. [116] A few years later, it was demonstrated that infrared light emission from SWNT may be electrically driven. [117] At the end of the 2000s, the first single-photon emission from SWNT was observed. [118] The underlying fundamental process that makes this possible is photon antibunching due to exciton localization in the vicinity of natural inhomogeneities of the environment, which surrounds the nanotube. However, the energy depth of such localization potentials is so small that cryogenic temperatures are required for efficient exciton localization, and thus, photon antibunching.

This motivated significant efforts aimed at introducing artificial localizing potentials deep enough to avoid thermal de-trapping, even at room temperature. Success in this challenge was first achieved in 2010 by the covalent bonding of oxygen atoms to the surface of carbon nanotubes. [104] Such functionalization introduces deep trap photoemissive excitonic states which reveal themselves as an appearance of new red-shifted bands in the PL spectrum.

Five years later, the viability of deeply trapped excitons as a basis for photon antibunching was confirmed experimentally by the first demonstration of room-temperature single-photon emission from an

oxygen-functionalized SWNT under optical excitation. [119] However, emission was achieved only at the 2nd telecom window, and the high value of the second-order correlation function $g^{(2)}(0) = 32.$ was reported, meaning that 32% of the emission events correspond to simultaneous emission of at least two photons, while only the residual 68% corresponds to purely single-photon emission.

Tremendous efforts were subsequently made to improve the performance of SWNT-based SPS and to reduce the $g^{(2)}(0)$ value. In 2016, it was demonstrated that single-photon emission from SWNT might be electrically triggered, but only $g^{(2)}(0)$=0.49 was achieved. [120] In 2017, applying a complex multi-step chemical procedure of surface sp3 functionalization, remarkable purity of single-photon emission ($g^{(2)}(0)$=0.01) from SWNT was achieved at 1.3 μm at room temperature, while a similar purity at 1.5 μm was achieved only at low temperatures. [103] In 2018, exceptionally high single-photon generation frequency was achieved thanks to the integration of functionalized SWNT and silicon microcavities although with values $g^{(2)}(0)$ as low as 0.1. [121] In 2019, improvements in sample fabrication and coupling with the Purcell resonator allowed for achieving exceptional purity of single photon emission ($g^{(2)}(0)$=0.01). [122] In 2021, guanine-functionalized SWNTs were demonstrated to emit single photons at room temperature with a moderate purity of $g^{(2)}(0)$=0.27, but at wavelengths outside any telecom window. [123]

Summarizing the progress made in the last decade on the development of SWNT-based SPS, peculiar chemical functionalization, and cavity integration emerge as the main approaches that provide enhancements in the performance of SWNT as SPS at telecom wavelengths. Recently, theoretical work [124] has proposed an alternative efficient method to enhance the characteristics of SWNT-based SPS. Particularly, it is suggested that the shortening of carbon nanotubes with deep trapped exciton states should improve the purity of single-photon emission sufficiently. The proposed underlying fundamental mechanism is the competing of exciton trapping at artificial defects with exciton-exciton annihilation and end trapping. According to calculations, $g^{(2)}(0)$ might be reduced from a typical value of 0.3 for 4000 nm long nanotubes to a record-

breaking value of 0.0013 for 100 nm long nanotubes. Despite quite exciting predictions, these theoretical considerations concerning the influence of SWNT length on the purity of single-photon generation have not yet been experimentally tested.

The first step on the experimental verification of this hypothesis would be investigation of exciton dynamics SWCNT with localizing trapping defects focusing on the competition between exciton trapping process versus other relaxation mechanisms.

1.4.5 Problems, tasks, and open questions.

In conclusion, there is a pressing need for a simple, efficient, and scalable method for embedding local trapping defects into the SWCNT structure. Understanding the physical nature of photoexcitations in localizing potentials along SWCNT, as well as the processes of population, relaxation and recombination of these states remains a critical challenge. These issues are addressed in the present thesis.

2 Materials, Measurement techniques and Experimental methods

2.1 Preparation of the suspensions of single walled carbon nanotubes with high optical quality

The commercially available (6,5)-enriched CoMoCat SWCNT purchased from Merk was utilized as the pristine material for fabricating the samples under investigation. This material consists of bundles of carbon nanotubes intertwined in a network. In such a scenario, the interactions among the nanotubes exert a significant influence on their optical and physical properties, leading to distortions in their original characteristics, rendering this material unsuitable for the purposes of this study. To achieve the set objectives, it was imperative to create a material containing individual nanotubes that do not interact with each other. To accomplish this, the initial powder of nanotubes was suspended in a solution of sodium dodecyl sulfate (SDS) at a concentration of 0.1 mg/mL. The surfactant was employed to prevent the bundling of nanotube aggregates, as surfactant molecules form micelles on the surface of the nanotubes, hindering such aggregation. To separate the initial nanotube bundles into individual nanotubes, the suspension underwent ultrasonication treatment for 4 hours, with an integrated power of 200 W and a duty cycle of 0.1. The volume of the suspension subjected to treatment was 50 mL. Next, the suspension underwent ultracentrifugation at an acceleration of 125,000 g for 1 hour. As a result, large, undispersed bundles of nanotubes settled at the bottom, while the remaining suspension predominantly contained individual nanotubes encapsulated in surfactant micelles. Approximately 80% of the supernatant was used for further investigations.

2.2 Doping and functionalization of single walled carbon nanotubes

In this study, carbon nanotubes were modified using two different methods. One method involved admixing of HCl to the SWCNT suspension, resulting in a final concentration of up to 40 microliters per milliliter. As will be demonstrated later, this procedure leads to the sorption of hydrogen ions onto the surface of the carbon nanotubes without forming covalent bonds, thus providing local doping. Chapter 3 is dedicated to the investigation of this kind of SWCNTs.

The goal of the second method was to create oxygen defects on the nanotube surface. For this purpose, NaOCl solution was added to the SWCNT suspension. Subsequently, the suspension was exposed to UV light from a mercury lamp (max intensity at 254 nm, power density 27 $\mu W/cm^2$) in an open quartz cuvette.

The hypochlorite ions in the suspension undergo photodissociation under UV irradiation, producing free atomic oxygen and chlorine. While chlorine ions, like sodium ions, may remain in the aqueous medium in a dissociated state, atomic oxygen tends to form chemical bonds either with another oxygen atom to form O_2 molecules or covalently with carbon atoms on the nanotube surface, creating point defects in the structure of SWCNT. [125] It is important to note that prior to this procedure, the suspension was diluted tenfold to reduce the surfactant concentration to 0.2%. This step was necessary because at higher surfactant concentrations, the access of atomic oxygen to the surface of SWCNTs is restricted, thereby hindering the functionalization process. B Chapter 4 is dedicated to investigation of SWCNTs with such artificial oxygen defects.

2.3 Optical absorption spectroscopy

Optical absorption spectroscopy stands out as one of the most straightforward techniques for studying single-walled carbon nanotubes. Its efficacy is particularly pronounced when the samples demonstrate high optical quality, like when nanotubes are evenly dispersed within a thin film or uniformly distributed in a liquid medium (such as an aqueous

suspension). In such scenarios, assessments regarding the nanotube composition fraction, average diameter, diameter distribution width, and other parameters can be reliably made. These assessments are made possible by the strong correlation observed between the electronic structure and the geometry of carbon nanotubes, alongside the established selection rules governing optical transitions in these materials.

In its most basic form, the spectral-dependent optical absorption within a medium can be succinctly described by the equation:

$$dI(\lambda) = -k(\lambda)I(\lambda)dl \tag{4}$$

Here, $I(\lambda)$ denotes the incoming light intensity at the wavelength λ, dl represents the thickness of the absorbing layer, and $k(\lambda)$ is the absorption coefficient.

Expressed in integral form, this concept aligns with the Beer-Lambert-Bouguer law:

$$I(\lambda) = I(\lambda_0)e^{-k(\lambda)\,L} \tag{5}$$

In this equation, $I(\lambda)$ signifies the spectral intensity of transmitted light, and L stands for the thickness of the uniformly absorbing layer.

A dual-beam spectrophotometer was utilized to collect optical absorption spectra of SWCNT suspensions. In this instrument, light emitted from an arc lamp passed through a monochromator to generate a monochromatic light beam. After splitting this beam into two parts, one traversed through a quartz cuvette containing the SWCNT suspension, and its intensity was measured using a photodiode. Simultaneously, the other beam was directed onto a similar photodiode without passing through the sample. By comparing the photocurrents at different wavelengths of light, the optical density values of the sample at each wavelength were determined. Prior to these measurements, calibration was performed to ensure that both beams reached the photodiodes without passing through the sample.

2.4 Raman spectroscopy

Raman spectroscopy provides information about the crystalline structure of SWCNTs by analyzing the spectrum of light scattered by the sample when exposed to a monochromatic laser beam. Since some of the scattered light is inelastically scattered, meaning that it expends some energy to excite phonons in the SWCNTs, the spectrum of the scattered light contains lines with photon energy different from that of the incident beam by the energy of the excited phonon. The spectral positions and shape of these lines carry information about the material's crystalline structure and electron-phonon interaction processes within it.

In this study, SWCNT suspensions were placed in a quartz cuvette under the long-focus objective of a Raman spectrometer. The excitation light with a wavelength of 514 nm passed through the side wall of the cuvette, positioned at an angle of approximately 10 degrees horizontally. The focal point was located 2-3 mm below the cuvette wall. The scattered light was collected in a backscattering configuration and detected using a silicon detector, after being dispersed into a spectrum by a diffraction grating.

2.5 Photoluminescence spectroscopy

The PL spectroscopy method is relatively simple yet highly informative for studying SWCNTs. In this study, a xenon arc lamp was used as the excitation light source in the visible spectrum, and a tunable titanium-sapphire (Ti:Sa) laser was used in the infrared range. The emitted light from the xenon lamp was monochromatized to obtain a monochromatic beam, while the laser beam from the Ti:Sa laser was focused directly onto the sample. In the case of excitation with the xenon lamp, the excitation beam was a 3-4 mm wide strip, while the laser beam from the Ti:Sa laser had a diameter of 2-3 mm on the sample. The emitted light from the sample was collected at a 90-degree angle from the incident radiation to minimize backscattered light. The emitted light was detected by a liquid nitrogen cooled InGaAs array detector, after being dispersed into a spectrum by a diffraction grating.

By varying the excitation wavelength, it was possible to obtain a wavelength-resolved map of the material composition by constructing three-dimensional maps with intensity dependence on both excitation and emission wavelengths. At the same time, the choice of the resonant excitation wavelength allowed for obtaining spectra predominantly from nanotubes with the desired chirality. For the investigation of the (6,5) nanotube, resonance excitation of the E_{22} transition was used with light wavelengths of 570 nm from the xenon lamp and 840 nm from the Ti:Sa laser, corresponding to the excitation of the dark E_{11} exciton via participation in the K process of a phonon sideband.

2.6 Ultrafast transient absorption spectroscopy

In this study, two different pump-probe setups were utilized. To obtain the results presented in Chapter 3, ultrafast transient absorption spectroscopy was implemented as follows. Femtosecond pump pulses with a duration of approximately 35 fs, tunable in the range of 520-750 nm, were generated using an optical parametric amplifier pumped by a femtosecond Ti:Sa laser with a wavelength of 800 nm. Broadband probe pulses were generated by focusing a beam into a sapphire crystal, with the visible part of the spectrum generated in the crystal removed using a filter. Both pump and probe pulses had the same polarization. The time delay between the pulses was controlled by a motorized delay line. The probe pulse was split into two beams, one passing through the pumped region of the sample (due to the overlap of the spots of the two laser beams), and the other passing through the unpumped region of the sample. The wevelength-dependent intensities of each beam were recorded by a spectrometer, allowing comparison of the transmission spectra of the pumped and unpumped materials to determine the pump-induced change in transparency. Measurements were conducted at room temperature.

In Chapter 4 ultrafast time-resolved pump-probe spectroscopy measurements were also carried out using an amplified Ti:sapphire laser

system equipped with an optical parametric amplifier (OPA). However, this system generated 100 fs pulses at a frequency of 1.00 kHz with a central wavelength of 800 nm. Around 90% of the output power was directed towards the OPA to produce tunable pump pulses covering the UV–Visible to near-infrared spectral ranges, enabling sample excitation at desired wavelengths. For all measurements, the pump wavelength was set to 400 nm, with a pulse energy density estimated at 1.5 mJ/cm^2. The remaining 10% of the output power was routed towards the delay line to precisely control the time delay between the pump and probe pulses, and converted into a broadband probe beam for examining the dispersed SWCNTs in transmission mode at normal incidence. Simultaneously, the chopper-modulated pump pulse was spatially and temporally overlapped with the probe beam on the samples. The detector was triggered to detect every probe pulse and calculate the absorption spectrum. The repetition rates of the pump and probe beams were adjusted to 500 Hz and 1 kHz, respectively. Consequently, the impact of the pump beam was observed in only one of the two consecutive probe beams.

3 Non-covalent doping of single walled carbon nanotubes in acid medium

This chapter delves into exploring the structure and physical characteristics of energy levels of photoexcitations in SWCNTs through noncovalent doping via the addition of HCl. To achieve this, a comprehensive approach was adopted, integrating techniques such as PL, optical absorption, Raman spectroscopy, and ultrafast transient absorption spectroscopy.

3.1 Photoluminescence studies

The initial material used to dope SWCNTs via HCl consisted of a suspension of SWCNTs in a 2% aqueous solution of SDS. In Figure 3.1, the excitation-emission PL map of an untreated SWCNT suspension is depicted. The color scale is normalized based on the maximum intensities observed in the 475-720 nm and 720-1000 nm spectral ranges, separately. This normalization was necessary due to the use of different excitation sources, namely the Xe lamp and CW Ti:sapphire laser, which had varying power levels for these regions. The key PL features are denoted by notation $(n,m)^{em}_{abs}$, where (n,m) represents the chiral indices of the corresponding SWCNT, defining its crystalline structure, including diameter and chirality, and thus influencing the energy of excitonic transitions. The subscript and superscript indices indicate the absorptive and emissive energy levels during the PL process, respectively. Therefore, the predominant spectral feature $(6,5)^{11}_{22}$ corresponds to the absorption of light by the E_{22} exciton of (6,5)-SWCNT, followed by the emission of light by the E_{11} exciton of SWCNT with (6,5) chirality. Other optical features correspond to residual PL of SWCNTs having (6,4), (8,3), (7,5), (8,4), and (7,3) chiralities. The assignment of the optical features to SWCNT chiralities is based on the dataset published in [126] .

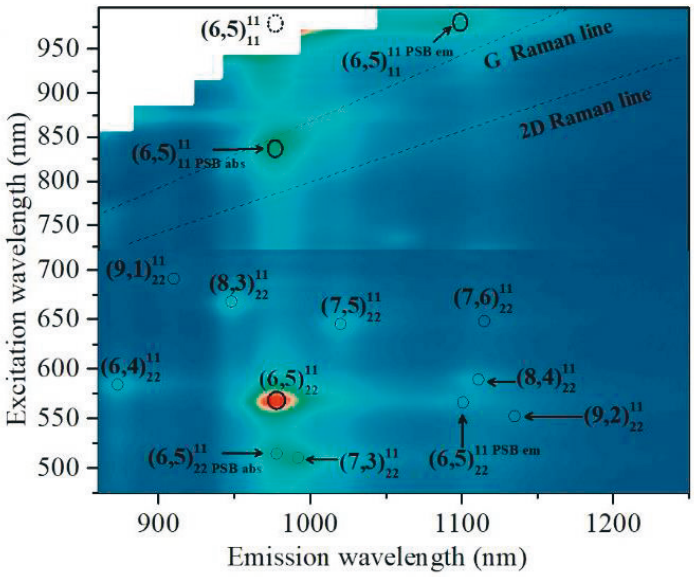

Figure 3.1 Excitation-emission PL maps of pristine single-walled carbon nanotubes. A contrast horizontal lines at 720 nm separate maps obtained using different excitation source (Xe lamp for visible and Ti:sapphire laser for near-infrared (NIR)), color scale normalized separately for each part (blue for 0 and red for 1). Reprinted from paper II (no permissions needed).

The diameters of SWCNTs in the suspension vary between 0.69 nm and 0.84 nm. While the spectroscopic methods used do not allow for an accurate estimation of the length of SWCNTs, it is anticipated to be several hundred nanometers based on the sample manufacturing techniques utilized [127].

It's important to mention the observation of emission and absorption PSB bands, which arise from the participation of a phonon in either the exciton recombination or excitation processes. For instance, the spectral feature $(6,5)^{11}_{11\ PSB\ abs}$, observed with a resonant excitation wavelength of 840 nm and an emission wavelength of 980 nm, corresponds to the simultaneous excitation of a K-momentum dark exciton from the E11 manifold and the band-edge phonon, followed by light emission by a bright E_{11} exciton [11]. By considering the spectral positions of the $(6,5)^{11}_{11\ PSB\ abs}$ and $(6,5)^{11\ PSB\ em}_{11}$ phonon side-bands, we can determine the position of the $(6,5)^{11}_{11}$ spectral feature, indicated by a dashed circle. However, it remains unobservable in the conducted experiment due to

significant scattering of the laser excitation line (depicted as white rectangles in Fig. 3.1).

Figure 3.2a illustrates the PL spectra of SWCNT suspensions with varying concentrations of hydrochloric acid under resonant excitation of (6,5)-SWCNT geometry. For convenience and clarity, when discussing PL spectra, the notation of spectral features will only include information about the emitting level, while the name of the excited level will be omitted. Thus, the most intense peak, located around 980 nm, corresponds to the radiative recombination of the bright E_{11} exciton in (6,5)-SWCNT is noted as $E_{11}(6,5)$. Also noted are spectral features corresponding to the recombination of bright E_{11} excitons in (6,4)-SWCNT and (7,5)-SWCNT. Additionally, in the region around 1115 nm, a spectral feature denoted as PSB (6,5) + E_{11} (7,6) is observed, representing the overlap of two PL signals: the recombination of the bright E_{11} exciton in (7,6)-SWCNT and the recombination of the dark K-momentum E_{11} exciton in (6,5)-SWCNT involving a phonon.

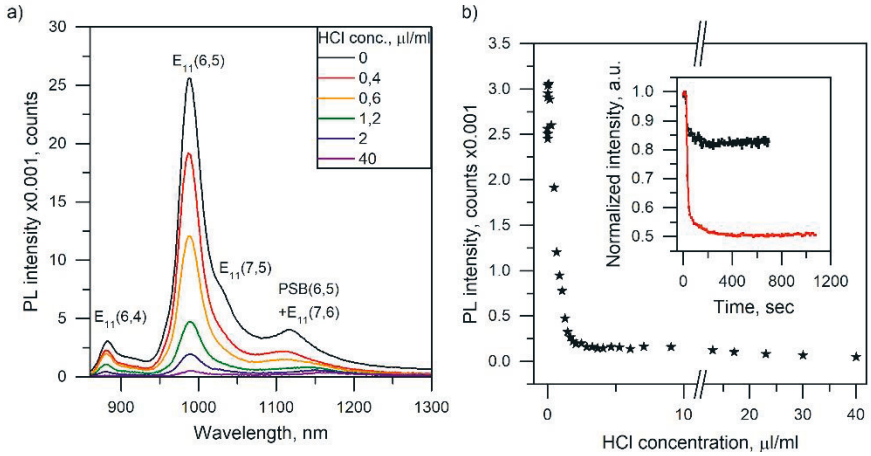

Figure 3.2 a) PL spectra of the SWNT suspensions with different concentrations of added HCl. b) The dependence of the fluorescence signal intensity of the SWCNT suspension on the concentration of hydrochloric acid. The insert: The dependence of the fluorescence signal intensity of the SWCNT suspension on the time elapsed since the addition of hydrochloric acid to the suspension. Two dependencies are presented with different HCl concentration, exposure times and temporal resolutions.

Main observed trend with increasing hydrochloric acid concentration in the SWCNT suspension is the suppression of all the PL peaks mentioned earlier. The dependence of the intensity of the $E_{11}(6,5)$ peak on the

hydrochloric acid concentration is presented in Figure 3.2b. One reason for the decrease in the brightness of the PL signal lies in the depletion of high-lying electronic levels of the valence band and the corresponding reduction in the oscillator strength of the excitonic optical transition due to doping of the SWCNTs when hydrochloric acid is added to the SWCNT suspension. Additionally, the decrease in intensity may be partially attributed to the sensitivity of the surfactant to the acidity of the medium and its potentially less effective suspension of individual SWCNTs.

It is important to note here that, besides the concentration of hydrochloric acid, another significant parameter affecting the intensity of PL is the time elapsed since the addition of the acid to the suspension. However, from the dependency presented in Figure 3.2 c, it can be observed that if the time elapsed since the addition of hydrochloric acid to the suspension exceeds 3 minutes, this parameter does not affect the brightness of PL. Therefore, to eliminate the influence of this parameter on the obtained results, a five-minute time interval between the addition of hydrochloric acid to the suspension and the registration of optical spectra was maintained in this study.

Another effect observed with increasing acid concentration in the suspension is the emergence of a new PL peak centered around 1150 nm upon the addition of hydrochloric acid to the suspension. This peak is labeled as X_{PL} in Figure 3.3a, which depicts normalized PL spectra of SWCNTs at several different concentrations of hydrochloric acid in the suspension. Despite the decrease in the intensity of the X_{PL} peak with increasing acid concentration, along with the overall PL signal, the ratio of the X_{PL} peak intensity to the intensity of the E_{11}(6,5) peak increases (see Figure 3.3b).

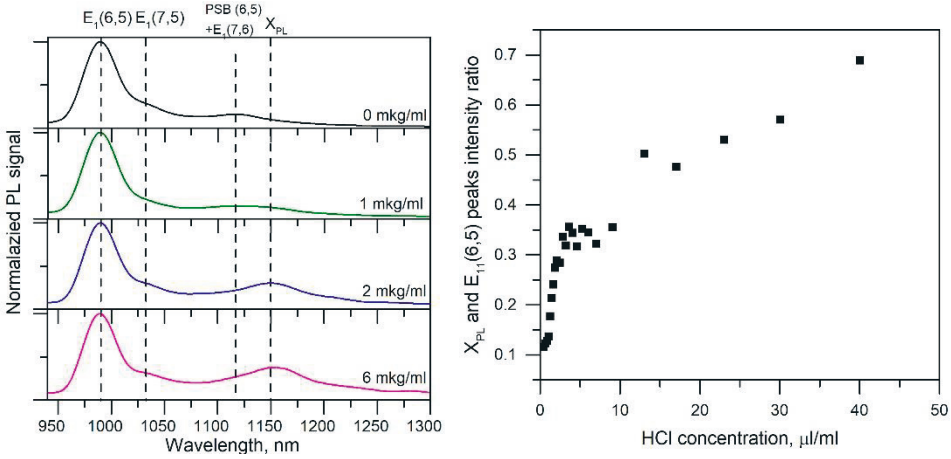

Figure 3.3 a) Normalized PL spectra of SWCNT suspensions at several concentrations of hydrochloric acid in the suspension. Excitation wavelength is 575 nm. Reprinted from paper I (no permissions needed) b) Dependence of the intensity ratio of the X_{PL} and $E_{11}(6,5)$ peaks on the amount of HCl admixed into the SWCNT sample.

To verify whether the X_{PL} peak is an attribute of the fluorescence properties of SWCNTs, a reference experiment was conducted while keeping all conditions the same except for the presence of SWCNTs in the suspension. The absence of any fluorescence signal in the aqueous solution of the surfactant with hydrochloric acid confirmed that the X_{PL} peak in the fluorescence spectra is observed because of the interaction of HCl with SWCNTs.

Despite obtaining spectra with a clearly defined X_{PL} peak under resonant excitation of (6,5)-SWCNTs, to associate it with SWCNTs of specific geometry, it is necessary to compare the fluorescence spectra under various resonance excitation conditions. Figure 3.4 shows the fluorescence spectra of the suspension under resonant excitation of (6,4)-SWCNTs normalized to the maximum of the $E_{11}(6,4)$ peak.

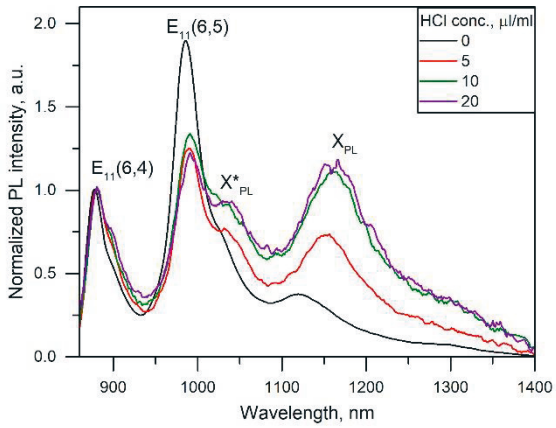

Figure 3.4 PL spectra of SWCNT suspensions with varying concentrations of hydrochloric acid. Excitation wavelength is 580 nm.

Despite the fact that the excitation wavelength is no longer resonant for (6,5)-SWCNTs, the most intense peak remains E_{11}(6,5). This is due to the proximity of the resonances of (6,5)-SWCNTs and (6,4)-SWCNTs (575 nm and 585 nm, respectively), and also because the concentration of (6,5)-SWCNTs in the suspension is much higher than that of (6,4)-SWCNTs (see Fig. 3.1). Nevertheless, the intensity of the E_{11}(6,4) peak is significantly higher than under resonant excitation of (6,5)-SWCNTs. Additionally, the appearance of a new weak peak X^*_{PL} around 1035 nm can be noticed, the shape of which is heavily distorted due to overlap with the excitonic peak E_{11}(6,5). The observed correspondence of the resonant excitation conditions of the new peaks (X and X*) and the main excitonic peaks in SWCNTs of different geometries leads to the conclusion that the X_{PL} and X^*_{PL} peaks are attributes of the PL properties of (6,5)-SWCNTs and (6,4)-SWCNTs, respectively.

To clarify the physical nature of the new PL peak X, it is necessary to first verify the assumption that X_{PL} may be a heavily shifted spectral feature of the PSB (6,5)&E_{11}(7,6). This assumption is not unfounded, as the large surface area of SWCNTs compared to their volume results in a strong sensitivity of their PL properties to the local dielectric permittivity of the environment near the surface. Specifically, the position of PL peaks can significantly change (see Fig. 1.9), as observed, including in this study, when hydrochloric acid is added to the SWCNT suspension.

Figure 3.5 illustrates the dependence of the positions of the X_{PL} and $E_{11}(6,5)$ peaks on the concentration of hydrochloric acid in the suspension. Although qualitatively, the dependencies for these two spectral features have a similar shape, significant differences are observed in the quantitative characteristics of the dependencies. Upon reaching a hydrochloric acid concentration of 40 µl/ml, the excitonic peak shifts to longer wavelengths by approximately 5 nm, while the maximum of the new spectral feature X_{PL} demonstrates a shift of more than 15 nm.

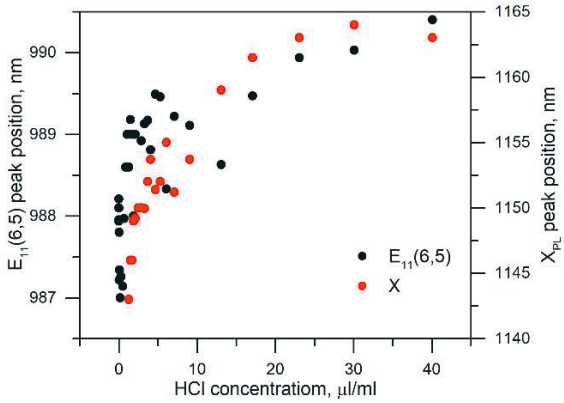

Figure 3.5 The dependence of the positions of the PL peaks $E_{11}(6,5)$ and X_{PL} on the concentration of hydrochloric acid in the suspension.

On one hand, such a significant difference in the sensitivity of the excitonic transition $E_{11}(6,5)$ and X_{PL} to the surrounding environment argues against the suggested hypothesis, as the PSB (6,5) and $E_{11}(7,6)$ peaks are similar in their physical nature, and their sensitivity to the acidity of the environment should not differ significantly from that of $E_{11}(6,5)$. On the other hand, the lower the concentration of hydrochloric acid, the greater the sensitivity to the acidity of the environment demonstrated by X, which is consistent with the assumption that X_{PL} may be a highly shifted peak, which may also occur in the spectra of undoped SWNTs.

To resolve this issue, the process of changing the PL properties of the SWNT suspension at low concentrations of hydrochloric acid was more thoroughly investigated. Figure 3.6 shows the evolution of the PL spectrum

of the SWNT suspension upon gradual addition of hydrochloric acid in small quantities.

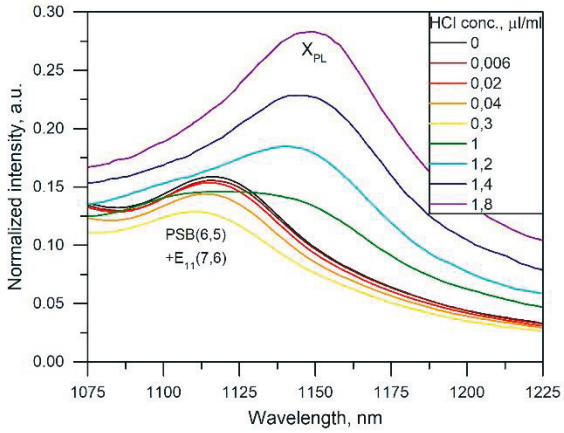

Figure 3.6 PL spectra of the SWNT suspension in the spectral range of X_{PL} at various concentrations of hydrochloric acid.

As the concentration of hydrochloric acid increases from 0 to 0.3 µl/ml, the suppression of the PSB(6,5) + E11(7,6) peak is observed, along with its very weak blue shift. This can be explained by the fact that the component of the E1(7,6) peak, which has a slightly longer wavelength than the PSB(6,5) component, begins to be suppressed at lower concentrations than the spectral features associated with (6,5)-SWTs. This is due to the narrower bandgap of (7,6)-SWNTs compared to (6,5)-SWNTs.

After the concentration of hydrochloric acid exceeds 0.3 µl/ml, the PL spectrum begins to change qualitatively. For example, at a concentration of 1 µl/ml, in addition to the PSB(6,5) + E1(7,6) peak, a signal in the range of 1140-1150 nm starts to appear (green line). The intensity of this signal increases with further increase in the concentration of hydrochloric acid, leading to the observation of a distinct PL peak X_{PL} at concentrations above 1 µl/ml.

Thus, a detailed study of PL spectra at low concentrations of hydrochloric acid allows us to conclude that the observed PL peak X_{PL} is a new spectral feature of SWCNT associated with the interaction with hydrochloric acid, rather than a heavily shifted PSB(6,5) peak.

3.2 Optical absorption studies

Optical absorption spectroscopy can be considered as a complementary method to PL spectroscopy. In the experiments described in this section, optical absorption spectroscopy was employed for additional verification of the results obtained through PL spectroscopy.

In Fig. 3.7a optical absorption spectra in the SWCNT suspension at various concentrations of hydrochloric acid in the spectral range of the first and second excitonic transitions are presented. Spectral features associated with the excitation of excitons E_{11} and E_{22} in SWCNTs of different geometries are observed in the spectral ranges of 850-1200 nm and 500-800 nm, respectively. Additionally, at concentrations above 2 µl/ml, a spectral feature around 1150 nm is observed, denoted as X_{abs}.

With increasing concentration of hydrochloric acid, a significant suppression and redshift of the spectral features of E11 are observed, as well as a less noticeable suppression and redshift of the spectral features of E_{22}. Quantitatively characterizing these processes is complicated, as unlike the PL spectra of strictly semiconducting nanotubes with resonant excitation, the optical absorption spectra involve overlapping spectral features associated with all the different geometries of SWCNTs present in the sample.

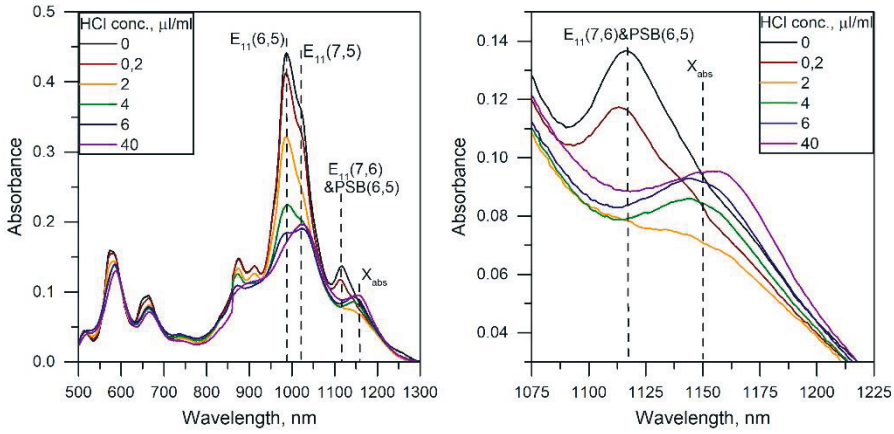

Figure 3.7 Optical absorption spectra of SWCNT suspension with different concentrations of HCl. a) in a wide spectral range b) in the spectral range of the X_{abs}.

The change in the dielectric permittivity of the environment surrounding SWCNTs, leading to the redshift of the observed peaks, is attributed to two factors. Firstly, it is the direct influence of hydrogen and chlorine ions in the vicinity of SWCNTs. Secondly, the acidity of the environment affects the efficiency of SWCNT dispersion, leading to the formation of SWCNT bundles, i.e., neighboring SWCNTs in the bundle start to influence the local dielectric permittivity of the environment surrounding SWCNTs. In the case of luminescence discussed in section 3.1, the second factor practically does not have an influence, as the main contribution to the luminescent signal comes from individual SWCNTs.

The combined effect of these two factors influences the change in the shape and position of the E_{11}(6,5) peak, resulting in the gradual suppression of the component associated with individual (6,5)-SWCNTs (at 980 nm), while the component associated with (6,5)-SWCNT bundles (at 1025 nm) becomes progressively more noticeable.

Confirmation that the optical transition E11 in (6,5)-SWCNT bundles has a wavelength around 1025 nm can be obtained by examining the PL spectrum of (6,5)-SWCNT films (see Fig. 3.8). Indeed, the peak fluorescence in such films under resonant excitation of (6,5)-SWCNTs is located around 1025 nm (red line), whereas the peak maximum in the (6,5)-SWCNT suspension is around 980 nm (black line).

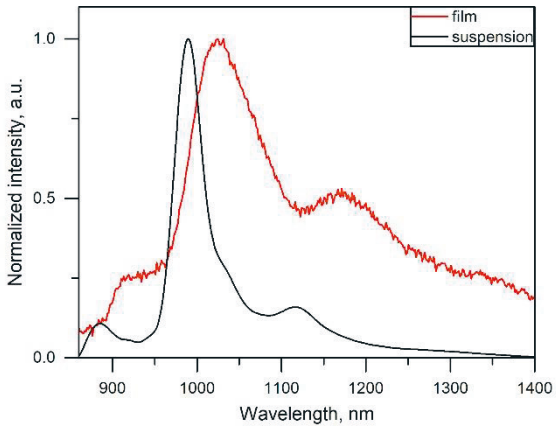

Figure 3.8 PL spectra of the (6,5)-SWCNT suspension (black line) and the film derived from it (red line). Excitation wavelength is 575 nm.

As seen in Fig. 3.7b, with increasing concentration of HCl, there is a gradual suppression of the E_{11}(7,6) peak centered around 1115 nm, which becomes indistinguishable from the background at a concentration of 1 µl/ml (green line). Only after this, a gradual increase in the new spectral feature X_{abs} is observed. This observation demonstrates that the observed peak X_{abs} cannot be attributed to the E_{11}(7,6) peak shifted due to SWCNT aggregation.

Taken together, the data from optical absorption spectroscopy and PL spectroscopy lead to the conclusion that the spectral features X_{abs} and X_{pl} correspond to the same energy level, which arises in the energy structure of (6,5)-SWCNTs due to the influence of HCl added to the suspension.

3.3 Raman spectroscopy studies

One hypothesis explaining the phenomenon of the emergence of new spectral features X_{abs} and X_{PL} is that HCl may contribute to the formation of defects in the structure of SWCNTs through reactions with carbon atoms. In the vicinity of defects in SWCNTs, there is a locally modified potential of the crystal lattice, leading to the appearance of new energy levels of excitons. These excitons are called defect-localized, as their wave function is localized within the modified potential. Raman spectroscopy was employed in this study to test the hypothesis of defect-localized excitons in SWCNT doped via HCl.

In Figure 3.9, Raman spectra of SWCNT suspensions before and after doping with HCl at a concentration of 2 µl/ml are presented. Upon addition of HCl, firstly, a shift of some Raman modes to higher frequencies was observed, and secondly, the intensity of all Raman modes decreased, with the RBM mode (Figure 3.9c) being suppressed more strongly than the others. Taken together, these effects confirm the doping of SWCNTs in an acidic environment.

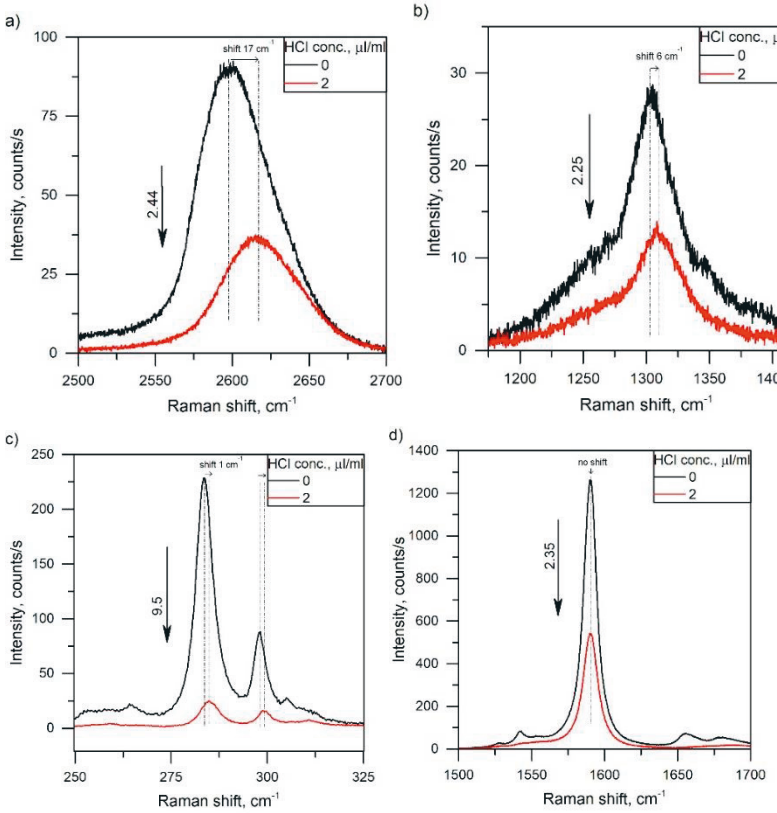

Figure 3.9 Raman spectra of pristine (black line) and doped (red) SWCNTs at an HCl concentration of 2 µl/ml.

Figure 3.10 illustrates the dependency of the intensity ratio between the breathing mode and the defect mode, as well as its overtone to the intensity of the tangential mode, on the concentration of HCl in the SWCNT suspension. The absence of growth in the defect mode relative to the tangential mode suggests that the addition of hydrochloric acid does not affect the quantity of defects in the SWCNT structure. In light of the data obtained through PL spectroscopy and optical absorption spectroscopy, this outcome implies that the new spectral features X_{PL} and X_{abs} cannot be interpreted as excitons localized in the vicinity of defects in the SWCNT structure created due to interaction with HCl.

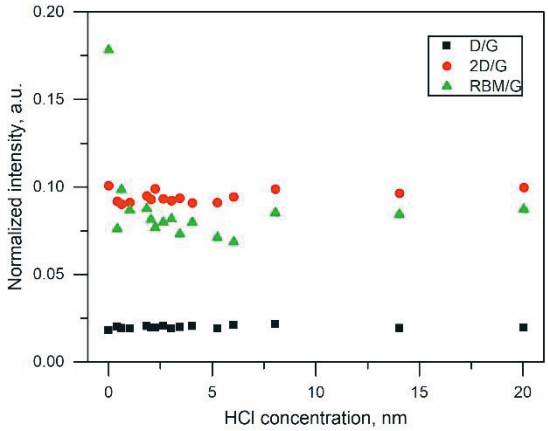

Figure 3.10 The dependence of the intensity ratio of various Raman modes to the intensity of the tangential mode.

3.4 The mechanism of single walled carbon nanotubes doping via addition of HCl

The observed changes in the optical properties of SWCNTs may arise from doping with both positive hydrogen ions and negative chloride ions, formed during the dissociation of hydrochloric acid. To determine which of these mechanisms is at play, a series of experiments were conducted involving the reconstitution of the suspension using sodium hydroxide.

The addition of sodium hydroxide to SWCNT suspension, previously doped with hydrochloric acid, leads to reverse changes in the fluorescence spectra (see Fig. 3.11a). This occurs due to neutralization reaction between hydrochloric acid and sodium hydroxide. During such a reaction, the concentration of free hydrogen ions decreases as they bind with hydroxyl groups to form water. However, Na+ and Cl- ions remain dissociated, and the concentration of free chlorine ions does not change, as the concentrations used in this study are significantly lower than the solubility limit of sodium chloride in water. Based on this, it can be concluded that the doping of SWCNTs and the corresponding change in their optical properties are caused by the interaction of SWCNTs with hydrogen ions rather than chlorine ions.

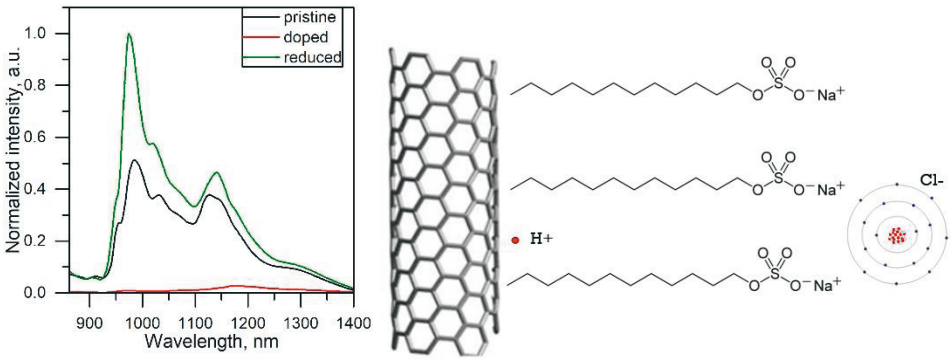

Figure 3.11 a) Fluorescence spectra of SWCNT suspensions: pristine, doped with HCl, and reduced with NaOH. b) A schematic representation of the morphological structure of the nearest environment of SWCNTs.

The fact that doping is caused by the interaction with hydrogen ions rather than chlorine ions can be explained by considering the morphology of the immediate environment of SWCNTs. The polar surfactant molecules are arranged along the radial directions of SWCNTs with weakly negative ends towards SWCNTs and weakly positive ends (with sodium atoms) towards the aqueous environment. Such a configuration makes it difficult for negatively charged chlorine ions with larger ionic radius to penetrate the surface of SWCNTs, while hindering the penetration of hydrogen ions much less (see Fig. 3.11b).

Indirectly, the conclusion that hydrogen ions are the dopant is supported by the ability to obtain a brighter PL signal in the restored suspension compared to the original one. This indicates that in the original suspension SWCNTs are extremely weakly doped, and upon adding a sufficient amount of sodium hydroxide, the concentration of hydrogen ions in the vicinity of the SWCNTs becomes lower than in the original suspension neutralizing the initial weak doping of SWCNTs and leading to an increase in the PL signal.

3.5 Ultrafast transient absorption spectroscopy studies

Additional information necessary to elucidate the nature of the energy level X can be obtained by analyzing the population dynamics of this level.

For this purpose, suspensions of SWCNTs doped in HCl were investigated using the pump-probe method. Furthermore, these studies were motivated by the fact that energy levels induced by doping SWCNTs are not necessarily optically bright, meaning they cannot be directly detected using PL and optical absorption spectroscopy methods. Since photoexcitations in SWCNTs can have sub-picosecond lifetimes, laser pulses shorter than 100 fs were used in pump-probe experiments.

Figures 3.12 (a) and 3.12 (b) depict color maps illustrating the dependence of the change in optical density in suspensions of pristine and doped (HCl concentration 2 µl/ml) SWCNTs, respectively, on the temporal delay between pump pulses (wavelength 570 nm) and probing.

The population of the E_{11} level in (6,5)-SWCNTs due to relaxation from the E_{22} level, which is pumped, leads to induced transparency in the wavelength region around 980 nm. Additionally, in the color maps of both pristine and doped SWCNTs, another signal of induced transparency is observed. In the former case, it is centered around 1115 nm, while in the latter, it is around 1140 nm.

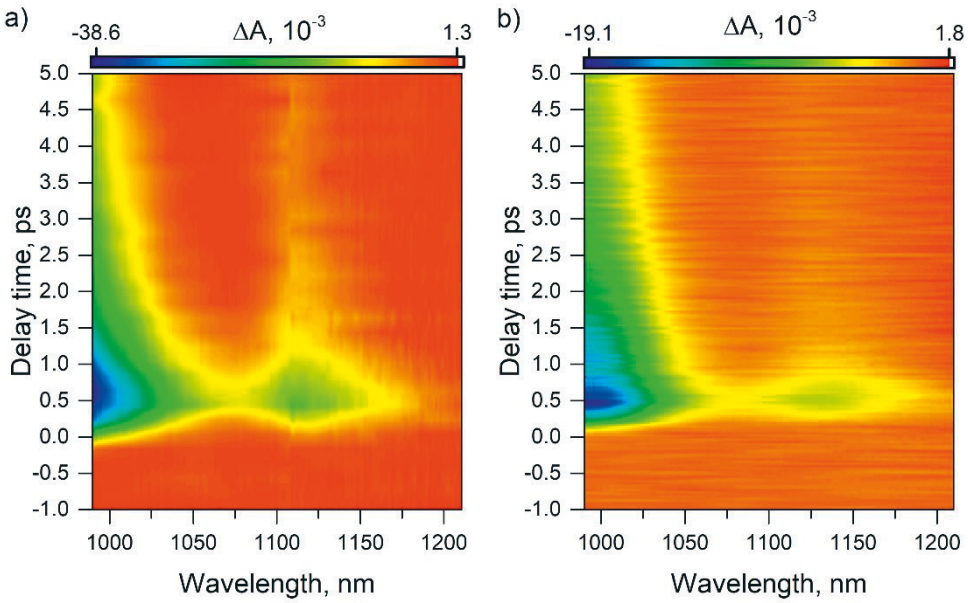

Figure 3.12 Color maps showing the transient absorption in the suspension of pristine SWCNTs (a) and SWCNTs doped with HCl at a concentration of 2 µl/ml (b). Reprinted from paper I (no permissions needed)

To interpret these peaks, we examine the normalized spectra of the transient absorption in undoped, moderately doped (2 µl/ml), and heavily doped (20 µl/ml) SWCNTs at a fixed time delay between the pump and probe pulses, set at 0.5 ps (see Fig. 3.13).

In the vicinity of 990 nm, the most intense spectral feature is observed, which is associated with the population of the excitonic level E_{11}(6,5). In undoped SWCNTs, there is also a peak around 1115 nm, caused by the presence of impurity geometry (7,6)-SWCNTs. In doped SWCNTs, a spectral feature labeled as X_{pp} is observed, demonstrating a red shift from 1140 nm to 1160 nm as the acidity of the medium increases. Similar behavior is exhibited by the peaks X_{PL} and X_{abs} in the spectra of PL and optical absorption (see Fig. 3.6 and Fig. 3.7b). In sections 3.2 and 3.3, it was demonstrated that these spectral features X_{PL} and X_{abs} cannot be attributed to the strongly shifted peak E_{11}(7,6), but rather arise from the emergence of a new energetic level X upon doping of the SWCNTs. This leads to the conclusion that the spectral feature X_{pp} is attributed to the population of the same energetic level X

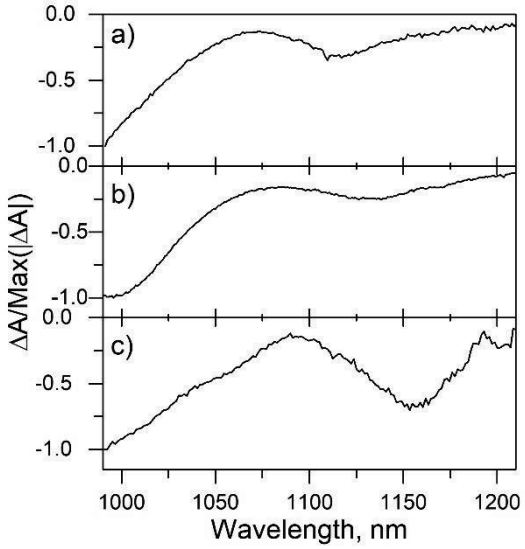

Figure 3.13 The normalized spectra of transient absorption ΔA at a time delay of 0.5 ps in suspensions of SWCNTs with HCl concentrations of 0 µl/ml (top), 2 µl/ml (middle), and 20 µl/ml (bottom).

Additional confirmation that the peak X_{PP} cannot be the shifted peak $E_{11}(7,6)$ is obtained by comparing the relaxation dynamics of these spectral features. Indeed, the spectral feature X_{PP} relaxes significantly faster than $E_{11}(7,6)$ (see Fig. 3.14b). One might suppose that doping could lead to a substantial reduction in the decay time of $E_{11}(7,6)$ excitons; however, such an assumption contradicts the fact that the relaxation dynamics of $E_{11}(6,5)$ excitons do not undergo significant changes upon doping (see Fig. 3.14a).

In Fig. 3.15 a) and b), spectra of transient absorption in suspensions of pristine and moderately doped SWCNTs, respectively, are presented at several fixed time delays between pump and probe pulses. Besides the two spectral features discussed earlier, $E_{11}(6,5)$ and X_{pp}, manifesting as induced transparency, at longer time delays between pump and probe pulses, a signal of induced absorption is observed in the spectra of doped SWCNTs in the wavelength region around 1200 nm. In contrast, induced absorption in this wavelength region is not observed in the spectra of pristine SWCNTs.

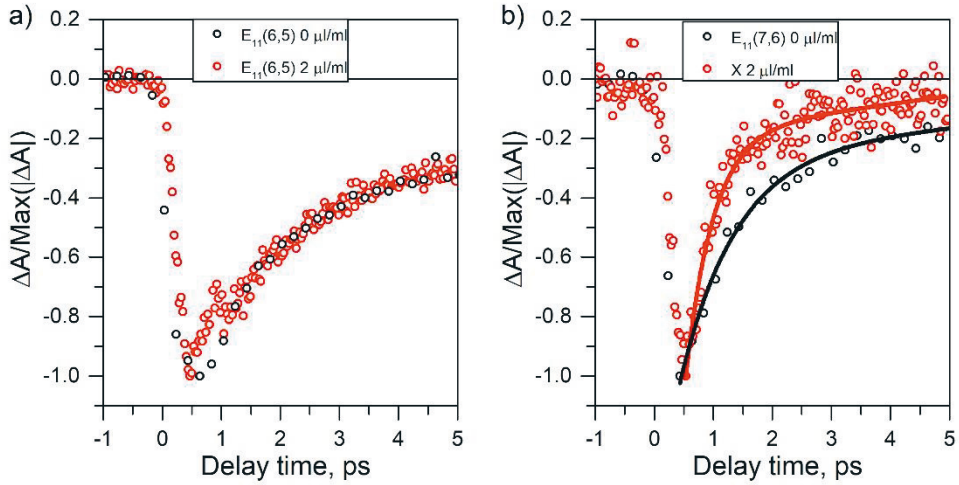

Figure 3.14 a) Relaxation dynamics of the E11(6,5) exciton in pristine and doped SWCNTs. b) Relaxation dynamics of the E11(7,6) exciton and the X level in pristine and doped SWCNTs.

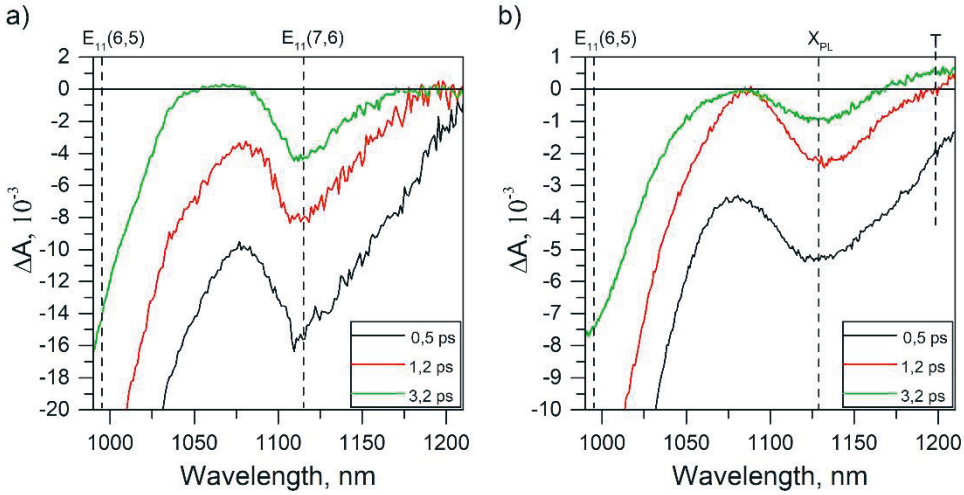

Figure 3.15 Spectra of transient absorption in pristine (a) and doped SWCNTs (b) at several fixed time delays between pump and probe pulses.

The detailed illustration of this effect is visible in Figure 3.16, where the dependencies of the change in optical density at a wavelength of 1200 nm over the time delay between pump and probe pulses are compared for pristine (black line) and doped (red line) SWCNTs. In both cases, the pump pulse initially leads to brightening of the sample at the wavelength of 1200 nm. From the color maps (Fig. 3.12) and their temporal slices (Fig. 3.14), it is evident that this negative signal is a consequence of the broadening of the peaks $E_{11}(7,6)$ and X_{PP} in pristine and doped SWCNTs, respectively. Upon relaxation of the photoexcitation of $E_{11}(7,6)$, the transparency of the sample with pristine SWCNTs at a wavelength of 1200 nm also returns to its original value ($\Delta A=0$). However, as the photoexcitation of X_{PP} in doped SWCNTs relaxes, a signal of induced absorption T_{PP} ($\Delta A>0$) begins to be observed at delays exceeding 1.5 ps.

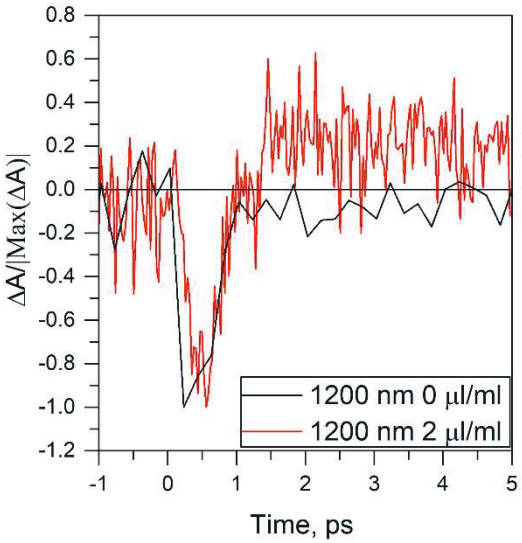

Figure 3.16 The dependence of the normalized intensity of the TA signal in the vicinity of 1200 nm on the time delay between the pump and probe pulses.

Thus, the spectroscopic feature T_{PP} in doped SWCNTs is clearly observed at time delays exceeding 1.5 ps, while at shorter time delays it overlaps with the more intense side wing of the spectral feature X_{PP}. Consequently, the dynamics associated with the spectral feature T_{PP} of the energy level cannot be directly obtained as a vertical slice of the color map in Fig. 3.12b, as it is also necessary to subtract the contribution of the spectral feature X_{PP} with proper normalization.

The obtained dependence of the population of the energy level associated with the spectral feature T_{PP} on time is presented in Fig. 3.17 (green line). On the same plot, the dynamics of the levels E_{11}(6,5) (red line) and X (blue line) are also depicted. The fact that the population of the energy level associated with the spectral feature T_{PP} occurs with a delay of about 1 ps compared to the population of levels E_{11}(6,5) and X, suggests that the spectral feature T_{PP} cannot be associated with the energy levels E_{11}(6,5) and X, but rather is attributed to the existence of another energy level T in doped SWCNTs.

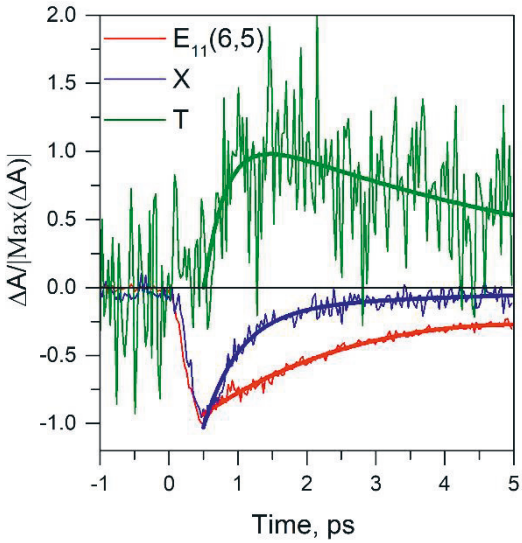

Figure 3.17 The dependence of the normalized TA signal intensity of different spectral features on the time delay between pump and probe pulses.

Unlike the energy levels $E_{11}(6,5)$ and X, whose population manifests as induced transparency, the population of the energy level T leads to induced absorption, i.e., more effective absorption of radiation with a wavelength around 1200 nm. This indicates that the positive signal in this wavelength region corresponds to an optical transition from the T level to some higher-lying level.

The absence of any spectral features associated with the energy level T in the spectra of optical absorption and fluorescence leads to the conclusion that the oscillator strength of direct optical transitions between the ground state of doped SWCNTs and the energy level T is small compared to the oscillator strength of optical transitions between the ground state of SWCNTs and the energy level X. Therefore, the energy level T is populated due to relaxation from the X level, rather than through direct optical transition from the ground state of SWCNTs.

3.6 Discussion on the physical nature of doping induced energy levels in carbon nanotubes doped with HCl

The attribution of the trion nature to the doping-induced spectral feature in the works [92], [98], [128], [129], [130], [131] is based on the argument of the correspondence between the experimentally observed chiral dependence of the spectral positions of new peaks and the diameter of the theoretical curve described by formula.

$$\Delta = \frac{A}{d} + \frac{B}{d^2} \quad (6)$$

where Δ stands for the energy difference between ordinary E_{11} exciton and doping induced spectral feature, d stands for the diameter of SWCNT, while A and B are free parameters of the model. However, in these studies, significant deviations of 20-40 meV from the theoretical curve are allowed during the approximation of experimental points. Moreover, the selected values of the two free parameters A and B vary significantly from one study to another.

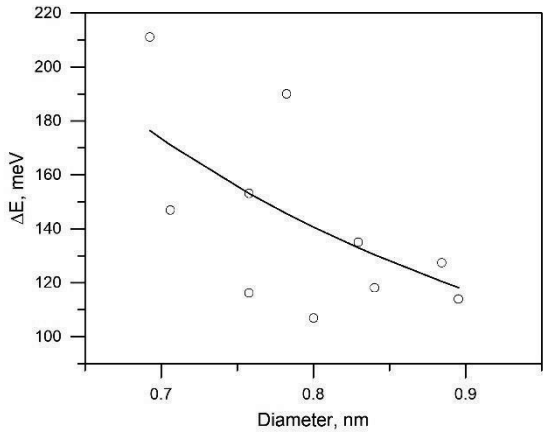

Figure 3.18 Dots: dependence of the energy difference between the main and functionalization-induced PL peaks on the diameter of oxygen-functionalized SWCNTs, obtained in the study [90]. Line: the theoretical dependence for the energy difference between trion energy and exciton energy on the SWCNT diameter.

The weakness of such a criterion for interpreting new doping-induced features is well illustrated by the possibility of selecting parameters A and B (see Figure 3.18), allowing formula (6) to describe the diameter

dependence of the positions of localized excitons in oxygen-functionalized SWCNTs [90], with deviations of experimental points from the theoretical curve being of the same order of magnitude as in the works [92], [98], [128], [129], [130], [131].

The doping-induced spectral features are explained by the formation of defect-localized excitons in cases where doping is accompanied by the formation of defects in the structure of SWCNTs [84], [85], [89], [97], [103], [105], [108], [132], [133]. For example, in studies [134], [135], [136], where two doping-induced energy levels are observed, the energy level X is interpreted as an exciton localized on a defect. Since we do not observe any significant increase in the defect mode in the spectra of Raman scattering in our work, the hypothesis of localization on the defect should be rejected. Considering the results presented in section 3.4 allows us to conclude that the doping of SWCNTs occurs due to the interaction of SWCNTs with hydrogen ions absorbed on the surface of SWCNTs without the formation of covalent bonds. If we neglect the diameter of SWCNTs compared to their length, i.e., consider SWCNTs as a truly one-dimensional structure, such an ion creates a Coulomb-like potential.

$$U(x) = \frac{1}{4\pi\varepsilon\varepsilon_0}\frac{e}{\sqrt{x^2 + l^2}} \tag{7}$$

, where l is the distance from the axis of the SWCNT to the adsorbed hydrogen ion, and the x-axis coincides with the axis of the SWCNT, with the coordinate origin located at the point nearest to the adsorbed ion. To consider the influence of such a potential on the energy of excitons in SWCNTs, it is necessary to take into account the perturbation in the form of the term

$$H_{pert} = \frac{1}{4\pi\varepsilon\varepsilon_0}\left(\frac{e^2}{\sqrt{{x_h}^2 + l^2}} - \frac{e^2}{\sqrt{{x_e}^2 + l^2}}\right) \tag{8}$$

where x_h and x_e are the coordinates of the hole and the electron, respectively. According to the solution of the corresponding quantum mechanical problem, provided in the theoretical work [91], taking into account such a potential can led to a reduction in the exciton energy by up to 100 meV. Thus, the absence of defect generation in SWCNTs during doping is not sufficient grounds to exclude the hypothesis of a localized

exciton, since adsorbed ions and other environmental heterogeneities induced by doping can act as localization centers.

In the vicinity of the potential (7), charge carriers can also be localized. The problem of finding the eigenvalues of energy for charge carriers in such a potential belongs to the class of problems of a "one-dimensional hydrogen atom":

$$-\frac{\hbar^2}{2m}\frac{d^2\psi}{dx^2}-\frac{1}{4\pi\varepsilon\varepsilon_0}\frac{e^2}{\sqrt{x^2+l^2}}\psi=E\psi; \tag{9}$$

Adapting the solution to this problem [137], [138], [139] for the case of (6,5)-SWCNTs doped with hydrochloric acid allows for an estimate, according to which the binding energy of the ground state is approximately 100 meV in magnitude.

The coexistence of strongly bound excitons and charge carriers localized in the same spatial region makes it plausible to assume the formation of a trion localized in the same potential. The observed delay in populating the energy level T compared to the level X indirectly confirms this assumption because the measured value of the time delay (1 ps) corresponds to a previously published value of the characteristic time for trion formation from an exciton and a carrier [135]. Based on this, we interpret the second energy level T induced by doping, first detected in SWCNT doped via interaction with HCl, as a trion state localized in the same potential as the X state. This interpretation is consistent with other studies [134], [135], [136] where a similar energy level was observed in SWCNTs doped by other methods. However, there is still ample room for further research in this area. Experiments sensitive to spin (e.g., using circular polarization or based on level splitting in a magnetic field) are needed for direct verification of the trion nature of the energy level T.

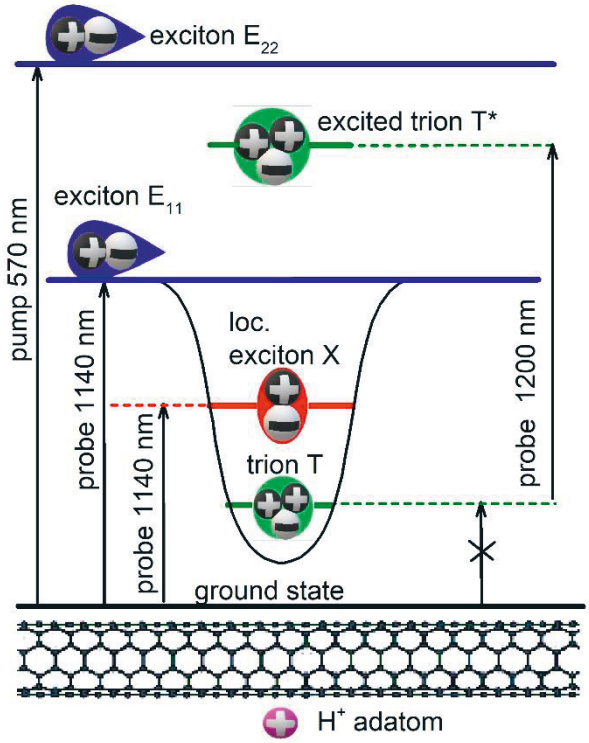

Figure 3.19 Simplified schematic illustration of the energy levels in SWCNT doped via interaction with HCl. Reprinted from paper I (no permissions needed)

In this study, it was demonstrated that the trionic level T in SWCNT doped via interaction with HCl cannot be directly excited from the ground state of SWCNTs but is populated only due to relaxation from higher lying levels, which is consistent with the findings of [135] but contradicts the results presented in [134], [140]. Such discrepancies in experimental results are presumably due to the specific characteristics of doping methods. The signal of induced absorption at a wavelength around 1200 nm is interpreted as an optical transition from the trion state T to the excited trion state T* (see Fig. 3.19). Since the energy difference between these levels (~1 eV) is close to the energy difference between the first and second bright excitons E_{22}-E_{11}=0.9 eV, we assume that the energy level T* is located several hundred meV below the bright exciton E_{22}. This is consistent with the results of theoretical calculations for trion energies in (8,0)-SWCNTs, as reported in [141], where a series of trion states are reported to be located 300 meV, 200 meV, and 150 meV below the bright exciton E_{22}.

4 Functionalization of single walled carbon nanotubes with oxygen quantum defects

This chapter is dedicated to refining the technology of oxygen functionalization of SWCNTs to achieve more intense PL. Additionally, it delves into the study of ultrafast processes of excitation, recombination, and trapping of excitons in SWCNT functionalized with oxygen (O-SWCNT).

4.1 Photoluminescence studies

The starting material for obtaining O-SWCNTs was a suspension similar to that used for doping with HCl (Chapter 3). For convenience, the PL map of the original suspension is presented again in Figure 4.1a alongside the PL map of the same suspension after oxygen functionalization (Figure 4.1b), based on the photodissociation of sodium hypochlorite (see Section 2.2 for detailed description of functionalization procedure)

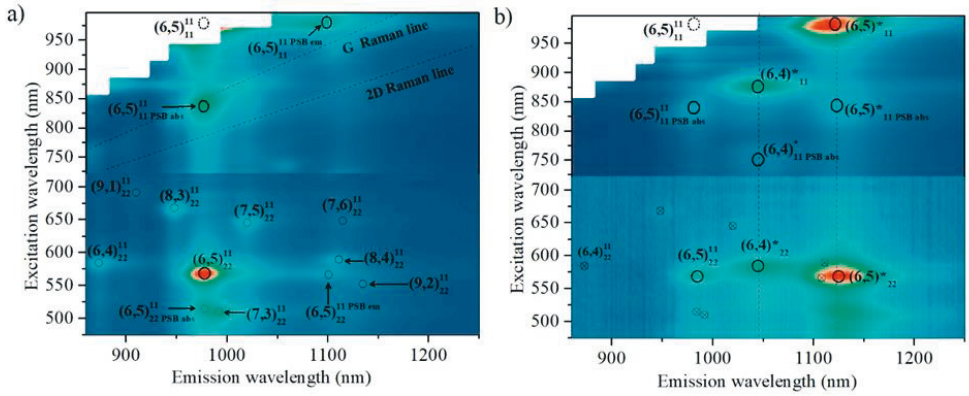

Figure 4.1 Excitation-emission PL maps of pristine SWCNTs (a) and O-functionalized SWCNTs (b). Solid horizontal lines separate maps obtained using different excitation source (Xe lamp for visible and Ti:sapphire laser for NIR), color scale normalized separately for each part. Reprinted from paper II (no permissions needed)

The spectral features noted in the original suspension were previously discussed in Section 3.1. Following the functionalization of SWCNTs with NaOCl and exposure to UV light, notable alterations in the PL

map were evident. Specifically, distinct emission bands emerged around 1045 nm and 1130 nm, as denoted by dashed vertical lines, while the original spectral features exhibited partial suppression (changes in the intensity of original spectral features will be discussed in detailes later in the text). The new emission band at 1130 nm corresponds to resonant excitation wavelengths of 568 nm, 840 nm, and 980 nm, coinciding with the resonance conditions of $(6,5)_{22}^{11}$, $(6,5)_{11\ PSB\ abs}^{11}$, and $(6,5)_{11}^{11}$, respectively (see Fig. 4.1b). Thus, we attribute the emission at 1130 nm to (6,5)-SWCNT. Similarly, the emission line centered at 1045 nm is linked to (6,4)-SWCNT. No additional emission bands related to SWCNTs of other chiralities are observable on the map due to their low concentration in the sample.

The emission wavelengths of the newly observed spectral features closely align with previously reported values for the recombination energy of excitons localized near oxygen atoms in carbon nanotubes functionalized with oxygen [104]. This substantiates the effective oxygen functionalization of SWCNTs through interaction with NaOCl under UV irradiation and facilitates the identification of the physical origin of the new emission bands as stemming from the radiative recombination of these zero-dimensional excitons. The localized exciton energy level is denoted by an asterisk (*).

4.2 Determination of optimum parameters of oxygen functionalization

To determine the optimal parameters for functionalizing SWCNTs with oxygen, experiments were conducted by varying parameters such as the concentration of sodium hypochlorite in the suspension and the duration of UV irradiation treatment. The efficiency of functionalization was assessed using the PL brightening coefficient (ϑ), defined as the ratio of the PL intensity after functionalization to that before functionalization.

$$\vartheta = \frac{A_{doped}^{(6,5)*}}{A_{pristine}^{(6,5)}} \tag{10}$$

where $A_{doped}^{(6,5*)}$ is the amplitude (maximum intensity) of the $E_{11}(6,5)$* band in the PL spectrum of O-functionalization SWCNTs and $A_{pristine}^{(6,5)}$ is the

amplitude of the E_{11}(6,5) band in the PL spectrum of pristine SWCNT (before functionalization).

Figure 4.2a illustrates the dependency of the PL brightening coefficient (ϑ) on the UV irradiation time of the suspension for various concentrations of pre-added sodium hypochlorite. It can be observed that the coefficient ϑ reaches its maximum after approximately 20-30 minutes of sample exposure to UV light, depending on the concentration of added sodium hypochlorite. For comparison, Figure 4.2b depicts the dependence of the intensity of the PL peak E_{11}(6,5) on the duration of UV irradiation, represented by a monotonically decreasing curve.

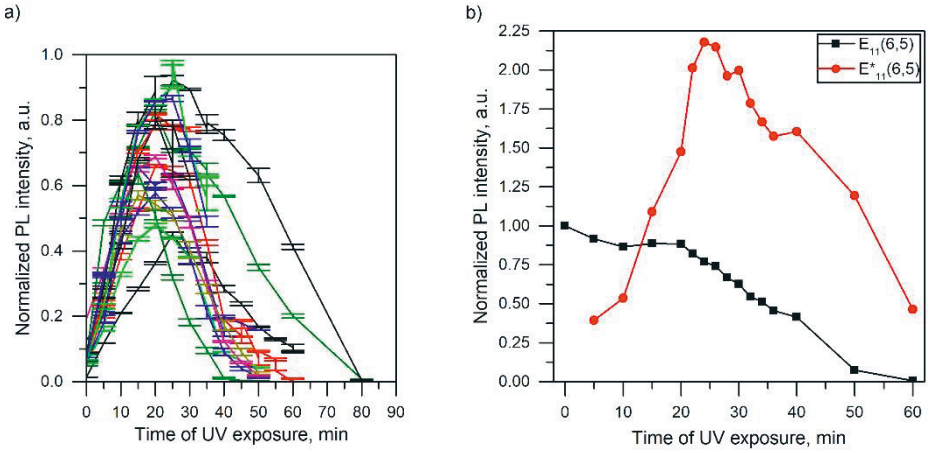

Figure 4.2 a) The dependency of the E^*_{11}(6,5) PL peak intensity on the UV exposure time at different concentration of sodium hypochlorite in the SWCNT suspension. b) the typical dependency of the intensity of the E_{11}(6,5) PL peak (black) along with the example dependence of the intensity of the E^*_{11}(6,5) (red) on the duration of UV exposure.

Figure 4.3a illustrates the influence of another important parameter – concentration of NaOCl in the suspension – on the efficiency of oxygen functionalization. By the dependence of maximum achievable peak PL intensity on a concentration of NaOCl it was established that the optimal parameters of oxygen functionalization are 0.1 mg/L concentration of NaOCl in SWCNT suspension and 25 minutes of UV exposure duration.

In Figure 4.3b, the PL spectrum of SWCNTs functionalized with oxygen under optimized parameters is shown by the red line, contrasted with the PL spectrum of pristine SWCNTs represented by the blue line. The

peak intensity of the $E_{11}(6,5)^*$ band in the PL spectrum of oxygen-functionalized SWCNTs surpasses that of the $E_{11}(6,5)$ band in pristine SWCNTs by more than twofold. It's worth mentioning that a control experiment was conducted where SWCNTs were exposed to UV light under identical conditions but without NaOCl (instead, deionized water was added to the SWCNT suspension in the same volume), and no $E_{11}(6,5)^*$ and $E_{11}(6,4)^*$ peaks were observed in the PL spectrum (indicated by the yellow reference line in Fig. 1d). Furthermore, there were no notable alterations in the PL spectrum of SWCNTs after 10 hours of interaction with NaOCl at the same concentration without UV exposure. This validates the necessity of both NaOCl and UV light for the effective oxygen functionalization of SWCNTs.

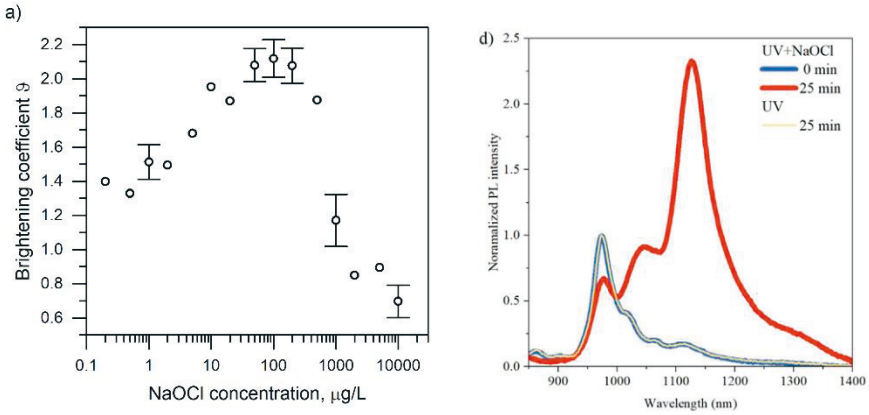

Figure 4.3 a) The dependencies of PL brightening coefficient on the concentration of NaOCl in the suspension b) Comparison of SWCNT PL spectra before O-functionalization (blue line) and after functionalization at optimum parameters at optimum parameters (red line). The excitation wavelength is 840 nm. Reprinted from paper II (no permissions needed)

4.3 Comparison of photoluminescence brightening efficiency to previously reported data

The most scientifically significant approach to compare the obtained PL enhancement with previously reported data is to assess the relative alterations in PL QY, which can be computed as:

$$\frac{QY(fun)}{QY(pristine)} = \frac{I_{fun}^{(6,5*)}}{I_{fun}^{(6,5)}} \tag{11}$$

Here, $I_{doped}^{(6,5*)}(6,5)^*$ represents the integrated intensity of the $E_{11}(6,5)^*$ peak in the spectrum of functionalized SWCNT, while $I_{pristine}^{(6,5)}$ denotes the integrated intensity of the $E_{11}(6,5)$ peak in the spectrum of pristine SWCNT.

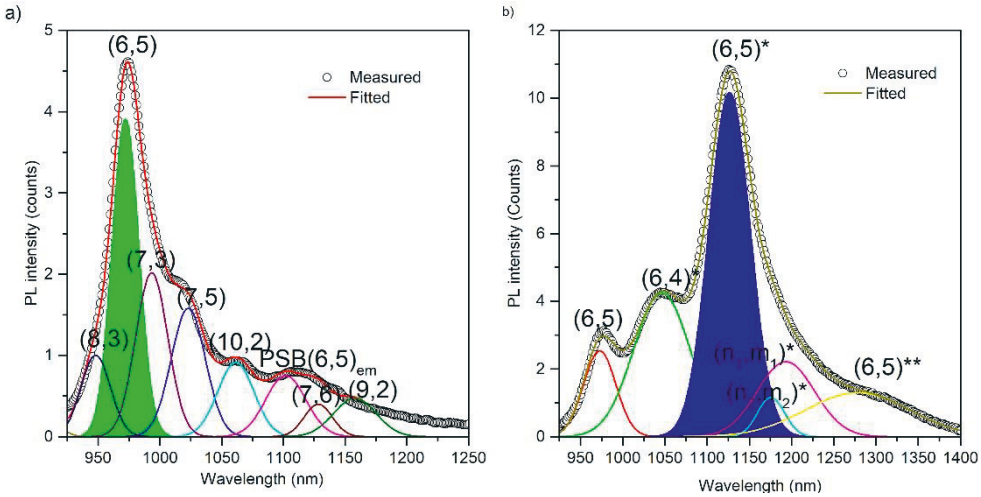

Figure 4.4 Deconvolution of PL spectra of SWNT suspension before (a) and after (b) oxygen functionalization procedure. $E_{11}(6,5)^*$ peak corresponds to ether-d configuration of oxygen atom bonding, $E_{11}(6,5)^{**}$ corresponds to epoxide-I configuration [142] . $(n_1,m_1)^*$ and $(n_2,m_2)^*$ corresponds to oxygen induced PL peak of SWNTs with unknown geometry persist in the sample.

Since there is an overlap of emission peaks with different geometries in the PL spectra, we performed deconvolution of the spectrum into components to calculate the integrated intensities of the peaks associated with the (6,5) geometry (see Figure 4.4). This allowed us to determine the values of $I_{fun}^{(6,5*)}$ and $I_{pristine}^{(6,5)}$ and establish that under optimal functionalization parameters, the PL QY increases 6 ± 0.6 times.

Formula (11) holds true under the condition of equal optical density of the sample at the excitation wavelength. To verify this condition, UV-vis-NIR optical absorption spectroscopy measurements were conducted. Figure 4.5 illustrates the optical absorption spectra of the SWCNT suspension before and after functionalization for various reaction durations. It is evident that both E_{11} optical transitions in the spectral range of 800-1200 nm and E_{22}

optical transitions in the range of 400-800 nm are attenuated, with more pronounced changes observed in the E_{11} spectral region. This phenomenon has been previously observed in SWCNTs functionalized using other methods and is commonly attributed to the reduction of the exciton oscillator strength resulting from the depletion of electron states in the valence band of SWCNT [99]. Apart from these changes, the optical absorption spectrum remains largely unaffected, indicating no significant alterations in the morphology of the SWCNTs. Furthermore, the absence of changes in the background spectral shape associated with scattering suggests similar suspendability for both pristine and oxygen-functionalized SWCNTs.

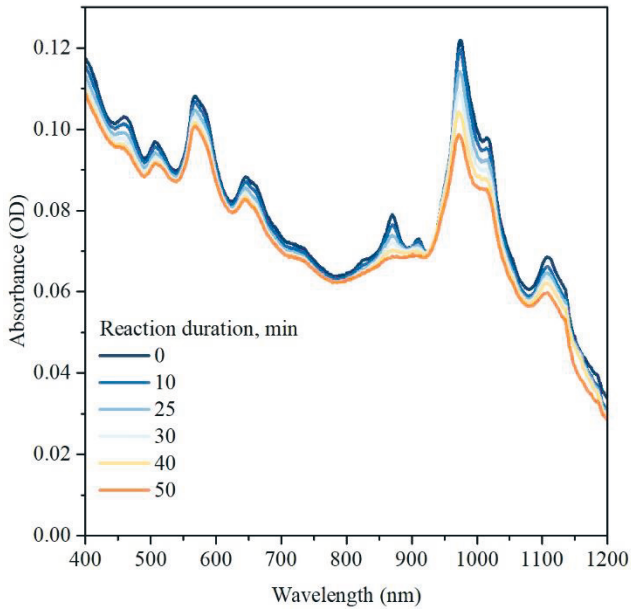

Figure 4.5 UV-vis-NIR optical absorption spectra of SWCNT with variety of oxygen functionalization strength. Reprinted from paper II (no permissions needed)

Given the decrease in the optical density of the sample at 840 nm resulting from oxygen functionalization, the actual enhancement factor of the PL QY exceeds the estimation obtained with formula (11) and is even higher than the 6. However, it is not possible to directly compare this value with the findings reported in the literature due to the absence of published data regarding spectral deconvolution and integrated peak intensity values.

Instead, we propose utilizing the previously introduced PL brightening coefficient ϑ to compare the efficiency of PL enhancement with previously published data.

Table 1 Comparison of the PL brightening coefficient ϑ achieved employing oxygen doping of SWCNT

Ref.	ϑ	(n,m)	SWCNT synthesis method and dealer	Note on O-functionalization method
This work	2.12	(6,5)	CoMoCat, Merk (former Sigma-Aldrich)	NaOCl + light
(Chiu et al.)[133]	1.65	(6,5)	CoMoCat, Sigma-Aldrich	treatment with polyunsaturated fatty acids
(Lin et al.) [125]	1.35	(6,5)	CoMoCat, Sigma-Aldrich	NaOCl + light
(Miyauchi et al.) [110]	0.86	(6,5)	CoMoCat, dealer unknown	O_3+light
(Ghosh et al.) [104]	0.68	(6,5)	unknown	O_3+light
(Iwamura et al.) [102]	0.61	(6,5)	CoMoCat, Sigma-Aldrich and Southwest Nanotechnologies	O_3+light
(Iizumi et al.) [143]	0.51	(6,5)	unknown	O_3+light
(Akizuki et al.) [100]	0.33	(6,5)	CoMoCat, Southwest Nanotechnologies	O_3+light

A greater ϑ value signifies a greater $\frac{QY(fun)}{QY(pristine)}$ value, but in terms of practical implications, like the use of O-SWCNTs as IR light sources, comparing ϑ values is more pertinent as it reflects alterations in PL brightness under consistent excitation conditions. Additionally, ϑ values obtained from previous studies can be precisely extracted from PL spectra, lending credibility to such a comparison. In this study, we attained a highly consistent ϑ value of 2.12±0.11 (Fig. 4.3b). Table 1 presents a comparison of

ϑ values across various publications on oxygen functionalization of SWCNT. As indicated in Table 1, our approach showcases the most substantial enhancement in PL emission. Note that similar source and types of SWCNT used in the cited papers indicate that the differences in the PL brightening coefficients are due to differences in the oxygen functionalization techniques rather than in the initial state of SWCNT.

4.4 Discussion on the reason for the advanced PL intensity enhancement

The higher ϑ values achieved in our study compared to those reported in previous studies [100], [102], [104], [110], [133], [143], [144] can be attributed to fundamental differences in the chemical reactions employed. Oxygen functionalization of SWCNT through ozonization involves multiple steps, including the formation of an ozonide adduct on the SWCNT surface, subsequent O2 loss resulting in an epoxide adduct, and photoisomerization of the epoxide adduct into either one [104]. Each stage of this reaction occurs on the SWCNT surface and may lead to the formation of both bright excitonic states and dark trapping defects. These defects hinder the conversion of diffusive $E_{11}(6,5)$ excitons into localized $E_{11}(6,5)^*$, thus limiting the resulting PL brightness [86]. In contrast, the NaOCl-based method involves a single-step reaction between carbon walls and atomic oxygen, generated at a distance from the SWCNT surface during the photodissociation of the hypochlorite ion. This variation in reaction mechanisms explains the higher ratio of bright to dark defects when using NaOCl as an oxygen source, consequently resulting in higher PL brightening coefficients.

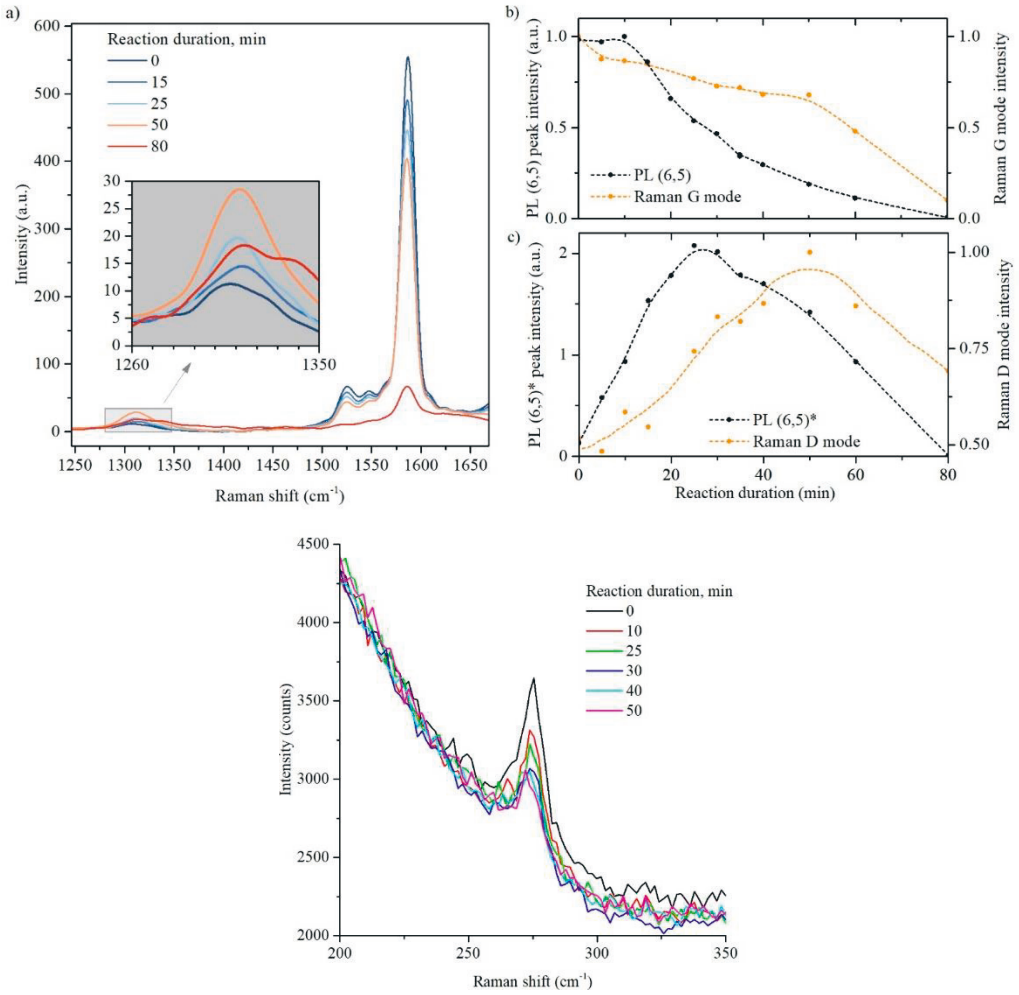

Figure 4.6 a) Spectra Raman of pristine and oxygen-functionalized SWCNTs; b) The relationship between PL E_{11}(6,5) intensity and Raman G-mode intensity concerning the duration of the functionalization reaction; Reprinted from paper II (no permissions needed) c) The relationship between PL E_{11}(6,5)* intensity and Raman D-mode intensity concerning the duration of the functionalization reaction. Dashed lines are provided as a visual aid. d) Raman spectra of pristine and functionalized SWCNT with different duration of functionalization procedure in RBM spectral region. Single peak at 270 cm^{-1} is radial breathing mode (RBM) peak.

Nevertheless, despite employing the same functionalization reaction as in [125], based on the photodissociation of hypochlorite ions, we observed significant variations in the obtained ϑ values. To elucidate the underlying cause of this difference, we utilized Raman spectroscopy to

investigate the intricacies of defect formation during oxygen functionalization.

The evolution of the Raman spectra is depicted in Fig. 4.6a. A gradual reduction in the tangential G-mode intensity was observed throughout the functionalization reaction, correlating with changes in the intensity of the E_{11}(6,5) PL band (Fig. 4.6b). Furthermore, the intensity of the RBM mode in the Raman spectra steadily decreased with prolonged UV exposure duration (see Fig. 4.6d). The concurrent attenuation of both the RBM and G modes in the Raman spectrum can be interpreted as indicative of effective SWCNT functionalization [145], [146], [147]. Notably, there were no significant alterations observed in the RBM spectral region of the Raman spectrum during oxygen functionalization, suggesting the preservation of SWCNT morphology within the sample. Utilizing the Raman shift of the RBM mode (275 cm-1), we estimated the diameter of the analyzed SWCNT to be 0.86 nm, consistent with the findings obtained from PL mapping.

Data on defects formation in SWCNT can be garnered by examining alterations in the spectral region corresponding to the "defective" (D) mode, as illustrated in the insert of Fig. 4.6a. Initially, the intensity of the D-mode increased during the initial 50 minutes of the reaction before exhibiting a subsequent decline, mirroring the behavior of the E_{11}(6,5)* PL peak (Fig. 6.6c). Estimation of the defect density in SWCNT can be achieved by comparing the integrated intensities of the D and G bands, utilizing the calibration curve detailed in [148]. For SWCNT subjected to moderate functionalization (25 minutes of UV exposure), the density of oxygen defects is approximated to be 30 μm^{-1}.

This observation supports the idea that the emergence of the E_{11}(6,5)* PL peak is a result of defect formation through the covalent bonding of oxygen atoms to the walls of SWCNTs. However, beyond 25 minutes of UV exposure, although the intensity of the E_{11}(6,5)* peak in the PL spectrum began to decrease, the intensity of the D-mode continued to increase. This phenomenon cannot be attributed to the amorphization of SWCNTs' crystalline structure due to a high number of oxygen defects, as there are no indications of amorphization in the shapes of the D and G bands until 50 minutes of UV exposure. The disruption of the SWCNTs' structure becomes

evident only after 50 minutes of UV illumination. This is marked by a sharp decrease in both the D and G band intensities, a significant increase in the D/G intensity ratio, and notable alterations in the shape of the D-band in the Raman spectrum (indicated by the red line in Fig. 4.6a).

To investigate whether the decrease in the E_{11}(6,5)* PL peak intensity is due to the depletion of NaOCl reactant during the initial 25 minutes [125], we conducted additional experiments. We added an extra portion of non-irradiated NaOCl to the SWCNT suspension midway through the oxygen-functionalization process (at 30 minutes of UV irradiation). However, this did not reverse the declining trend of the E_{11}(6,5)* peak intensities over time of UV irradiation (refer to Fig. 4.7). This finding suggests that the scarcity of NaOCl reactant is not a limiting factor for the growth of the E_{11} (6,5)* peak.

We hypothesize that the close proximity of oxygen defects may disrupt the localizing potential and electronic structure of the oxygen-functionalized sites, thereby hindering effective radiative emission and limiting the growth of the E_{11} (6,5)* peak intensity, despite an increase in the total number of oxygen defects. This suggests that achieving homogeneous functionalization is crucial for obtaining bright emissions from the oxygen-functionalized sites of SWCNTs.

This explanation could elucidate the higher PL brightening coefficient (ϑ) achieved in our study compared to previously published results. Specifically, the utilization of prolonged (25 min) and gentle (27 μW/cm^2) UV exposure in our work is expected to yield more uniform oxygen functionalization compared to the brief (40 s) and intense (29 mW/cm^2) UV exposure used in [125]. This difference in UV exposure conditions likely contributes to the notable contrast in ϑ values (2.12 in our study compared to 1.36 in [125]), despite the similar D/G intensity ratio.

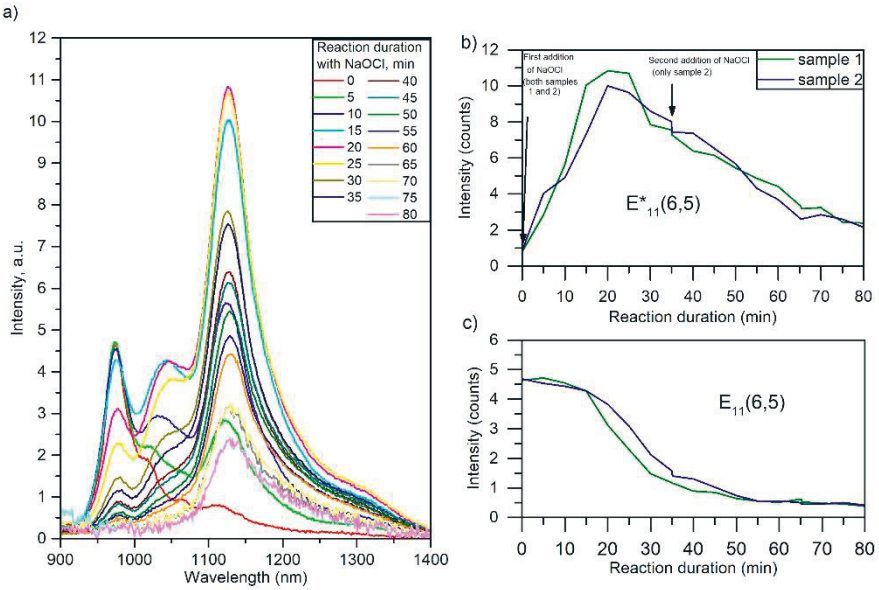

Figure 4.7 a) Control experiments were conducted to test whether the consumption of NaOCl acted as a limiting factor in the growth of PL intensity. In panel (a), the PL spectra of SWNT suspension with added NaOCl are shown, irradiated with a UV lamp for varying durations. Panels (b) and (c) depict the dependency of the $E_{11}(6,5)^*$ and $E_{11}(6,5)$ PL peak intensities, respectively, on the duration of UV exposure. An additional amount of NaOCl was added to sample 2 after 35 minutes of reaction duration.

Utilizing oxygen-functionalized SWCNTs synthesized through NaOCl treatment and prolonged, gentle UV exposure could potentially enhance tissue imaging contrast compared to conventional methods. Moreover, in the realm of single photon sources, this approach may enable emission at higher frequencies. However, for the successful integration of O-SWNTs into industrial applications such as bioimaging probes, single-photon emitters, IT LEDs, and IR nanolasers, further enhancement of O-SWNT PL brightness is necessary. The findings of this study suggest an efficient strategy for achieving this by optimizing the duration and intensity of UV exposure to improve the uniformity of SWCNT O-functionalization. This method presents a promising avenue for surpassing the brightness of sp3-functionalized SWCNTs while maintaining the simplicity and speed of O-functionalization technology.

The refined approach to SWCNT oxygen-functionalization showcased in this study leads to the emergence of a red-shifted PL band with a peak intensity exceeding twice that of the pristine sample. Notably, the PL brightening coefficient of 2.12±0.11 achieved here stands as the highest among all prior studies utilizing the O-functionalization technique. Insights from Raman spectroscopy investigations into defect formation suggest that this enhancement stems from a more uniform distribution of oxygen atoms along the SWCNTs, facilitated by prolonged and gentle UV exposure. We posit that further optimization of the O-functionalization process, specifically by fine-tuning the duration and intensity of UV exposure, holds significant promise for elevating the brightness of O-SWCNT PL. Importantly, this optimization can be achieved while preserving the technological simplicity and rapidity inherent in this approach, thus meeting the requirements of diverse technological applications including IR LEDs, IR nanolasers, IR single-photon sources, and bio-imaging probes.

4.5 Ultrafast exciton dynamics in oxygen-functionalized single-walled carbon nanotubes

Figure 4.8 depicts a two-dimensional color map of transient absorption (TA) in the pristine SWCNT suspension, where the probe wavelength spans the NIR and visible spectral regions and the pump wavelength is set to 400 nm. Negative TA spectral features, indicating exciton population in SWCNTs of different chiralities, are marked with dashed lines and denoted as $E_{ii}(n,m)$, where (n,m) represents the SWCNT chirality and the subscript ii defines the type of excitonic transition (E_{11} for band-edge and E_{22} for deep-band excitons). The assignment of chiral indexes (n,m) to the TA features is based on PL map (see Fig. 4.1). Additionally, basic TA features of SWCNTs, such as the biexciton formation signal at ~1060 nm, are observed, although not analyzed in this study. Our focus in this research is on SWCNTs of the predominant chirality (6,5), which exhibit the most intense photo response. These nanotubes exhibit induced

transmittance features centered at 980 nm and 565 nm, corresponding to the E_{11} and E_{22} excitonic transitions, respectively [126]. The population dynamics of E_{11} and E_{22} can be inferred from the time dependence of the measured TA signal at the corresponding wavelengths. It's worth noting that, despite the TA response of SWCNTs in the E_{11} spectral region being a superposition of spectrally shifted positive and negative TA signals, the ratio of amplitudes of these signals does not show strong time dependence. [57], [149]

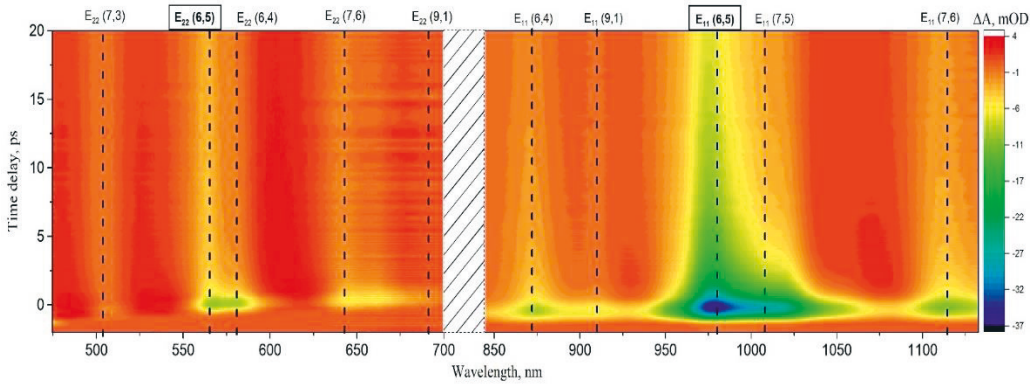

Figure 4.8 a) Two-dimensional color maps depict the variation of pump-induced transient absorption (TA) in the suspension of pristine SWCNTs as a function of probe wavelength and time delay between the pump and probe pulses. The notations $E_{ii}(n,m)$ denote the chirality and type of optical transition of the SWCNTs. The pump wavelength is set to 400 nm. Reprinted from paper III (no permissions needed)

Figures 4.9a and 4.9b display the relationship between the induced transmittance signal at specific wavelengths (980 nm and 565 nm, respectively) and the time delay between the pump and probe pulses for SWCNT suspensions with varying densities of embedded oxygen defects. These figures highlight the impact of oxygen functionalization on the population dynamics of E_{11} and E_{22} excitons. Remarkably, even at low levels of functionalization, the dynamics of E_{11} exhibit noticeable changes, while the dynamics of E_{22} remain relatively unaffected until the duration of functionalization surpasses 25 minutes.

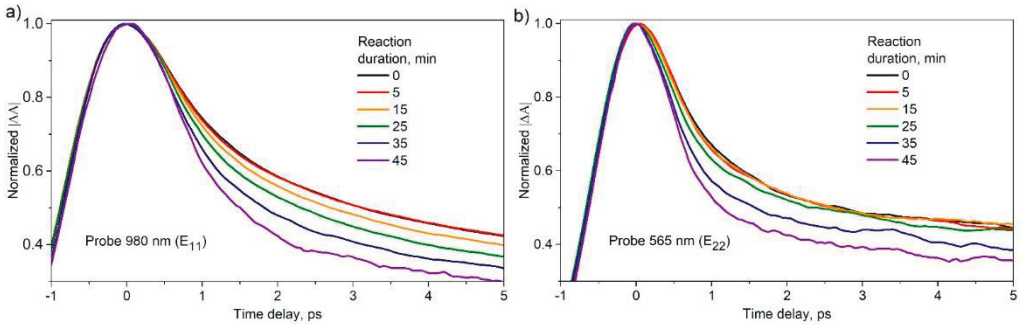

Figure 4.9 Kinetic profiles at 980 nm (a) and 565 nm (b) probe wavelengths for SWCNT and O-SWCNT with varying degrees of oxygen functionalization. The pump wavelength is 400 nm. Reprinted from paper III (no permissions needed)

We now turn our attention to quantitatively characterizing the changes in the dynamics of E_{11} and E_{22} excitons. Previous studies by Sykes et al. demonstrated that the ultrafast dynamics of excitons in sp^3-SWCNTs can be effectively modeled through a global analysis of the entire spectral range, considering various decay channels such as first-order exciton decay, exciton-exciton annihilation, Auger recombination, and trapping by defects [87]. While this approach proves successful for monochiral SWCNT suspensions, its applicability becomes impractical in the presence of SWCNTs with different chiralities, given the significantly increased number of fitting parameters. To tackle this challenge, we propose a simplified approach wherein the exciton dynamics in oxygen-functionalized SWCNTs are regarded as a convolution of the complex exciton dynamics in pristine SWCNTs and a putative functionalization-induced exciton relaxation channel. Formally, this approach can be expressed as follows:

$$N_{11}^{T}(t) = A_{11} * e^{-\frac{t}{\tau_{11}}} + (1 - A_{11}) * N_{11}^{0}(t) \quad (12)$$

$$N_{22}^{T}(t) = A_{22} * e^{-\frac{t}{\tau_{22}}} + (1 - A_{22}) * N_{22}^{0}(t) \quad (13)$$

In this expression, t represents the time delay between the pump and probe pulses, T indicated the duration of the oxygen functionalization reaction, $N_{nn}^{T}(t)$ denotes the population dynamics of E_{nn} excitons in O-SWCNT, while $N_{nn}^{0}(t)$ represents the population dynamics of E_{nn} excitons in pristine SWCNT. The fitting parameters, A_{nn} and τ_{nn}, capture the contribution and lifetime, respectively, of an additional decay channel resulting from oxygen functionalization. The factor $(1 - A_{nn})$ signifies the reduction in the relative contribution of decay channels typical for pristine SWCNTs due to

oxygen functionalization. We note that our usage of a model considering an exponential law of exciton decay rather than the power law is in alignment with prior literature. Indeed, the power decay law was reported for ultrapure monochiral SWCNT suspensions [57], while exponential decay law is more typical for the SWCNT samples processing several SWCNT chiralities [62], [69], [150].

By applying this model to fit the experimental data on exciton dynamics, we determined the values of fitting parameters A_{nn} and τ_{nn} for SWCNTs with varying degrees of oxygen functionalization. Figure 4.10 represents typical fitting results of experimental results by model expressed by formulas (12) and (13). The approximation was performed using the original MATLAB code presented in the Appendix 1.

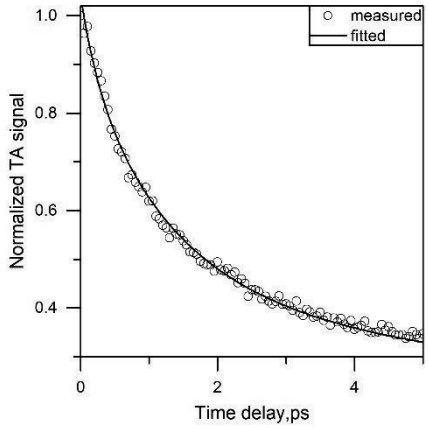

Figure 4.10 Typical fitting results of dynamics in oxygen-functionalized SWCNTs employing the model described by equations (1) and (2). Circles represent experimental data, while line indicates the fitting data.

Figures 4.11 a and 4.11 b illustrate the dependencies of the relative contributions A_{nn} and the lifetime τ_{nn} of the functionalization-induced decay channel on the duration of the reaction. Notably, significant differences emerge in the evolution of the additional decay channel for E_{11} and E_{22} excitons. Specifically, for the E_{11} exciton case, the amplitude A_{11} of the additional decay channel consistently increases from the beginning of the reaction. On the other hand, the functionalization-induced decay channel in the dynamics of the E_{22} exciton becomes active only after approximately 25-30 minutes of the reaction, followed by an increase. The lifetime of the

additional decay channel shows a step-like dependence on the degree of functionalization. At low degrees of functionalization, when the amplitude of the functionalization-induced decay channel is negligibly small, the lifetime remains in the order of several picoseconds, indicating minimal impact on the dynamics. However, once the additional channel is activated, its lifetime decreases, fluctuating within the range of 400-600 fs for the E_{11} exciton and 100-150 fs for the E_{22} exciton.

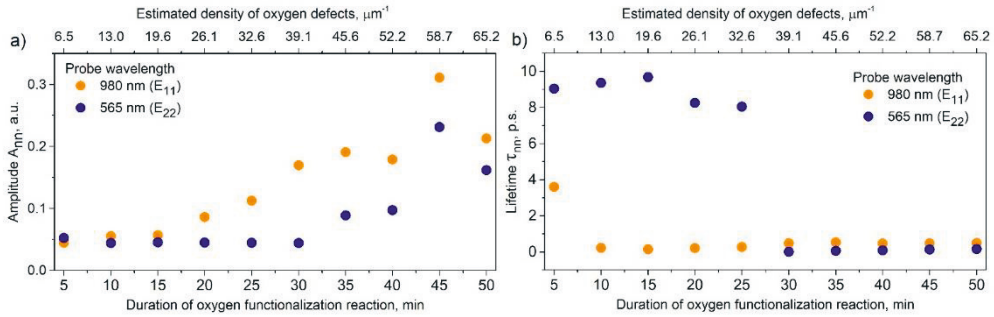

Figure 4.11 The evaluated amplitudes (a) and lifetimes (b) of the functionalization-induced decay channel for E_{11} (orange) and E_{22} (blue) excitons are depicted as a function of the duration of the functionalization reaction. The density of oxygen defects is estimated according to [108]. Reprinted from paper III (no permissions needed)

We propose that the changes observed in the dynamics of E_{11} and E_{22} excitons, as the degree of functionalization varies, stem from the interplay between diffusive excitons and oxygen defects, leading to the emergence of a functionalization-induced decay channel. This explanation is supported by the distinct behaviors exhibited by E_{11} and E_{22} excitons. Initially, E_{22} excitons undergo rapid relaxation to the lower-energy E_{11} state through phonon scattering [74]. However, as they belong to the lowest exciton manifold of pristine SWCNTs, E_{11} excitons do not experience fast phonon relaxation and can diffuse over longer distances along SWCNTs. Consequently, at low degrees of functionalization, photoexcited excitons are more likely to encounter oxygen defects while in the E_{11} state than in the E_{22} state. Conversely, at higher degrees of functionalization, the proximity of oxygen defects becomes more pronounced, increasing the likelihood that diffusive E_{22} excitons reach the defects before relaxing to the E_{11} manifold. These considerations provide a qualitative explanation for why the amplitude of

the functionalization-induced channel of E_{11} excitons begins to increase at lower degrees of functionalization compared to the activation of the functionalization-induced decay channel of E_{22} excitons (see Fig. 4.11). This reasoning supports the attribution of the functionalization-induced channel to the interaction between diffusive excitons and oxygen defects.

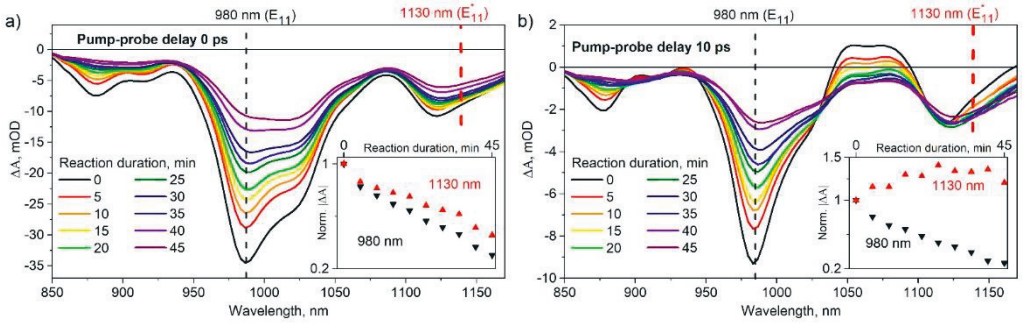

Figure 4.12 TA spectra of SWCNT suspensions with varying degrees of oxygen functionalization at 0 ps (a) and 10 ps (b) time delay between probe and pump pulses. Pump wavelength is 400 nm. Inserts show the dependence of the normalized amplitudes of the TA signals at 980 nm and 1130 nm. Reprinted from paper III (no permissions needed)

The interaction between excitons and defects may result in shortened exciton lifetimes, either due to exciton trapping by defective potentials or exciton recombination induced by scattering on the defects. To determine which of these processes occurs, we analyzed the evolution of TA spectra with increasing degrees of functionalization at fixed pump-probe delay times of 0 and 10 ps (Fig. 4.12a and 4.12b, respectively). It can be observed that at zero delay time (see Fig. 4.12a), the amplitude of the TA signal decreases monotonically with rising degrees of functionalization. Importantly, this observation holds true for the entire spectrum, encompassing excitonic transitions in SWCNTs of all chiralities (see insert in Fig. 4.12a). At a delay time of 10 ps, the suppression of excitonic transitions is also noticeable with increasing degrees of functionalization. However, this pattern does not extend to the region of 1100-1170 nm, where some changes in the shape of the band and even an increase in the induced transmittance signal with the reaction duration are observed (see insert in Fig. 4.12b). This suggests the emergence of a new functionalization-induced negative TA spectral feature, labeled as E_{11}*, within the 1100-1170 nm

region. However, this feature partially overlaps with the spectral feature of the E_{11} excitonic transition in (7,6)-SWCNT, centered at 1115 nm (see Fig. 4.8). To isolate the signal of the functionalization-induced spectral feature E_{11}*, the signal arising from (7,6)-SWCNT should be subtracted:

$$N^{T}_{E^{*}_{11}}(t) = \Delta A^{\square}_{\lambda}(t) - N^{T}_{(7,6)}(t), \qquad (14)$$

where *t* is the time delay between the pump and the probe pulses, *T* is the duration of the oxygen functionalization procedure, $\Delta A^{\square}_{\lambda}(t)$ is a TA signal measured at the wavelength λ belonging to the region 1100-1170 nm, $N_T(t)$ reflects the time dependency of the noted spectral feature of oxygen functionalization level determined by T value.

Note that the impact of functionalization on the exciton dynamics in (7,6)-SWCNT should be considered before subtraction. To perform these calculations we quantitatively characterize the impact of the functionalization on the E_{11} exciton dynamics introducing the correction function $F^{T}_{(n,m)}(t)$ as follows:

$$F^{T}_{(n,m)}(t) = \frac{N^{T}_{(n,m)}(t)}{N^{0}_{(n,m)}(t)} \qquad (15)$$

Here $N^{T}_{(n,m)}(t)$ reflects the exciton population dynamics oxygen-functionalized sample and $N^{0}_{(n,m)}(t)$ – in the pristine sample. These calculations were performed using the original MATLAB script presented in Appendix 2.

Figure 4.13a shows calculated correction functions $F^{25}_{(6,5)}(t)$ and $F^{25}_{(6,4)}(t)$. Note that the correction functions calculated for two most prominent charities in the sample, that are (6,5) and (6,4) are very similar, and this is valid not only for T=25 min but for other durations of functionalization procedure as well. Assuming that functionalization affects exciton dynamics in (7,6)-SWCNT in a similar way as it affects exciton in dynamics in (6,5) or (6,4), we consider general correction function $F^{T}(t) = F^{T}_{(6,5)}(t) \approx F^{T}_{(6,4)}(t) \approx F^{T}_{(7,6)}(t)$ and estimate exciton population dynamics in functionalized (7,6)-SWCNT as follows:

$$N^{T}_{(7,6)}(t) = N^{0}_{(7,6)}(t) * F^{T}(t) \qquad (16)$$

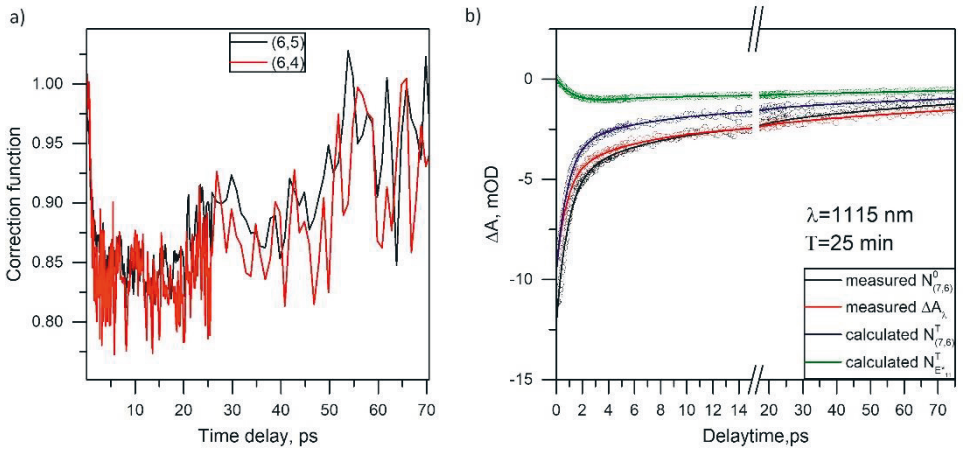

Figure 4.13 a) Correction functions $F^{25}_{(6,5)}(t)$ *and* $F^{25}_{(6,4)}(t)$ calculated according to formula (15) b) Illustration of the calculation steps for the time dependence of the E_{11}^* spectral feature according to equations (14), (15), and (16)

Finally, to calculate the time dependency of the spectral feature E_{11}^* noted in Fig. 4.12b within the 1100-1170 nm region we substitute formula (16) into formula (14). Figure 4.13b illustrate an example of the calculation result for T=25 and λ =1115 nm. Calculations were performed using MATLAB function presented in Appendix 3. We performed described calculation procedure for each λ value within 1100-1170 nm region and for each duration T of oxygen functionalization reaction from 5 to 45 min (refer to Appendix 4 for the corresponding MATLAB script).

As a representative example of the results of these calculations, Figure 4.14a presents a two-dimensional color plot of the assessed E_{11}* spectral feature at T=25 min. Interestingly, the assessed E_{11}* spectral feature turned out to be centered at 1130 nm, which consistent with the emission wavelength of the functionalization-induced PL band observed in the PL spectra of O-SWCNTs (see Fig. 4.1a). [102], [104], [110], [125] Note that the information about the peak position was not included in the input data or in the MATLAB code used to calculate E_{11}* signal, which supports the validity of the applied calculation procedure.

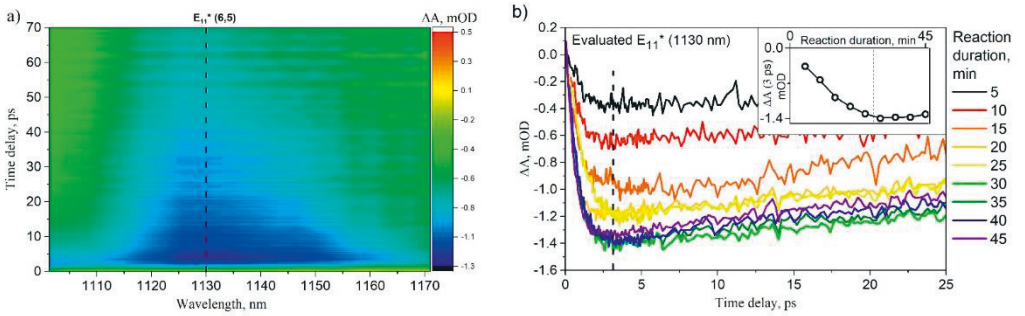

Figure 4.14 a) Depiction of a two-dimensional color map representing the assessed TA signal attributed to the E_{11}* exciton population in oxygen-functionalized SWCNT (reaction duration of 25 minutes). b) Illustration of the evaluated dynamics of the E_{11}* exciton in SWCNT with various levels of oxygen functionalization. Inset: The relationship between the amplitude of the E_{11}* feature at the delay of 3 ps and the duration of the functionalization reaction. Reprinted from paper III (no permissions needed)

It's noteworthy that there is no indication of a corresponding peak around 1130 nm in steady-state absorption spectra of oxygen-functionalized SWCNTs (see Fig. 4.5). This stands as a significant divergence between O-SWCNT and sp^3-SWCNT, as sp^3-SWCNTs exhibit a distinct red-shifted absorption peak in steady-state absorption spectra [81], [89], [107], a characteristic not reported in works dedicated to O-SWCNTs [104], [110], [143]. Similarly, a distinct E_{11}* spectral feature in TA spectra of sp^3-SWCNTs was previously observed by Sykes et al. [87], but so far, there have been no reports regarding this matter in O-SWCNTs. We address this knowledge gap by observing the E_{11}* spectral feature in TA spectra of O-SWCNTs (see Fig. 4.14a). It's also notable that the E_{11}* spectral feature displays time-domain characteristics similar to those previously reported for defect-localized excitons (see Fig. 4.14b): a formation time on the order of several picoseconds, similar to what was revealed by pump-probe spectroscopy of sp^3- SWCNTs [87], and a decay time on the order of several tens or hundreds of picoseconds, akin to that unveiled by time-resolved PL spectroscopy of both O-SWCNTs and sp^3-SWCNTs [84], [85], [108], [109]. These observations suggest that the E_{11}* spectral feature corresponds to the formation of excitons localized by the deep trap potentials of oxygen defects.

The relationship between the amplitude of the E_{11}* spectral feature and the duration of the functionalization reaction offers important insights concerning differences in the interaction of E_{11} and E_{22} excitons with embedded oxygen defects (refer to Fig. 4.14b). The E_{11}* amplitude increases with a higher degree of oxygen functionalization until the reaction time reaches 30 minutes (see insert in Fig. 4.14). Concurrently, as previously discussed and shown in Figs. 4.9 and 4.11, these levels of functionalization result in a shortened E_{11} exciton lifetime without significantly affecting the E_{22} exciton lifetime. This leads us to conclude that the functionalization-induced decay channel in E_{11} dynamics arises from exciton trapping, which subsequently populates the defect-localized excitonic state E_{11}*.

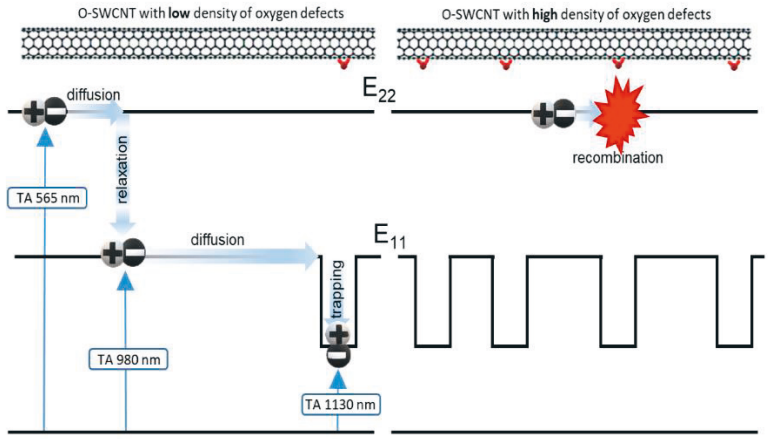

Figure 4.15 Simplified schematic illustration of the E_{11} and E_{11}* exciton interaction process with quantum defects. Reprinted from Paper III (no permissions needed).

Additionally, we observe that when the functionalization level is sufficient to affect the dynamics of E_{22} excitons (reaction time exceeding 30 minutes, see Figs. 4.9 and 4.11), the E_{11}* amplitude dependence on the degree of functionalization shifts, showing a slight decrease instead of an increase (see Fig. 4.14b). This suggests that deep-band E_{22} exciton trapping is much less efficient than band-edge E_{11} exciton trapping. The decrease in E_{22} exciton lifetime with increasing functionalization is thus attributed to exciton recombination via scattering on oxygen defects, similar to exciton quenching on natural nonradiative defects [151]. We propose that these unexpected differences in the interactions of E_{11} and E_{22} excitons with

oxygen defect sites, not previously addressed in the literature, are due to differences in the exciton wave functions and the spectra of excitonic states in the E_{11} and E_{22} manifolds [16].

The findings presented in this paragraph are schematically summarized in Figure 4.15. Our research demonstrates that E_{11} excitons interacting with oxygen defect sites result in the population of defect localized E_{11}* via an exciton trapping process. In contrast, the interaction of E_{22} excitons with defective potentials leads to exciton dissociation. This suggests that the ideal density of quantum defects is intricately linked to the mean free path of E_{11} and E_{22} excitons. Various factors influence this relationship, including the diameter of the SWCNT, the local environment, the presence of non-emissive defects, and the length of the SWCNT. These complex interdependencies highlight the necessity for a nuanced and comprehensive approach when customizing functionalized SWCNTs for specific applications. Precisely selecting the concentration and distribution of quantum defects within the SWCNT structure is crucial for achieving optimal performance in devices such as nanolasers, single photon sources, LEDs, and bioimaging probes.

CONCLUSION

In this work, a comprehensive study of SWCNTs modified by two different methods was conducted: non-covalent doping with HCl and covalent functionalization with oxygen. It was found that the addition of HCl to the SWCNT suspension results in the physisorption of hydrogen ions onto the surface of the SWCNTs. This adatom acts as a spatial inhomogeneity, locally perturbing the lattice potential of the SWCNTs and enabling new quantum states that are absent in other parts of the SWCNTs. The energy structure and physical nature of these embedded levels were investigated in this study. We discovered that localization of the edge exciton E_{11} occurs in the vicinity the hydrogen adatom, leading to changes in its excitation and recombination energy compared to the exciton in the undoped part of the SWCNTs, as can be directly observed by appearance of a new red-shifted bands in PL and absorption spectra of SWCNT upon doping. Additionally, we found another energy level T introduced by doping, located in the same localizing potential but at a lower energy. We established that this state is populated during relaxation from the localized exciton level X with a delay of about 1 ps. We suggest that this delay corresponds to the binding of the exciton with a hole, forming a new quasiparticle - a trion. Interestingly, the trion in such SWCNTs cannot be optically excited directly from the ground state of the SWCNTs and does not recombine with light emission. Its detection was made possible by observing the induced absorption signal corresponding to the transition from the trion level T to a higher excited trion level T*.

While the interaction of SWCNTs with HCl results in a significant suppression of photoluminescence intensity, which is disadvantageous for practical applications of such a material, covalent doping of SWCNTs with oxygen shows the opposite trend, with a noticeable increase in the photoluminescence signal intensity due to the emergence of a red-shifted emission peak. In this work, an improved technology for the oxygen functionalization of SWCNTs was proposed, which allows increasing the peak photoluminescence signal intensity of SWCNTs by more than 2 times,

higher than any previously published works on oxygen functionalization of SWCNTs. This achievement is attributed to the more uniform distribution of oxygen defects along the SWCNTs.

The process of exciton capture by oxygen traps was investigated in detail in this work. We found that both band-edge E_{11} and deep-band E_{22} excitons interact with oxygen traps, but there are significant differences in these processes. Edge excitons E_{11} interact with oxygen defects even at low defect densities, leading to trapping and the population of localized exciton states E_{11}*. On the other hand, as established in this work, intra-band excitons are insensitive to oxygen defects at densities below a critical value determined by the free path length of E_{22} excitons. At oxygen functionalization levels exceeding the critical value, the interaction of E_{22} excitons with oxygen defects differs from the E_{11} case and leads to the dissociation of E_{22} excitons rather than trapping and population of the E_{11}* level.

The results obtained in this work are of interest both from a fundamental and a practical perspective. The new data on the interplay of quantum defects and SWCNTs complement the experimental base necessary for a complete and consistent theoretical description of hybrid dimensional structures, specifically one-dimensional physical systems with zero-dimensional inclusions. On the other hand, the advanced technology for the introduction of quantum defects proposed in this work and the discovered differences in the nature of the interaction of various excitons with defect potentials are critically important for practical applications such as the development of nanolasers, single-photon sources, or the creation of biomarkers based on O-SWCNTs.

BIBLIOGRAPHY

[1] S. Reich, J. Maultzsch, and C. Thomsen, *Carbon Nanotubes: Basic Concepts and Physical Properties*. Willey-VCH, 2008.

[2] R. Zhang, Y. Zhang, Q. Zhang, H. Xie, W. Qian, and F. Wei, 'Growth of Half-Meter Long Carbon Nanotubes Based on SchulzÀFlory Distribution', 2013, doi: 10.1021/nn401995z.

[3] A. De Vita, J.-C. Charlier, X. Blase, and R. Car, 'Electronic structure at carbon nanotube tips', *Appl. Phys. A*, vol. 68, pp. 283–286, 1999.

[4] N. Hamada, S.-I. Sawada, and A. Oshiyama, 'New One-Dimensional Conductors: Graphitic Microtubules', vol. 68, no. 10, 1992.

[5] Ge. G. Samsonidze *et al.*, 'The Concept of Cutting Lines in Carbon Nanotube Science', *J Nanosci Nanotechnol*, vol. 3, no. 6, pp. 431–458, 2003, doi: 10.1166/jnn.2003.231.

[6] M. S. Dresselhaus, G. Dresselhaus, R. Saito, and A. Jorio, 'Raman spectroscopy of carbon nanotubes', *Phys Rep*, vol. 409, no. 2, pp. 47–99, 2005, doi: 10.1016/j.physrep.2004.10.006.

[7] R. Saito, G. Dresselhaus, and M. S. Dresselhaus, 'Trigonal warping effect of carbon nanotubes', *Phys Rev B*, vol. 61, no. 4, pp. 2981–2990, 2000, doi: 10.1103/PhysRevB.61.2981.

[8] R. Krupke, 'Separation of Metallic from Semiconducting Single-Walled Carbon Nanotubes', *Science (1979)*, vol. 301, no. 5631, pp. 344–347, 2003, doi: 10.1126/science.1086534.

[9] A. Jorio *et al.*, 'Resonance Raman spectroscopy (n,m)-dependent effects in small-diameter single-wall carbon nanotubes', *Phys Rev B Condens Matter Mater Phys*, vol. 71, no. 7, 2005, doi: 10.1103/PhysRevB.71.075401.

[10] G. G. Samsonidze *et al.*, 'Family behavior of the optical transition energies in single-wall carbon nanotubes of smaller diameters', *Appl Phys Lett*, vol. 85, no. 23, pp. 5703–5705, 2004, doi: 10.1063/1.1829160.

[11] Y. Miyauchi, 'Photoluminescence studies on exciton photophysics in carbon nanotubes', *J Mater Chem C Mater*, vol. 1, no. 40, pp. 6499–6521, 2013, doi: 10.1039/c3tc00947e.

[12] F. Wang, G. Dukovic, L. E. Brus, and T. F. Heinz, 'The Optical Resonances in Carbon Nanotubes Arise from Excitons', *Science (1979)*, vol. 308, no. 5723, pp. 838–841, 2005, doi: 10.1126/science.1110265.

[13] J. Maultzsch *et al.*, 'Exciton binding energies in carbon nanotubes from two-photon photoluminescence', *Phys Rev B Condens Matter Mater Phys*, vol. 72, no. 24, pp. 1–4, 2005, doi: 10.1103/PhysRevB.72.241402.

[14] C. D. Spataru, S. Ismail-Beigi, L. X. Benedict, and S. G. Louie, 'Excitonic Effects and Optical Spectra of Single-Walled Carbon Nanotubes', *Phys Rev Lett*, vol. 92, no. 7, p. 077402, 2004, doi: 10.1103/PhysRevLett.92.077402.

[15] T. Ando, 'Aharonov-Bohm effects on bright and dark excitons in carbon nanotubes', 2006, doi: 10.1088/1742-6596/38/1/004.

[16] M. S. Dresselhaus, G. Dresselhaus, R. Saito, and A. Jorio, 'Exciton Photophysics of Carbon Nanotubes', *Annu Rev Phys Chem*, vol. 58, no. 1, pp. 719–747, 2007, doi: 10.1146/annurev.physchem.58.032806.104628.

[17] S. Yamashita, Y. Saito, and J. H. Choi, *Carbon nanotubes and graphene for photonic applications*. 2013. doi: 10.1017/CBO9781107415324.004.

[18] J. Jiang *et al.*, 'Chirality dependence of exciton effects in single-wall carbon nanotubes: Tight-binding model', *Phys Rev B Condens Matter Mater Phys*, vol. 75, no. 3, pp. 1–13, 2007, doi: 10.1103/PhysRevB.75.035407.

[19] J. Kü, G. Kresse, and H. Kuzmany, 'First-principles calculations of the radial breathing mode of single-wall carbon nanotubes', 1998.

[20] H. Kuzmany *et al.*, 'Determination of SWCNT diameters from the Raman response of the radial breathing mode', *Eur. Phys. J. B*, vol. 22, pp. 307–320, 2001.

[21] M. Milnera, R. Rouse, and R. Rouse, 'Periodic resonance excitation and intertube interaction from quasicontinuous distributed helicities in single-wall carbon nanotubes', *Phys Rev Lett*, vol. 84, no. 6, pp. 1324–1327, Feb. 2000, doi: 10.1103/PhysRevLett.84.1324.

[22] Y. Piao *et al.*, 'Intensity Ratio of Resonant Raman Modes for (n,m) Enriched Semiconducting Carbon Nanotubes', *ACS Nano*, vol. 10, no. 5, 2016, doi: 10.1021/acsnano.6b01031.

[23] L. M. Malard, M. A. Pimenta, G. Dresselhaus, and M. S. Dresselhaus, 'Raman spectroscopy in graphene', *Phys Rep*, vol. 473, no. 5–6, pp. 51–87, 2009, doi: 10.1016/j.physrep.2009.02.003.

[24] V. Skákalová, Y. S. Woo, Z. Osváth, L. P. Biró, and S. Roth, 'Electron transport in Ar+-irradiated single wall carbon nanotubes', *Phys Status Solidi B Basic Res*, vol. 243, no. 13, pp. 3346–3350, 2006, doi: 10.1002/pssb.200669183.

[25] A. Jorio *et al.*, 'Characterizing carbon nanotube samples with resonance Raman scattering', *New J Phys*, vol. 5, no. 1, pp. 139–139, Oct. 2003, doi: 10.1088/1367-2630/5/1/139.

[26] A. C. Ferrari and D. M. Basko, 'Raman spectroscopy as a versatile tool for studying the properties of graphene', pp. 1–26, 2013, doi: 10.1038/nnano.2013.46.

[27] J. Zhang *et al.*, 'Effect of chemical oxidation on the structure of single-walled carbon nanotubes', *Journal of Physical Chemistry B*, vol. 107, no. 16, pp. 3712–3718, 2003, doi: 10.1021/jp027500u.

[28] S. Maruyama *et al.*, 'Optical characterization of single-walled carbon nanotubes synthesized by catalytic decomposition of alcohol', *New J Phys*, vol. 2630, no. 03, pp. 1–12, 2003.

[29] a. Hagen and T. Hertel, 'Quantitative Analysis of Optical Spectra from Individual Single-Wall Carbon Nanotubes', *Nano Lett*, vol. 3, no. 3, pp. 383–388, 2003, doi: 10.1021/nl020237o.

[30] X. Wei, T. Tanaka, Y. Yomogida, N. Sato, R. Saito, and H. Kataura, 'Experimental determination of excitonic band structures of single-walled carbon nanotubes using circular dichroism spectra', *Nat Commun*, vol. 7, 2016, doi: 10.1038/ncomms12899.

[31] M. J. O'Connell, 'Band Gap Fluorescence from Individual Single-Walled Carbon Nanotubes', *Science (1979)*, vol. 297, no. 5581, pp. 593–596, 2002, doi: 10.1126/science.1072631.

[32] Y. Miyauchi and S. Maruyama, 'Identification of an excitonic phonon sideband by photoluminescence spectroscopy of single-walled carbon-13 nanotubes', *Phys Rev B Condens Matter Mater Phys*, vol. 74, no. 3, p. 035415, Jul. 2006, doi: 10.1103/PhysRevB.74.035415.

[33] F. Plentz, H. B. Ribeiro, A. Jorio, M. S. Strano, and M. A. Pimenta, 'Direct experimental evidence of exciton-phonon bound states in carbon nanotubes', *Phys Rev Lett*, vol. 95, no. 24, 2005, doi: 10.1103/PhysRevLett.95.247401.

[34] H. Htoon, M. J. O'Connell, S. K. Doom, and V. I. Klimov, 'Single carbon nanotubes probed by photoluminescence excitation spectroscopy: The role of phonon-assisted transitions', *Phys Rev Lett*, vol. 94, no. 12, pp. 1–4, Apr. 2005, doi: 10.1103/PhysRevLett.94.127403.

[35] M. F. Islam, D. E. Milkie, C. L. Kane, A. G. Yodh, and J. M. Kikkawa, 'Direct measurement of the polarized optical absorption cross section of single-wall carbon nanotubes', *Phys Rev Lett*, vol. 93, no. 3, pp. 3–6, Jul. 2004, doi: 10.1103/PhysRevLett.93.037404.

[36] Y. Murakami, E. Einarsson, T. Edamura, and S. Maruyama, 'Polarization dependence of the optical absorption of single-walled carbon nanotubes',

Phys Rev Lett, vol. 94, no. 8, p. 087402, Mar. 2005, doi: 10.1103/PhysRevLett.94.087402.

[37] L. Oudjedi, A. N. G. Parra-Vasquez, A. G. Godin, L. Cognet, and B. Lounis, 'Metrological investigation of the (6,5) carbon nanotube absorption cross section', *Journal of Physical Chemistry Letters*, vol. 4, no. 9, pp. 1460–1464, 2013, doi: 10.1021/jz4003372.

[38] D. Joh, J. Kinder, L. Herman, and S. Ju, 'Supporting Information for Single-walled carbon nanotubes as excitonic optical wires', *Nat Nanotechnol*, vol. 6, no. 1, pp. 51–56, 2010, Accessed: Dec. 08, 2017. [Online]. Available: https://www.nature.com/nnano/journal/v6/n1/abs/nnano.2010.248.html

[39] F. Schöppler *et al.*, 'Molar extinction coefficient of single-wall carbon nanotubes', *Journal of Physical Chemistry C*, vol. 115, no. 30, pp. 14682–14686, 2011, doi: 10.1021/jp205289h.

[40] T. Koyama, Y. Miyata, H. Kishida, H. Shinohara, and A. Nakamura, 'Photophysics in single-walled carbon nanotubes with (6,4) chirality at high excitation densities: Bimolecular auger recombination and phase-space filling of excitons', *Journal of Physical Chemistry C*, vol. 117, no. 4, pp. 1974–1981, Jan. 2013, doi: 10.1021/jp312798h.

[41] S. Berciaud, L. Cognet, and B. Lounis, 'Luminescence decay and the absorption cross section of individual single-walled carbon nanotubes', *Phys Rev Lett*, vol. 101, no. 7, 2008, doi: 10.1103/PhysRevLett.101.077402.

[42] Y. Homma, S. Chiashi, and Y. Kobayashi, 'Suspended single-wall carbon nanotubes: Synthesis and optical properties', *Reports on Progress in Physics*, vol. 72, no. 6, p. 066502, Jun. 2009, doi: 10.1088/0034-4885/72/6/066502.

[43] Y. Murakami, B. Lu, S. Kazaoui, N. Minami, T. Okubo, and S. Maruyama, 'Photoluminescence sidebands of carbon nanotubes below the bright singlet excitonic levels', *Phys Rev B Condens Matter Mater Phys*, vol. 79, no. 19, 2009, doi: 10.1103/PhysRevB.79.195407.

[44] Y. Kadria-Vili, S. M. Bachilo, J. L. Blackburn, and R. B. Weisman, 'Photoluminescence Side Band Spectroscopy of Individual Single-Walled Carbon Nanotubes', *Journal of Physical Chemistry C*, vol. 120, no. 41, pp. 23898–23904, 2016, doi: 10.1021/acs.jpcc.6b08768.

[45] V. Perebeinos, J. Tersoff, and P. Avouris, 'Electron-Phonon Interaction and Transport in Semiconducting Carbon Nanotubes', *Phys Rev Lett*, vol. 94, no. 8, p. 086802, Mar. 2005, doi: 10.1103/PhysRevLett.94.086802.

[46] C. Fantini, A. Jorio, M. Souza, M. S. Strano, M. S. Dresselhaus, and M. A. Pimenta, 'Optical transition energies for carbon nanotubes from resonant

raman spectroscopy: Environment and temperature effects', *Phys Rev Lett*, vol. 93, no. 14, pp. 1–4, Sep. 2004, doi: 10.1103/PhysRevLett.93.147406.

[47] Y. Ohno, S. Iwasaki, Y. Murakami, S. Kishimoto, S. Maruyama, and T. Mizutani, 'Chirality-dependent environmental effects in photoluminescence of single-walled carbon nanotubes', *Phys Rev B Condens Matter Mater Phys*, vol. 73, no. 23, p. 235427, Jun. 2006, doi: 10.1103/PhysRevB.73.235427.

[48] J. Lefebvre, J. M. Fraser, Y. Homma, and P. Finnie, 'Photoluminescence from single-walled carbon nanotubes: A comparison between suspended and micelle-encapsulated nanotubes', *Appl Phys A Mater Sci Process*, vol. 78, no. 8, pp. 1107–1110, 2004, doi: 10.1007/s00339-003-2460-6.

[49] J. G. Duque, M. Pasquali, L. Cognet, and B. Lounis, 'Environmental and synthesis-dependent luminescence properties of individual single-walled carbon nanotubes', *ACS Nano*, vol. 3, no. 8, pp. 2153–2156, Aug. 2009, doi: 10.1021/nn9003956.

[50] S. Chiashi, S. Watanabe, T. Hanashima, and Y. Homma, 'Influence of gas adsorption on optical transition energies of single-walled carbon nanotubes', *Nano Lett*, vol. 8, no. 10, pp. 3097–3101, Oct. 2008, doi: 10.1021/nl801074j.

[51] Y. Miyauchi *et al.*, 'Dependence of exciton transition energy of single-walled carbon nanotubes on surrounding dielectric materials', *Chem Phys Lett*, vol. 442, no. 4–6, pp. 394–399, 2007, doi: 10.1016/j.cplett.2007.06.018.

[52] R. Matsunaga, K. Matsuda, and Y. Kanemitsu, 'Evidence for dark excitons in a single carbon nanotube due to the Aharonov-Bohm effect', *Phys Rev Lett*, vol. 101, no. 14, 2008, doi: 10.1103/PhysRevLett.101.147404.

[53] Y. Z. Ma, L. Valkunas, S. L. Dexheimer, and G. R. Fleming, 'Ultrafast exciton dynamics in semiconducting single-walled carbon nanotubes', *Mol Phys*, vol. 104, no. 8, pp. 1179–1189, 2006, doi: 10.1080/00268970500525564.

[54] J. S. Lauret *et al.*, 'Ultrafast Carrier Dynamics in Single-Wall Carbon Nanotubes', *Phys Rev Lett*, vol. 90, no. 5, p. 4, 2003, doi: 10.1103/PhysRevLett.90.057404.

[55] Y. Z. Ma *et al.*, 'Ultrafast carrier dynamics in single-walled carbon nanotubes probed by femtosecond spectroscopy', *Journal of Chemical Physics*, vol. 120, no. 7, pp. 3368–3373, 2004, doi: 10.1063/1.1640339.

[56] C. Manzoni, A. Gambetta, E. Menna, M. Meneghetti, G. Lanzani, and G. Cerullo, 'Intersubband exciton relaxation dynamics in single-walled carbon nanotubes', *Phys Rev Lett*, vol. 94, no. 20, pp. 2–5, 2005, doi: 10.1103/PhysRevLett.94.207401.

[57] Z. Zhu *et al.*, 'Pump-probe spectroscopy of exciton dynamics in (6,5) carbon nanotubes', *Journal of Physical Chemistry C*, vol. 111, no. 10, pp. 3831–3835, 2007, doi: 10.1021/jp0669411.

[58] K. Matsuda, T. Inoue, Y. Murakami, S. Maruyama, and Y. Kanemitsu, 'Exciton dephasing and multiexciton recombinations in a single carbon nanotube', *Phys Rev B Condens Matter Mater Phys*, vol. 77, no. 3, 2008, doi: 10.1103/PhysRevB.77.033406.

[59] F. Wang, G. Dukovic, L. E. Brus, and T. F. Heinz, 'Time-resolved fluorescence of carbon nanotubes and its implication for radiative lifetimes', *Phys Rev Lett*, vol. 92, no. 17, pp. 177401–1, 2004, doi: 10.1103/PhysRevLett.92.177401.

[60] C. D. Spataru, S. Ismail-Beigi, R. B. Capaz, and S. G. Louie, 'Theory and Ab initio calculation of radiative lifetime of excitons in semiconducting carbon nanotubes', *Phys Rev Lett*, vol. 95, no. 24, pp. 1–4, 2005, doi: 10.1103/PhysRevLett.95.247402.

[61] V. Perebeinos, J. Tersoff, P. A.-N. Letters, undefined 2005, and P. Avouris, 'Radiative lifetime of excitons in carbon nanotubes', *Nano Lett*, vol. 5, no. 12, pp. 2495–2499, 2005, doi: 10.1021/nl051828s.

[62] G. N. Ostojic *et al.*, 'Interband Recombination Dynamics in Resonantly Excited Single-Walled Carbon Nanotubes', *Phys Rev Lett*, vol. 92, no. 11, pp. 117402–1, 2004, doi: 10.1103/PhysRevLett.92.117402.

[63] S. Reich, M. Dworzak, A. Hoffmann, C. Thomsen, and M. S. Strano, 'Excited-state carrier lifetime in single-walled carbon nanotubes', *Phys Rev B Condens Matter Mater Phys*, vol. 71, no. 3, pp. 1–4, 2005, doi: 10.1103/PhysRevB.71.033402.

[64] O. J. Korovyanko, C. X. Sheng, Z. V. Vardeny, A. B. Dalton, and R. H. Baughman, 'Ultrafast Spectroscopy of Excitons in Single-Walled Carbon Nanotubes', *Phys Rev Lett*, vol. 92, no. 1, p. 4, 2004, doi: 10.1103/PhysRevLett.92.017403.

[65] M. Jones *et al.*, 'Analysis of photoluminescence from solubilized single-walled carbon nanotubes', *Phys Rev B Condens Matter Mater Phys*, vol. 71, no. 11, 2005, doi: 10.1103/PhysRevB.71.115426.

[66] T. Hertel, S. Himmelein, T. Ackermann, D. Stich, and J. Crochet, 'Diffusion limited photoluminescence quantum yields in 1-D semiconductors: Single-wall carbon nanotubes', *ACS Nano*, vol. 4, no. 12, pp. 7161–7168, 2010, doi: 10.1021/nn101612b.

[67] T. Gokus, L. Cognet, J. G. Duque, M. Pasquali, A. Hartschuh, and B. Lounis, 'Mono-and biexponential luminescence decays of individual single-walled

carbon nanotubes', *Journal of Physical Chemistry C*, vol. 114, no. 33, pp. 14025–14028, 2010, doi: 10.1021/jp1049217.

[68] A. Hagen *et al.*, 'Exponential decay lifetimes of excitons in individual single-walled carbon nanotubes', *Phys Rev Lett*, vol. 95, no. 19, pp. 1–4, 2005, doi: 10.1103/PhysRevLett.95.197401.

[69] L. Huang, H. N. Pedrosa, and T. D. Krauss, 'Ultrafast ground-state recovery of single-walled carbon nanotubes', *Phys Rev Lett*, vol. 93, no. 1, pp. 1–4, 2004, doi: 10.1103/PhysRevLett.93.017403.

[70] J. Lefebvre, D. G. Austing, J. Bond, and P. Finnie, 'Photoluminescence imaging of suspended single-walled carbon nanotubes', *Nano Lett*, vol. 6, no. 8, pp. 1603–1608, 2006, doi: 10.1021/nl060530e.

[71] L. J. Carlson, S. E. Maccagnano, M. Zheng, J. Silcox, and T. D. Krauss, 'Fluorescence efficiency of individual carbon nanotubes', *Nano Lett*, vol. 7, no. 12, pp. 3698–3703, 2007, doi: 10.1021/nl072014+.

[72] D. A. Tsyboulski, J. D. R. Rocha, S. M. Bachilo, L. Cognet, and R. B. Weisman, 'Structure-dependent fluorescence efficiencies of individual single-walled carbon nanotubes', *Nano Lett*, vol. 7, no. 10, pp. 3080–3085, Oct. 2007, doi: 10.1021/nl071561s.

[73] Y. Z. Ma, C. D. Spataru, L. Valkunas, S. G. Louie, and G. R. Fleming, 'Spectroscopy of zigzag single-walled carbon nanotubes: Comparing femtosecond transient absorption spectra with ab initio calculations', *Phys Rev B Condens Matter Mater Phys*, vol. 74, no. 8, pp. 1–9, 2006, doi: 10.1103/PhysRevB.74.085402.

[74] A. R. Amori, Z. Hou, and T. D. Krauss, 'Excitons in Single-Walled Carbon Nanotubes and Their Dynamics', *Annu Rev Phys Chem*, vol. 69, pp. 81–99, 2018, doi: 10.1146/annurev-physchem-050317-014241.

[75] Y. Z. Ma, T. Hertel, Z. V. Vardeny, G. R. Fleming, and L. Valkunas, 'Ultrafast spectroscopy of carbon nanotubes', *Topics in Applied Physics*, vol. 111, pp. 321–352, 2008, doi: 10.1007/978-3-540-72865-8_10.

[76] V. Perebeinos, J. Tersoff, and P. Avouris, 'Scaling of excitons in carbon nanotubes', *Phys Rev Lett*, vol. 92, no. 25 I, pp. 8–11, 2004, doi: 10.1103/PhysRevLett.92.257402.

[77] J. Maultzsch *et al.*, 'Excitons in carbon nanotubes', *Phys Status Solidi B Basic Res*, vol. 243, no. 13, pp. 3204–3208, 2006, doi: 10.1002/pssb.200669131.

[78] F. Wang, G. Dukovic, E. Knoesel, L. E. Brus, and T. F. Heinz, 'Observation of rapid Auger recombination in optically excited semiconducting carbon

nanotubes', *Phys Rev B Condens Matter Mater Phys*, vol. 70, no. 24, pp. 1–4, 2004, doi: 10.1103/PhysRevB.70.241403.

[79] B. Yuma *et al.*, 'Biexciton, single carrier, and trion generation dynamics in single-walled carbon nanotubes', *Phys Rev B Condens Matter Mater Phys*, vol. 87, no. 20, pp. 1–7, 2013, doi: 10.1103/PhysRevB.87.205412.

[80] J. Park, P. Deria, and M. J. Therien, 'Dynamics and transient absorption spectral signatures of the single-wall carbon nanotube electronically excited triplet state', *J Am Chem Soc*, vol. 133, no. 43, pp. 17156–17159, 2011, doi: 10.1021/ja2079477.

[81] S. Settele *et al.*, 'Synthetic control over the binding configuration of luminescent sp3-defects in single-walled carbon nanotubes', *Nat Commun*, no. 2021, pp. 1–10, 2021, doi: 10.1038/s41467-021-22307-9.

[82] B. J. Gifford, S. Kilina, H. Htoon, S. K. Doorn, and S. Tretiak, 'Controlling defect-state photophysics in covalently functionalized single-walled carbon nanotubes', *Acc Chem Res*, vol. 53, no. 9, pp. 1791–1801, 2020, doi: 10.1021/acs.accounts.0c00210.

[83] T. Shiraki, Y. Miyauchi, K. Matsuda, and N. Nakashima, 'Carbon nanotube photoluminescence modulation by local chemical and supramolecular chemical functionalization', *Acc Chem Res*, vol. 53, no. 9, pp. 1846–1859, 2020, doi: 10.1021/acs.accounts.0c00294.

[84] X. He *et al.*, 'Intrinsic limits of defect-state photoluminescence dynamics in functionalized carbon nanotubes', *Nanoscale*, vol. 11, no. 18, pp. 9125–9132, 2019, doi: 10.1039/c9nr02175b.

[85] Y. Kim *et al.*, 'Photoluminescence Intensity Fluctuations and Temperature-Dependent Decay Dynamics of Individual Carbon Nanotube sp ^{3} Defects', *J Phys Chem Lett*, vol. 10, no. 6, pp. 1423–1430, Mar. 2019, doi: 10.1021/acs.jpclett.8b03732.

[86] B. J. Gifford *et al.*, 'Optical Effects of Divalent Functionalization of Carbon Nanotubes', *Chemistry of Materials*, vol. 31, no. 17, pp. 6950–6961, 2019, doi: 10.1021/acs.chemmater.9b01438.

[87] M. E. Sykes *et al.*, 'Ultrafast Exciton Trapping at sp3 Quantum Defects in Carbon Nanotubes', *ACS Nano*, vol. 13, no. 11, pp. 13264–13270, 2019, doi: 10.1021/acsnano.9b06279.

[88] M. Nutz *et al.*, 'Photon Correlation Spectroscopy of Luminescent Quantum Defects in Carbon Nanotubes', *Nano Lett*, vol. 19, no. 10, pp. 7078–7084, 2019, doi: 10.1021/acs.nanolett.9b02553.

[89] Y. Piao *et al.*, 'Brightening of carbon nanotube photoluminescence through the incorporation of sp 3 defects', *Nat Chem*, vol. 5, no. 10, pp. 840–845, 2013, doi: 10.1038/nchem.1711.

[90] X. Ma *et al.*, 'Electronic Structure and Chemical Nature of Oxygen Dopant States in Carbon Nanotubes', *Nat Nanotechnol*, vol. 7, no. July, pp. 1–6, 2015, doi: 10.1038/nnano.2011.227.

[91] B. O. Tayo and S. V. Rotkin, 'Charge impurity as a localization center for singlet excitons in single-wall nanotubes', *Phys Rev B Condens Matter Mater Phys*, vol. 86, no. 12, pp. 1–8, 2012, doi: 10.1103/PhysRevB.86.125431.

[92] K. H. Eckstein, H. Hartleb, M. M. Achsnich, F. Schöppler, and T. Hertel, 'Localized Charges Control Exciton Energetics and Energy Dissipation in Doped Carbon Nanotubes', *ACS Nano*, vol. 11, no. 10, pp. 10401–10408, 2017, doi: 10.1021/acsnano.7b05543.

[93] S. Mouri, Y. Miyauchi, M. Iwamura, and K. Matsuda, 'Temperature dependence of photoluminescence spectra in hole-doped single-walled carbon nanotubes: Implications of trion localization', *Phys Rev B Condens Matter Mater Phys*, vol. 87, no. 4, pp. 1–4, 2013, doi: 10.1103/PhysRevB.87.045408.

[94] T. F. Rønnow, T. G. Pedersen, and H. D. Cornean, 'Correlation and dimensional effects of trions in carbon nanotubes', *Phys Rev B Condens Matter Mater Phys*, vol. 81, no. 20, pp. 1–7, 2010, doi: 10.1103/PhysRevB.81.205446.

[95] R. Matsunaga, K. Matsuda, and Y. Kanemitsu, 'Observation of charged excitons in hole-doped carbon nanotubes using photoluminescence and absorption spectroscopy', *Phys Rev Lett*, vol. 106, no. 3, pp. 1–4, 2011, doi: 10.1103/PhysRevLett.106.037404.

[96] S. M. Santos *et al.*, 'All-optical trion generation in single-walled carbon nanotubes', *Phys Rev Lett*, vol. 107, no. 18, p. 187401, 2011, doi: 10.1103/PhysRevLett.107.187401.

[97] T. Koyama, S. Shimizu, Y. Miyata, H. Shinohara, and A. Nakamura, 'Ultrafast formation and decay dynamics of trions in p-doped single-walled carbon nanotubes', *Phys Rev B Condens Matter Mater Phys*, vol. 87, no. 16, p. 165430, 2013, doi: 10.1103/PhysRevB.87.165430.

[98] T. Nishihara, Y. Yamada, M. Okano, and Y. Kanemitsu, 'Trion formation and recombination dynamics in hole-doped single-walled carbon nanotubes', *Appl Phys Lett*, vol. 103, no. 2, p. 023101, 2013, doi: 10.1063/1.4813014.

[99] H. Hartleb, F. Spath, and T. Hertel, 'Evidence for Strong Electronic Correlations in the Spectra of Gate-Doped Single-Wall Carbon Nanotubes', *ACS Nano*, vol. 9, no. 10, pp. 10461–10470, 2015, doi: 10.1103/PhysRevB.75.035122.

[100] N. Akizuki, S. Aota, S. Mouri, K. Matsuda, and Y. Miyauchi, 'Efficient near-infrared up-conversion photoluminescence in carbon nanotubes', *Nat Commun*, vol. 6, pp. 1–6, 2015, doi: 10.1038/ncomms9920.

[101] H. Harutyunyan, T. Gokus, A. A. Green, M. C. Hersam, M. Allegrini, and A. Hartschuh, 'Photoluminescence from disorder induced states in individual single-walled carbon nanotubes', *Phys Status Solidi B Basic Res*, vol. 246, no. 11–12, pp. 2679–2682, 2009, doi: 10.1002/pssb.200982273.

[102] M. Iwamura *et al.*, 'Nonlinear Photoluminescence Spectroscopy of Carbon Nanotubes with Localized Exciton States', *ACS Nano*, vol. 8, no. 11, pp. 11254–11260, 2014, doi: 10.1021/nn503803b.

[103] X. He *et al.*, 'Tunable room-Temperature single-photon emission at telecom wavelengths from sp 3 defects in carbon nanotubes', *Nat Photonics*, vol. 11, no. 9, pp. 577–582, 2017, doi: 10.1038/nphoton.2017.119.

[104] S. Ghosh, S. M. Bachilo, R. A. Simonette, K. M. Beckingham, and R. B. Weisman, 'Oxygen doping modifies near-infrared band gaps in fluorescent single-walled carbon nanotubes', *Science (1979)*, vol. 330, no. 6011, pp. 1656–1659, 2010, doi: 10.1126/science.1196382.

[105] H. Kwon *et al.*, 'Molecularly Tunable Fluorescent Quantum Defects', *J Am Chem Soc*, vol. 138, no. 21, pp. 6878–6885, 2016, doi: 10.1021/jacs.6b03618.

[106] A. H. Brozena, M. Kim, L. R. Powell, and Y. H. Wang, 'Controlling the optical properties of carbon nanotubes with organic colour-centre quantum defects', *Nat Rev Chem*, vol. 3, no. 6, pp. 375–392, 2019, doi: 10.1038/s41570-019-0103-5.

[107] W. Zheng, N. F. Zorn, M. Bonn, J. Zaumseil, and H. I. Wang, 'Probing Carrier Dynamics in sp3-Functionalized Single-Walled Carbon Nanotubes with Time-Resolved Terahertz Spectroscopy', *ACS Nano*, vol. 16, no. 6, pp. 9401–9409, 2022, doi: 10.1021/acsnano.2c02199.

[108] N. F. Hartmann *et al.*, 'Photoluminescence Dynamics of Aryl sp3 Defect States in Single-Walled Carbon Nanotubes', *ACS Nano*, vol. 10, no. 9, pp. 8355–8365, 2016, doi: 10.1021/acsnano.6b02986.

[109] X. He *et al.*, 'Solvent- and Wavelength-Dependent Photoluminescence Relaxation Dynamics of Carbon Nanotube sp ^{3} Defect States', *ACS Nano*, no. July, p. acsnano.8b02909, 2018, doi: 10.1021/acsnano.8b02909.

[110] Y. Miyauchi, M. Iwamura, S. Mouri, T. Kawazoe, M. Ohtsu, and K. Matsuda, 'Brightening of excitons in carbon nanotubes on dimensionality modification', *Nat Photonics*, vol. 7, no. 9, pp. 715–719, 2013, doi: 10.1038/nphoton.2013.179.

[111] A. K. Ekert, 'Quantum Cryptography and Bell's Theorem', pp. 413–418, 1992, doi: 10.1007/978-1-4615-3386-3_34.

[112] A. Beveratos, R. Brouri, T. Gacoin, A. Villing, J. P. Poizat, and P. Grangier, 'Single Photon Quantum Cryptography', *Phys Rev Lett*, vol. 89, no. 18, pp. 4–7, 2002, doi: 10.1103/PhysRevLett.89.187901.

[113] T. Marshall and S. Santos, 'Comment on "experimental evidence for a photon anticorrelation effect on a beam splitter: A new light on single-photon interferences"', *Epl*, vol. 3, no. 3, pp. 293–296, 1987, doi: 10.1209/0295-5075/3/3/007.

[114] I. Aharonovich, D. Englund, and M. Toth, 'Solid-state single-photon emitters', *Nat Photonics*, vol. 10, no. 10, pp. 631–641, 2016, doi: 10.1038/nphoton.2016.186.

[115] Y. Lin, Y. Ye, and W. Fang, 'Electrically driven single-photon sources', *Journal of Semiconductors*, vol. 40, no. 7, 2019, doi: 10.1088/1674-4926/40/7/071904.

[116] S. M. Bachilo, 'Structure-Assigned Optical Spectra of Single-Walled Carbon Nanotubes', *Science (1979)*, vol. 298, no. 5602, pp. 2361–2366, 2002, doi: 10.1126/science.1078727.

[117] J. A. Misewich, R. Martel, J. C. Tsang, S. Heinze, and J. Tersoff, 'Electrically Induced Optical Emission from a Carbon Nanotube FET', vol. 300, no. May, pp. 783–786, 2003.

[118] A. Högele, C. Galland, M. Winger, and A. Imamoğlu, 'Photon antibunching in the photoluminescence spectra of a single carbon nanotube', *Phys Rev Lett*, vol. 100, no. 21, pp. 5–8, 2008, doi: 10.1103/PhysRevLett.100.217401.

[119] X. Ma, N. F. Hartmann, J. K. S. Baldwin, S. K. Doorn, and H. Htoon, 'Room-temperature single-photon generation from solitary dopants of carbon nanotubes', *Nat Nanotechnol*, vol. 10, no. 8, pp. 671–675, Aug. 2015, doi: 10.1038/nnano.2015.136.

[120] S. Khasminskaya *et al.*, 'Fully integrated quantum photonic circuit with an electrically driven light source', *Nat Photonics*, vol. 10, no. 11, pp. 727–732, 2016, doi: 10.1038/nphoton.2016.178.

[121] A. Ishii *et al.*, 'Enhanced Single-Photon Emission from Carbon-Nanotube Dopant States Coupled to Silicon Microcavities', *Nano Lett*, 2018, doi: 10.1021/acs.nanolett.8b01170.

[122] Y. Luo *et al.*, 'Carbon nanotube color centers in plasmonic nanocavities: A path to photon indistinguishability at telecom bands', *Nano Lett*, pp. 9037–9044, 2019, doi: 10.1021/acs.nanolett.9b04069.

[123] Y. Zheng *et al.*, 'Quantum Light Emission from Coupled Defect States in DNA-Functionalized Carbon Nanotubes', *ACS Nano*, vol. 15, no. 6, pp. 10406–10414, 2021, doi: 10.1021/acsnano.1c02709.

[124] R. Kawabe, H. Takaki, T. Ibi, Y. Maeda, K. Nakagawa, and H. Maki, 'Pure and Efficient Single-Photon Sources by Shortening and Functionalizing Air-Suspended Carbon Nanotubes', *ACS Appl Nano Mater*, vol. 3, no. 1, pp. 682–690, 2020, doi: 10.1021/acsanm.9b02209.

[125] C. W. Lin *et al.*, 'Creating fluorescent quantum defects in carbon nanotubes using hypochlorite and light', *Nat Commun*, vol. 10, no. 1, 2019, doi: 10.1038/s41467-019-10917-3.

[126] R. B. Weisman and S. M. Bachilo, 'Dependence of optical transition energies on structure for single-walled carbon nanotubes in aqueous suspension: An empirical Kataura plot', *Nano Lett*, vol. 3, no. 9, pp. 1235–1238, 2003, doi: 10.1021/nl034428i.

[127] G. Pagani, M. J. Green, P. Poulin, and M. Pasquali, 'Competing mechanisms and scaling laws for carbon nanotube scission by ultrasonication', vol. 109, no. 29, 2012, doi: 10.1073/pnas.1200013109.

[128] M. Yoshida, A. Popert, and Y. K. Kato, 'Gate-voltage induced trions in suspended carbon nanotubes', *Phys Rev B Condens Matter Mater Phys*, vol. 93, no. 4, pp. 1–5, 2016, doi: 10.1103/PhysRevB.93.041402.

[129] J. S. Park, Y. Hirana, S. Mouri, Y. Miyauchi, N. Nakashima, and K. Matsuda, 'Observation of negative and positive trions in the electrochemically carrier-doped single-walled carbon nanotubes', *J Am Chem Soc*, vol. 134, no. 35, pp. 14461–14466, 2012, doi: 10.1021/ja304282j.

[130] M. S. Strano *et al.*, 'Reversible, band-gap-selective protonation of single-walled carbon nanotubes in solution', *Journal of Physical Chemistry B*, vol. 107, no. 29, pp. 6979–6985, 2003, doi: 10.1021/jp027664a.

[131] A. Dowgiallo, K. S. Mistry, J. C. Johnson, and J. L. Blackburn, 'Ultrafast Spectroscopic Signature of Charge Transfer between Single- Walled Carbon Nanotubes and C 60', *ACS Nano*, vol. 8, no. 8, pp. 8573–8581, 2014, doi: 10.1021/nn503271k.

[132] P. Finnie and J. Lefebvre, 'Photoinduced band gap shift and deep levels in luminescent carbon nanotubes', *ACS Nano*, vol. 6, no. 2, pp. 1702–1714, 2012, doi: 10.1021/nn204679s.

[133] C. F. Chiu, W. A. Saidi, V. E. Kagan, and A. Star, 'Defect-Induced Near-Infrared Photoluminescence of Single-Walled Carbon Nanotubes Treated with Polyunsaturated Fatty Acids', *J Am Chem Soc*, vol. 139, no. 13, pp. 4859–4865, 2017, doi: 10.1021/jacs.7b00390.

[134] T. Shiraishi, T. Shiraki, and N. Nakashima, 'Substituent effects on the redox states of locally functionalized single-walled carbon nanotubes revealed by in situ photoluminescence spectroelectrochemistry', *Nanoscale*, vol. 9, no. 43, pp. 16900–16907, 2017, doi: 10.1039/C7NR05480G.

[135] Y. Bai *et al.*, 'Dynamics of charged excitons in electronically and morphologically homogeneous single-walled carbon nanotubes', *Proceedings of the National Academy of Sciences*, vol. 115, no. 1, pp. 674–679, 2018, doi: 10.1073/pnas.1712971115.

[136] Y. Z. Ma, L. Valkunas, S. L. Dexheimer, S. M. Bachilo, and G. R. Fleming, 'Femtosecond spectroscopy of optical excitations in single-walled carbon nanotubes: Evidence for exciton-exciton annihilation', *Phys Rev Lett*, vol. 94, no. 15, pp. 1–4, 2005, doi: 10.1103/PhysRevLett.94.157402.

[137] R. Loudon and R. Loudon, 'One-dimensional hydrogen 2016', 2016.

[138] R. Loudon, 'One-Dimensional Hydrogen Atom 1959', *Am J Phys*, vol. 27, no. 9, pp. 649–655, 1959, doi: 10.1119/1.1934950.

[139] Y. Ran, L. Xue, S. Hu, and R. Su, 'On the Coulomb-type potential of the one-dimensional Schrödinger equation', vol. 9265, 2000.

[140] A. H. Brozena, J. D. Leeds, Y. Zhang, J. T. Fourkas, and Y. Wang, 'Controlled defects in semiconducting carbon nanotubes promote efficient generation and luminescence of trions', *ACS Nano*, vol. 8, no. 5, pp. 4239–4247, 2014, doi: 10.1021/nn500894p.

[141] T. Deilmann, M. Drüppel, and M. Rohlfing, 'Three-particle correlation from a Many-Body Perspective: Trions in a Carbon Nanotube', *Phys Rev Lett*, vol. 116, no. 19, pp. 1–6, 2016, doi: 10.1103/PhysRevLett.116.196804.

[142] A. Saha *et al.*, 'Narrow-band single-photon emission through selective aryl functionalization of zigzag carbon nanotubes', *Nat Chem*, vol. 10, pp. 1089–1095, 2018, doi: 10.1038/s41557-018-0126-4.

[143] Y. Iizumi, M. Yudasaka, J. Kim, H. Sakakita, T. Takeuchi, and T. Okazaki, 'Oxygen-doped carbon nanotubes for near-infrared fluorescent labels and imaging probes', *Sci Rep*, vol. 8, no. 1, pp. 1–6, 2018, doi: 10.1038/s41598-018-24399-8.

[144] T. Shiraishi *et al.*, 'Determination of Precise Redox Properties of Oxygen-Doped Single-Walled Carbon Nanotubes Based on in Situ

Photoluminescence Electrochemistry', *Journal of Physical Chemistry C*, vol. 120, no. 29, pp. 15632–15639, 2016, doi: 10.1021/acs.jpcc.5b07841.

[145] T. Eremin and E. Obraztsova, 'Optical Properties of Single-Walled Carbon Nanotubes Doped in Acid Medium', *Phys Status Solidi B Basic Res*, vol. 255, no. 1, p. 1700272, 2017, doi: 10.1002/pssb.201700272.

[146] P. V. Fedotov *et al.*, 'Optical properties of single-walled carbon nanotubes filled with CuCl by gas-phase technique', *Phys Status Solidi B Basic Res*, vol. 251, no. 12, pp. 2466–2470, 2014, doi: 10.1002/pssb.201451240.

[147] M. Kalbac, L. Kavan, and L. Dunsch, 'Changes in the electronic states of single-walled carbon nanotubes as followed by a Raman spectroelectrochemical analysis of the radial breathing mode', *Journal of Physical Chemistry C*, vol. 112, no. 43, pp. 16759–16763, 2008, doi: 10.1021/jp805612d.

[148] F. L. Sebastian *et al.*, 'Absolute Quantification of sp 3 Defects in Semiconducting Single- Wall Carbon Nanotubes by Raman Spectroscopy', 2022, doi: 10.1021/acs.jpclett.2c00758.

[149] L. Lüer, G. Lanzani, J. Crochet, T. Hertel, J. Holt, and Z. V. Vardeny, 'Ultrafast dynamics in metallic and semiconducting carbon nanotubes', *Phys Rev B Condens Matter Mater Phys*, vol. 80, no. 20, pp. 4–8, 2009, doi: 10.1103/PhysRevB.80.205411.

[150] D. J. Styers-Barnett *et al.*, 'Exciton Dynamics and Biexciton Formation in Single-Walled Carbon Nanotubes Studied with Femtosecond Transient Absorption Spectroscopy', *The Journal of Physical Chemistry C*, vol. 112, no. 12, pp. 4507–4516, 2008, doi: 10.1021/jp7099256.

[151] D. K. Singh, P. K. Giri, and P. K. Iyer, 'Evidence for defect-enhanced photoluminescence quenching of fluorescein by carbon nanotubes', *Journal of Physical Chemistry C*, vol. 115, no. 49, pp. 24067–24072, 2011, doi: 10.1021/jp207392d.

Appendices

APPENDIX 1.

MATLAB script used to fit the decay curves according to the model described by formulas (12) and (13).

```
function [X, Y, xCuted, yFit, B, parametersNames] = getcut...
    (...                    %description of input arguments
    SampleName,...          %in format T1m5
    WhatToGet,...           %either "dyna" or "spec"
    ValueOfCut,...          %for example, 980 (nm) or 20 (ps)
    ifFit,...               %1 if fitting is needed, 0 if it is not needed
    zerotime, endtime,...   %difine interval in wich the differences will be fitted
    normalization,...       %1 if we normalize T*m0 and T*m* before subtractiong or not
    IFP,...                 %parameters of previous fitting. Probably unnessesary
    typeOfFittingFunction,...%define the function
    regime...
    )

if ~exist('endtime', 'var')
    endtime=0;
end
if ~exist('normalization', 'var')
    normalization=0;
end
if ~exist('IFP', 'var')
    IFP=0;
end
if ~exist('typeOfFittingFunction', 'var')
    typeOfFittingFunction="nope";
end
if ~exist('regime', 'var')
    regime="nope";
end


if exist('SampleName','var')
    %disp("Function getcut.m called externary")
    testing=0;
else
    clear all;
    close all;

    testing=1;
    %Initialization of arguments for testing
    disp("Warning, testiong is ON in getgut function");
    SampleName='T1m25';
    WhatToGet='dyna';
    ValueOfCut=980;
    %       WavelengthesVIS =[509 568 581 648 658 730]
    %       WavelengthesNIR =[875 910 980 1020 1130]
    ifFit=1;
    zerotime=0;
    endtime=5;
    normalization=0;
    IFP=0;

    typeOfFittingFunction="3exp+Y0";    %fitting of row pristine data
    regime="additionalChannel";         %function for additional channel is always diffP1exp+Y0  -
one exponent with diffucion

    %STOP PARAMETER INITIALIZING
end
plotFittingResults=0;

%% EXTRACTING
```

```
load('wsAllMaps');
map=eval(SampleName);

if (WhatToGet=='spec')
    X=map(:,1);
    name=transpose(map(1,:));
end
if (WhatToGet=='dyna')
    X=transpose(map(1,:));
    name=map(:,1);
end

IndexOfCut=GetIndexByValue(name, ValueOfCut);

if (WhatToGet=='spec')
    Y=map(:,IndexOfCut);
    Y(1)=[];% a Value of cut was there. I dont need it. I remove it for valid normalization
    X(1)=[];
    if testing==1
        plot(X,Y)
    end
end
if (WhatToGet=='dyna')
    Y=transpose(map(IndexOfCut,:));

    Y(1)=[];% a Value of cut was there. I dont need it. I remove it for valid normalization
    X(1)=[];
end


if WhatToGet=="dyna"
    if regime == "additionalChannel"
        %getting parameters of pristine dynamics
        %it is recursive call of the same function
        %so for each doping level each time I call the function to
        %calculate parapeters of fitting of pristine dynamics
        pSampleName=strcat(SampleName(1:3),"0");
        [Xp,Yp, xFitp, yFitp, IFP, parametersNames] = ...
            getcut(pSampleName, WhatToGet, ValueOfCut, 1, zerotime, endtime, normalization, 0,
typeOfFittingFunction, "simple");
    end

    if regime == "simple"
        [X,Y]=FindTrueZeroOfX(X,Y);
    end

    %% Normalization
    if (normalization==1)&&(WhatToGet=="dyna")
        M=max(abs(Y));
        Y=-Y/M;
    end

    %% FITTING
    if (ifFit==1)&&(WhatToGet=="dyna")
        %% extract only part of the dynamics for fitting
            indexzero = GetIndexByValue(X, zerotime);
            indexend = GetIndexByValue(X, endtime);

            xCuted  = X(indexzero:indexend);
            yCuted = Y(indexzero:indexend);

        [y,IFP,amountOfComponents,equationtext,parametersNames, LB,
UB]=generateFittingFunction(typeOfFittingFunction,IFP,regime);

        %% turning to positive values and normalize
            if max(yCuted)==max(abs(yCuted))
                S=1;
            else
                S=-1;
            end
            yCuted = S*yCuted/max(abs(yCuted));
```

```
        %% Fitting itself
        OLS = @(b) sum((y(b,xCuted) - yCuted).^2);           % Ordinary Least Squares cost function
        options = optimset(...
        'MaxIter', 5000000000,...
        'TolFun',0.000000000000001,...
        'MaxFunEvals', 5000000000 ...
                        );

        %'PlotFcns','optimplotx', ...
        B = fminsearchbnd(OLS, IFP, LB, UB, options);       % Use ‘fminsearch’ to minimise the ‘OLS’
function


        yFit = y(B,xCuted);                             % Calculate function with estimated
parameters
        sumofsq = sum((yFit - yCuted).^2);

        %% output results of fitting

        if (testing==1)||(plotFittingResults==1)
            %FfittingGetcut=figure; %create a new window for each fitting
            figure('Name', strcat("Fitting for ", SampleName, WhatToGet, num2str(ValueOfCut)));
            hold on;
            scatter(xCuted, yCuted, 'b');
            hold on
            plot(xCuted, yFit, '-r', 'LineWidth',1);
            title(strcat("Fitting in getcut.m  ", SampleName));
            xlabel("Delay, ps");
            ylabel("Normalized dA");
            text(0.3*max(xCuted),0.9*max(yCuted), equationtext);
            for p=1:length(parametersNames)
                text(0.5*max(xCuted),(0.9-0.05*p)*max(yCuted),
strcat(parametersNames(p),"=",num2str(B(p))));
            end
            FORORIGIN=[xCuted, yCuted,yFit];
            grid
        end

    else
        %preparing return if fitting was nad required
        xCuted=NaN;
        yFit=NaN;
        B=IFP; % if getcut was called without fitting B remains unchanged
        parametersNames="no parameters";
    end
else %that means WhatToGet = "dyna"
    %preparing return if spec was extracted
    xCuted=NaN;
    yFit=NaN;
    B=0; % if getcut was called without fitting B remains unchanged
    parametersNames="no parameters";
end
end
```

APPENDIX 2

MATLAB script used to calculate correction function according to formula (15)

```
function [delaytimes, CorrFun]=GetCorrFun(SampleType, pristUVtime, dopedUVtime, refWl, regime)


if exist('SampleType','var')
    %disp("Function GetDynamicsOfLocalizedExciton.m called externary")
    testing=0;
else
    clear all;
    close all;

    testing=1;
    disp("WARNING - testing in GetCorrFun");
    SampleType='T1';
    pristUVtime =0;
    dopedUVtime=25;
    refWl=[970 865];
    regime="noisy";
end
%STOP PARAMETER INITIALIZING

for i=(1:1:length(refWl))

    [delaytimesP, prist_ref_dyna, delaytimesP_cutted, prist_ref_dyna_fitted] =
getcut(strcat(SampleType,'m', num2str(pristUVtime)), 'dyna', refWl(i), 1, 0, 75, 0, 0 ,"3exp+Y0",
"simple");
    [delaytimesD, doped_ref_dyna, delaytimesD_cutted, doped_ref_dyna_fitted] =
getcut(strcat(SampleType,'m', num2str(dopedUVtime)), 'dyna', refWl(i), 1, 0, 75, 0, 0 ,"3exp+Y0",
"simple");

    [delaytimesP, prist_ref_dyna]=FindTrueZeroOfX(delaytimesP, prist_ref_dyna);
    [delaytimesD, doped_ref_dyna]=FindTrueZeroOfX(delaytimesD, doped_ref_dyna);

    [delaytimesP, prist_ref_dyna, delaytimesD, doped_ref_dyna]=tuneToSameXVAR(delaytimesP,
prist_ref_dyna, delaytimesD, doped_ref_dyna);

    delaytimes=delaytimesP;

    CorrFunArr = zeros(length(delaytimes),length(refWl));

    CorrFunArr(:,i)=doped_ref_dyna./prist_ref_dyna;  %this is the principal point
    f=min(prist_ref_dyna)/min(doped_ref_dyna);
    CorrFunArr(:,i)= CorrFunArr(:,i)*f;

    [~,z]=min(abs(delaytimes-0));
    CorrFunArr(1:z,i)=CorrFunArr(z,i);



    CorrFunArrSmooth = zeros(length(delaytimesP_cutted),length(refWl));
    CorrFunArrSmooth(:,i)=doped_ref_dyna_fitted./prist_ref_dyna_fitted;


    %OUTPUT
    if (testing==1)
        figure('Name', strcat('changes in dynamics',num2str(refWl(i))));
        plot(delaytimes, -prist_ref_dyna/min(prist_ref_dyna), 'DisplayName', "pristine ref dyna");
        hold on;
        plot(delaytimes, -doped_ref_dyna/min(doped_ref_dyna), 'DisplayName', "doped ref dyna");
        hold on;
        title(strcat('changes in dynamics',num2str(refWl(i))));
        legend;
        hold off;


        figure(2);
```

```
        plot(delaytimes, CorrFunArr(:,i), 'DisplayName', num2str(refWl(i))); %noisy
        hold on;
        plot(delaytimesP_cutted, CorrFunArrSmooth(:,i), 'DisplayName', num2str(refWl(i))); %smooth
        title('correction function calculated at refWL')

        legend;
        hold on;
    end

end

%VALUES TO RETURN
if regime=="smoothly"
    delaytimes=delaytimesP_cutted;
    CorrFun=mean(CorrFunArrSmooth, 2); %obtained by dividing fitting curves
end
if regime=="noisy"
    CorrFun=mean(CorrFunArr, 2);%obtained by dividing pristine data curves
end
```

APPENDIX 3

MATLAB script used to calculate correction function according to formulas (14) and (16).

```
function [X,Y] = GetDynamicsOfLocalizedExciton(SampleType, pristUVtime, dopedUVtime, locWl, refWl,
norm, CorrectionUsage, regime)
%Documentation
%Input
% string SampleType, T1 etc
% double pristUVtime, usually 0
% double dopedUVtime, 5, 10, 15 etc
% double  refWl, usually 980, may try 870 also
% double  locWL, we start at 1130, may be will calculate others
%       norm 1 or 0
%       CorrectionUsage 1 if use correction function and 0 if not use
%       correction function
%
%               Performance
% calculate correction function as dyndoped/dynpristine at 980
% modulate doped dynamics of badgeometry as pristine dynamics of doped geometry multiplied by
correction function
% estimate dynamics of loc exciton as measured dynamics at 1130 minus modulated dynamics of bad
geomatry
%norm option: if norm=1 then at t=0 modulated dynamics has the same
%intensity as measured
%
%
%               Output
% vector with dynamics of localized exciton
% testing output to workbook together wth delay times


if exist('SampleType','var')
    %disp("Function GetDynamicsOfLocalizedExciton.m called externary")
    testing=0;
else
    clear all;
    close all;

    testing=1;
    disp("WARNING - testing in GetDynamicsOfLocalizedExciton");
    SampleType='T1';
    pristUVtime =0;
    dopedUVtime=25;
    refWl=970;
    locWl=1115;
    norm=1;
    CorrectionUsage=1;
    %regime="smoothly";
    regime="noisy";
end

%STOP PARAMETER INITIALIZING

%NOTE: getcut(SampleName, WhatToGet, ValueOfCut, ifFit, zerotime)
[delaytimes, pristine_loc_dyna, fitedT, fitedP] = getcut(strcat(SampleType,'m',
num2str(pristUVtime)), 'dyna', locWl, 1, 0, 75, 0, 0 ,"3exp+Y0", "simple");
[delaytimes, measured_doped_loc_dyna, fitedT, fitedD] = getcut(strcat(SampleType,'m',
num2str(dopedUVtime)), 'dyna', locWl, 1, 0, 75, 0, 0 , "3exp+Y0", "simple");


if (CorrectionUsage==1)
    [delaytimesCorr, CorrFunS] = GetCorrFun(SampleType, pristUVtime, dopedUVtime, refWl,
'smoothly');
    LS=length(CorrFunS);
    [delaytimesCorr, CorrFunN] = GetCorrFun(SampleType, pristUVtime, dopedUVtime, refWl, 'noisy');
    LN=length(CorrFunN);
```

```
    CorrFun=CorrFunN;%adjusting length
    CorrFun(LN-LS+1:end)=CorrFunS;%fill positive part by smooth values
    CorrFun(1:LN-LS)=CorrFun(LN-LS+1);
else
    % an array of 1 with the same length
    delaytimesCorr=delaytimes;
    CorrFun=delaytimes;
    CorrFun(:)=1;
end


delaytimesP=delaytimes;
delaytimesM=delaytimes;

[delaytimesP, pristine_loc_dyna, delaytimesM, measured_doped_loc_dyna, delaytimesCorr,
CorrFun]=tuneToSameXVAR(delaytimesP, pristine_loc_dyna, delaytimesM, measured_doped_loc_dyna,
delaytimesCorr, CorrFun);
[delaytimesP, pristine_loc_dyna, delaytimesM, measured_doped_loc_dyna, delaytimesCorr,
CorrFun]=removeNaNRows(delaytimesP, pristine_loc_dyna, delaytimesM, measured_doped_loc_dyna,
delaytimesCorr, CorrFun);
delaytimes=delaytimesP;


if delaytimesP~=delaytimesM
    error('delaytimesP~=delaytimesM')
end



modulated_doped_loc_dyna=pristine_loc_dyna.*CorrFun; %modulated dynamics of bad SWNT
% normalization
if (norm==0)
    coef=1;
else
     index=GetIndexByValue(delaytimes, 0);
     coef=(abs(measured_doped_loc_dyna(index)))/(abs(modulated_doped_loc_dyna(index)));
end
modulated_doped_loc_dyna=coef*modulated_doped_loc_dyna;

% normalization finished
estimated_doped_loc_dyna=measured_doped_loc_dyna-modulated_doped_loc_dyna;

fitedP=fitedP*min(pristine_loc_dyna);
fitedD=fitedD*min(measured_doped_loc_dyna);


if (CorrectionUsage==1)
    [delaytimesCorr, CorrFunS] = GetCorrFun(SampleType, pristUVtime, dopedUVtime, refWl,
'smoothly');
else
    % an array of 1 with the same length
    delaytimesCorr=delaytimes;
    CorrFunS=fitedT;
    CorrFunS(:)=1;
end


modulated_fitedD=fitedP.*CorrFunS;
ind=GetIndexByValue(fitedT, 0);
modulated_fitedD=modulated_fitedD*(fitedD(ind)/modulated_fitedD(ind));
estimated_doped_loc_dyna_smooth=fitedD-modulated_fitedD;


%testing=0;
if (testing==1)
    figure(round(locWl));
    scatter(delaytimes, pristine_loc_dyna, 'r', 'DisplayName', strcat('Before doping
',num2str(locWl)));
    hold on;
    plot(fitedT, fitedP, 'r');
    hold on;
```

```
    scatter(delaytimes, measured_doped_loc_dyna, 'g','DisplayName',strcat('After doping measured
',num2str(locWl)));
    hold on;
    plot(fitedT, fitedD, 'g');
    hold on;

    scatter(delaytimes, modulated_doped_loc_dyna, 'b', 'DisplayName',strcat('After doping corrected
',num2str(locWl)));
    hold on;
    plot(fitedT, modulated_fitedD, 'b');
    hold on;



    plot(delaytimes, estimated_doped_loc_dyna, 'm', 'DisplayName',
strcat('estimated_doped_loc_dyna', num2str(locWl)));
    hold on;
    plot(fitedT, estimated_doped_loc_dyna_smooth, 'm', 'DisplayName',
strcat('stimated_doped_loc_dyna_smooth', num2str(locWl)));
    hold on;

    %xlim([0 25])


     title(strcat('Evaluation of dynamics of localized exciton dopedUVtime=',
num2str(dopedUVtime)));
     legend;
     hold off;

     output1=[delaytimes, pristine_loc_dyna, measured_doped_loc_dyna, modulated_doped_loc_dyna,
estimated_doped_loc_dyna];
     output2=[fitedT,fitedP,fitedD,modulated_fitedD,estimated_doped_loc_dyna_smooth];

end
%return

if regime=="smoothly"
    X = fitedT;
    Y = estimated_doped_loc_dyna_smooth;
end

if regime=="noisy"

    X = delaytimes;
    Y = estimated_doped_loc_dyna;
end


end
```

APPENDIX 4

MATLAB script used to plot TA map of E^*_{11} spectral feature.

```
function GetMapOfLocalizedExciton(SampleType, pristUVtime, dopedUVtime, refWl, norm,
CorrectionUsage, wl_left, wl_right, regime)
%briefly this usnction is the same as GetDynamicsOfLocalizedExciton but for
%all locWL

if exist('SampleType','var')
    disp("Function GetMapOfLocalizedExciton.m called externary")
    testing=0;
else
    clear all;
    close all;
    testing=1;

    disp("WARNING testing in GetMapOfLocalizedExciton")
    SampleType='T1';
    pristUVtime =0;
    dopedUVtime=25;
    refWl=970;
    norm=1;
    CorrectionUsage=1;
    wl_left=1100;
    wl_right=1170;
    time_start=-3;
    time_end=75;
    %regime="smoothly";
    regime="noisy";
end
%STOP PARAMETER INITIALIZING



%get the wavelength and timedalay vectors
[wl, ~] = getcut(strcat(SampleType,'m', num2str(pristUVtime)), 'spec', 10, 0, 0);
%amount_of_pixels=length(wl);
%MapOfLocExc=[delaytimes];

%define the limits for the map
pixel1=GetIndexByValue(wl,  wl_left);
pixel2=GetIndexByValue(wl, wl_right);



%calculate loc dynamics for each wavelength
for i=pixel1:1:pixel2

    locWl=wl(i);
    %disp(locWl);

    [X,Y] = GetDynamicsOfLocalizedExciton(SampleType, pristUVtime, dopedUVtime, locWl, refWl, norm,
CorrectionUsage, regime);
    %Y = SmoothAveraging (Y, 3);
    %Y(1)=wl(i);
    if ~exist("MapOfLocExc", 'var')
        MapOfLocExc=[X];
        MapOfLocExc(:,end+1)=Y;
        delaytimes=X;
    else
        [X, Y, MapOfLocExc]=tuneToSameX(X, Y, MapOfLocExc);
        delaytimes=X;
        MapOfLocExc(:,end+1)=Y;

    end

end
%adjust the values on the axes f the maps
wl_range=wl(pixel1:pixel2);
%i1=find(delaytimes==time_start);
%i2=find(delaytimes==time_end);
```

```
[~,i1] = min(abs(delaytimes-time_start));
[~,i2] = min(abs(delaytimes-time_end));
delaytimes_range=delaytimes(i1:i2);
delaytimes_range(1)=[];

%adjust the map for plotting in matlab
MapOfLocExc(1:i1-1,:)=[];
MapOfLocExc(i2+1:end,:)=[];

MapOfLocExc_range=MapOfLocExc;
MapOfLocExc_range(1,:) = [];
MapOfLocExc_range(:,1) = [];

N=100;
cmp=GenerateGreenZeroColorMap(MapOfLocExc_range);

for delaytime=delaytimes_range
    index = find(delaytimes_range==delaytime);
    sp=MapOfLocExc_range(index,:);
    sp=smoothdata(sp, "movmean", 5);
    MapOfLocExc_range(index,:)=sp;
end


fDynamicProfiles=figure('Name','DynamicProfiles');
movegui(fDynamicProfiles,[1580 -20]);
fSpectra=figure('Name','Spectra');
movegui(fSpectra,[980 -600]);
fMap=figure('Name','Map');
[C, h]=contourf( wl_range, delaytimes_range,  MapOfLocExc_range,  N);
set(h,'LineColor','none');
colormap jet;
%colormap(cmp);
w = waitforbuttonpress;
while w==0
    figure(fMap);
    [wl_click,delay_click] = ginput(1);

    figure(fDynamicProfiles)
        [~,i] = min(abs(wl_range-wl_click));
        plot(delaytimes_range, MapOfLocExc_range(:,i));
    hold on;

    figure(fSpectra)
        [~,i] = min(abs(delaytimes_range-delay_click));
        plot(wl_range, MapOfLocExc_range(i,:));
    hold on;

    figure(fMap);
    w = waitforbuttonpress;
end

hold off;


writematrix(MapOfLocExc, "MapOfLocExc.xls");
end
```

APPENDIX 5

Author also contributed to the following publications on adjacent fields not included in the present dissertation:

1. Kalachikova, P. M., Goldt, A. E., Khabushev, E. M., **Eremin, T. V**., Ustinovich, K. B., Grebenko, A., ... & Nasibulin, A. G. (2019). Direct injection of SWCNTs into liquid after supercritical nitrogen treatment. *Carbon*, *152*, 66-69.
2. Zaremba, O., Goldt, A., Ramirez-Morales, M., Khabushev, E. M., Shulga, E., **Eremin, T.**, ... & Nasibulin, A. G. (2019). Robust technique for dispersion of single-walled carbon nanotubes in aqueous solutions with tRNA. *Carbon*, *151*, 175-180.
3. **Eremin, T**., & Obraztsova, E. (2018). Optical Properties of Single-Walled Carbon Nanotubes Doped in Acid Medium. *physica status solidi (b)*, *255*(1), 1700272.
4. **Eremin, T. V**., Tonkikh, A. A., & Kudryashova, E. M. (2016). In situ Raman monitoring of single-walled carbon nanotube filling with copper chloride. *Journal of Nanophotonics*, *10*(1), 012516-012516.
5. Makarov, I. S., Golova, L. K., Vinogradov, M. I., Levin, I. S., Shandryuk, G. A., Arkharova, N. A., Golubev Y.V., Berkovich A.K., **Eremin T.V.**, Obraztsova, E. D. (2020). The effect of alcohol precipitants on structural and morphological features and thermal properties of lyocell fibers. *Fibers*, *8*(6), 43.

APPENDIX 6

Results reported in this dissertation have been presented in the following national and international conferences:

1. Eighth International Workshop Nanocarbon Photonics and Optoelectronics 31 July - 5 August, 2022, Holiday Centre Huhmari, Polvijärvi, Finland. Oral presentation "*Protonation of oxygen doped single-walled carbon nanotubes*"
2. Optics and Photonics Days 2022, 6-8 September, Tampere, Finland. Poster presentation "Protonation of oxygen doped single walled carbon nanotubes"
3. PREIN Workshop on Quantum Technologies, 10-11 November 2022. Joensuu, Finland. Oral presentation "*Zero-dimensional quantum defects in oxygen-doped carbon nanotubes*"
4. 36th International Winterschool on Electronic Properties of Novel Materials (IWEPNM,9-15 March , 2024, Kirchberg/Tirol, Austria. Poster presentation "Ultrafast exciton trapping dynamics in oxygen-doped single walled carbon nanotubes"

ARTICLES

ARTICLE I

Eremin, T.V., Obraztsov, P.A., Velikanov, V.A., Shubina, T.V. & Obraztsova, E.D.(2019). Many-particle excitations in non-covalently doped single-walled carbon nanotubes, *Scientific Reports*, 9, 1-8.

ARTICLE II

Eremin, T., Eremina, V., Svirko, Y., & Obraztsov, P. (2023). Over Two-Fold Photoluminescence Enhancement from Single-Walled Carbon Nanotubes Induced by Oxygen Doping. *Nanomaterials*, *13*(9), 1561.

ARTICLE III

Eremin, T., Dhama, R., Caglayan, H., & Obraztsov, P. (2024). Ultrafast exciton trapping dynamics in oxygen-functionalized single-walled carbon nanotubes. *Carbon*, 220, 118837.

ARTICLE I

Eremin, T.V., Obraztsov, P.A., Velikanov, V.A., Shubina, T.V. & Obraztsova, E.D.(2019). Many-particle excitations in non-covalently doped single-walled carbon nanotubes, *Scientific Reports*, 9, 1-8.

SCIENTIFIC REPORTS
nature research

OPEN

Many-particle excitations in non-covalently doped single-walled carbon nanotubes

Timofei V. Eremin[1,2,3*], Petr A. Obraztsov[2,4], Vladimir A. Velikanov[2,5], Tatiana V. Shubina[6] & Elena D. Obraztsova[2,3]

Doping of single-walled carbon nanotubes leads to the formation of new energy levels which are able to participate in optical processes. Here, we investigate (6,5)-single walled carbon nanotubes doped in a solution of hydrochloric acid using optical absorption, photoluminescence, and pump-probe transient absorption techniques. We find that, beyond a certain level of doping, the optical spectra of such nanotubes exhibit the spectral features related to two doping-induced levels, which we assign to a localized exciton *X* and a trion *T*, appearing in addition to an ordinary exciton E_1. We evaluate the formation and relaxation kinetics of respective states and demonstrate that the kinetics difference between E_1 and *X* energy levels perfectly matches the kinetics of the state *T*. This original finding evidences the formation of trions through nonradiative relaxation via the *X* level, rather than via a direct optical excitation from the ground energy state of nanotubes.

Multi-particle interactions exert a significant influence on physical properties of single-walled carbon nanotubes (SWNTs), as became clear after the first direct experimental confirmation of the excitonic nature of optical transitions in SWNTs[1]. Accounting for the electron-electron, electron-hole and exciton-phonon interactions allowed the successful explanation of a set of phenomena that were inexplicable with a simple non-interacting model. The ratio problem (the deviation of the second to first optical transition energy ratio from that predicted by commonly used theoretical models), a peculiarly low quantum yield of SWNT photoluminescence (PL) and the positions of phonon-side bands are among such phenomena[2,3]. Thus, many-body interactions in carbon nanotubes have become an increasingly active research area.

There is considerable interest in doped nanotubes, formed using various methods, such as chemical and gate doping, covalent functionalization, etc. Such modification methods may strongly impact the energy structure of SWNTs and yield new complex quasiparticles. Several different interpretations of these doping-induced many-particle energy levels can be found in the literature[4–20].

Theoretical studies by Rønnow *et al.* showed that the interaction of an exciton with either an electron or a hole in a SWNT may lead to the formation of a negatively or positively charged quasiparticle (known as a trion), respectively, detectable even at room temperature[4]. The first experimental confirmation of this prediction was done by Matsunaga *et al.*, who observed new peaks in absorption and PL spectra of SWNTs after p-doping with 2,3,5,6-tetrafluoro-7,7,8,8-tetracyanoquinodimethane (F4TCNQ) and hydrochloric acid (HCl)[5]. These new peaks were assigned to the optical transitions between the ground (non-excited) energy state of the nanotubes and a new doping-induced energy state, located approximately 100–200 meV (depending on the nanotube diameter) below the bright exciton, and attributed to the positive trion. It was also reported later that trions can be generated by all-optical excitations[6,7].

Later, applying doping methods such as gate-doping, electrochemical doping, chemical doping with F4TCNQ and HCl, several groups reported new features in linear absorption[8–10] and PL spectra[11–14] and attributed them to a direct optical excitation and a radiative decay of trions, respectively. Compared to the main exciton peak,

[1]Faculty of Physics of M.V. Lomonosov Moscow State University, Leninskie Gory str. 1, Moscow, 119991, Russia. [2]A.M. Prokhorov General Physics Institute of RAS, Vavilov str. 38, Moscow, 119991, Russia. [3]Moscow Institute of Physics and Technology, 9 Institutskiy per., Dolgoprudny, Moscow Region, 141701, Russia. [4]Department of Physics and Mathematics, University of Eastern Finland, Yliopistokatu 7, Joensuu, 80101, Finland. [5]National Research Nuclear University, Moscow Engineering Physics Institute, 31 Kashirskoe Highway, Moscow, 115409, Russia. [6]Ioffe Institute of RAS, Politechnicheskaya str. 26, St Petersburg, 194021, Russia. *email: timaeremin@yandex.ru

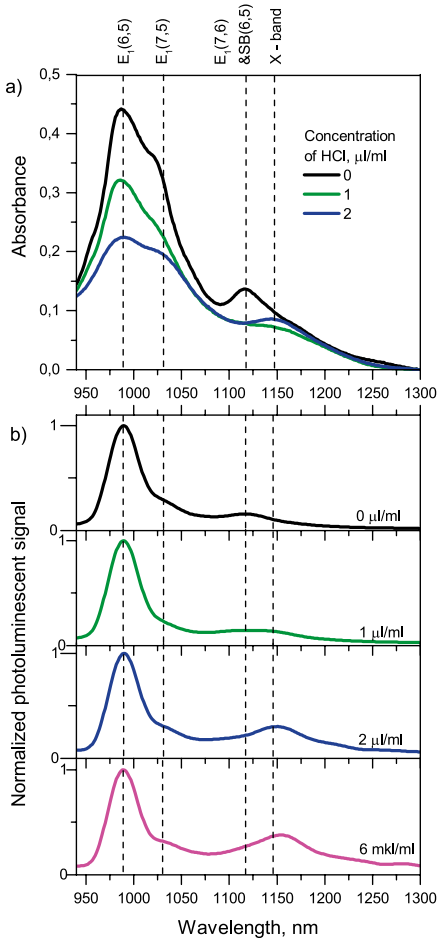

Figure 1. (**a**) Optical absorption spectra and (**b**) normalized PL spectra of the SWNT suspensions with different concentration of HCl.

such new peaks exhibit increased intensity with increased doping concentration, while the total absorbance and luminescence signal decreases.

On the other hand, a set of works have shown that the covalent functionalization of SWNTs leads to the appearance of very similar spectral features, i.e. the satellite peaks located 100–200 meV below the main exciton peak[15–20]. In these works, such peaks are attributed not to the trions but to the excitons, localized on defects which are introduced into the SWNT wall structure by covalent functionalization. The lower energy position of such excitons is usually explained as a result of modified potential in the defect vicinity. The exact position of these defect-localized excitons can be sensitive to the type of bonded functional group[18,20].

It is important to note that localization of excitons is not limited to the vicinity of defects induced by a covalent functionalization. A theoretical investigation by Tayo at al. indicated that charged particles, physisorbed on the surface of SWNTs, might play the role of localization centres for excitons[21]. It was also found experimentally in electrochemically doped nanotubes that both excitons and trions are spatially confined because of adsorbed ions, even without chemical bonding with the nanotube wall[22]. The temperature dependence of new doping-induced peaks in PL spectra confirmed the spatial localization of corresponding quasiparticles[23].

Brozena *et al.* observed defect-localized excitons in diazonium-functionalized SWNTs and the appearance of a second extra PL peak after chemical doping (reducing) of diazonium-functionalized SWNTs. This second peak was attributed to trions[24]. Thus, both localized excitons and trions can coexist in nanotubes modified with such a two-step method. A combination of covalent aryl functionalization and gate doping leads to the existence of both localized excitons and trions, as was reported by Shiraishi *et al.*[25]. Very recently, two different doping-induced

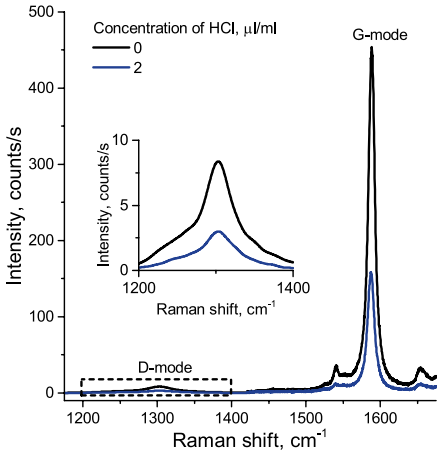

Figure 2. Raman spectra of the initial SWNT suspension (black line) and SWNT suspension with HCl (blue line). Inset: zoomed D-mode spectral region. The excitation wavelength is 633 nm.

levels were also reported by Bai at el. for SWNTs homogeneously non-covalently doped using K_2IrCl_6[26]; however, these levels were attributed to hole-polaron-dressed excitons and trions.

Bai *et al.* reported a one-picosecond trion formation time after the excitation of either an ordinary exciton or a hole-polaron-dressed exciton and concluded that trions are not formed as a result of the direct optical transition from the ground energy level, but rather via the intermediation of the hole-polaron-dressed exciton state. This finding contradicted previous works, since Nishihara *et al.* reported that trions can be generated via direct optical transitions from the ground energy level, using a model accounting for the dark exciton level[9], and Koyama *et al.* revealed that the trion level is occupied almost immediately (delay is less than 100 fs) after the occupation of the main exciton level[8].

In this work, we report the first observation of two doping-induced levels of different natures in SWNTs non-covalently doped with HCl. We ascribe these levels to the localized excitons and trions. We compare the ultrafast formation and relaxation dynamics of these photo-excitations in (6,5)-SWNTs doped by HCl and reveal that the occupation of the trion energy level occurs with a delay of 1 ps via the intermediary *X* level. Together with absorption and PL data, this finding indicates that the trions do not form via the direct optical excitation from the ground energy state in SWNTs noncovalently doped by HCl.

Results and Discussion

An aqueous suspension of (6,5)-enriched SWNTs coated with sodium dodecyl sulfate (SDS) was used in this research. Doping of the nanotubes was achieved by adding HCl to this suspension.

Figure 1a shows the optical absorption spectra of SWNT suspensions with different concentrations of HCl. The three peaks labelled $E_1(6,5)$, $E_1(7,5)$ and $E_1(7,6)$ in the spectrum of a non-doped sample (black line) correspond to the excitation of the first bright excitonic states in nanotubes with the indicated chiral indexes. With increasing concentration of HCl, one can observe a gradual suppression of all three excitonic peaks. At a concentration of 1 μl/ml, the $E_1(7,6)$ peak is totally suppressed (dark green line). At a higher concentration (2 μl/ml), the gradual rise of a new peak, labelled X, located around 1140–1160 nm is observed (blue line).

Figure 1b shows the normalized PL spectra of suspensions with different concentrations of HCl under the resonant excitation of the second bright exciton E_2 in (6,5) nanotubes (570 nm). The brightest peak at 990 nm corresponds to the radiative decay of the first bright exciton in (6,5)-SWNTs. A faint peak around 1025–1030 nm should be assigned to the emission from (7,5) nanotubes, which appeared due to an exciton energy transfer (EET) from a (6,5) nanotube[27]. A spectral feature at 1120 nm, labelled $E_1(7,6) + SB(6,5)$, might consist of two overlapped peaks: a signal of an EET process from (6,5) to (7,6) nanotubes and a phonon-side photoluminescence band[28,29], associated with (6,5) nanotubes.

In the rest of this paper, we omit chiral indices (n,m) in $E_1(n,m)$, as we only discuss (6,5) nanotubes. When the HCl concentration is greater than 1 μl/ml, we observe the gradual rise of a new PL peak around 1140–1160 nm, labelled *X*. We suggest that the observable red-shift of the *X* band from 1140 nm to 1160 nm is due to the influence of HCl on the local dielectric constant and, consequently, to the screening efficiency[30].

In order to check the influence of HCl on the structure of SWNT, we performed Raman measurements (see Fig. 2.). Since we do not observe a rise of the "defective" D-mode compared to the G-mode with increasing of HCl concentration, we conclude that adding of HCl does not lead to the formation of defects in the structure of SWNT.

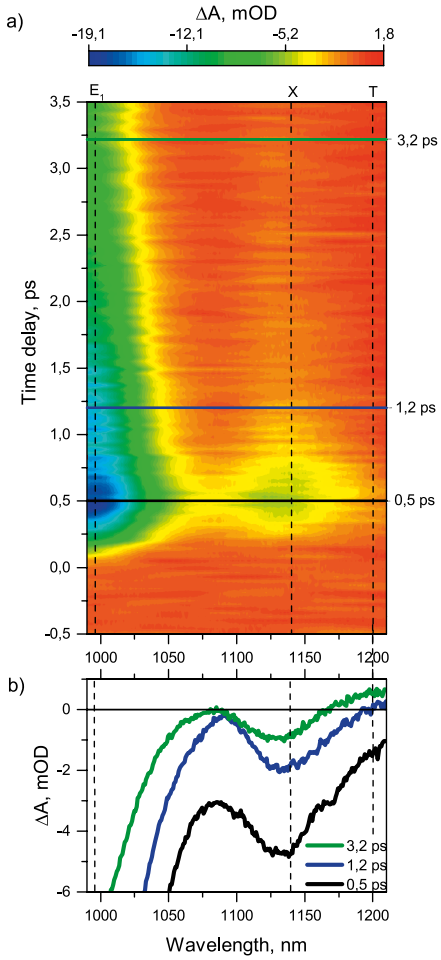

Figure 3. (**a**) Time dependence of the absorbance change signal of the suspension pumped at 570 nm. (**b**) Differential absorption spectra of the suspension taken at several different delay times.

The suspension with 2 µl/ml HCl exhibiting the bright *X* spectral features (solid blue lines in Fig. 1a,b) was investigated by the pump-probe technique. The colour map in Fig. 3a shows a dependence of the induced sample optical density on the time delay between a pump pulse centred at E_2 resonance of (6,5) nanotubes (570 nm) and a probe pulse covering the spectral region 990–1210 nm. The occupancy of the first bright excitonic level of (6,5) nanotubes reveals itself as an induced transmittance at 990 nm. Since both optical absorption and PL data demonstrate that, under concentrations of HCL higher than 1 µl/ml, the (6,5)-SWNTs exhibit an additional optically active energy level *X* appearing as a peak around 1140–1160 nm, we assign an induced transmittance signal centred approximately at 1140 nm in Fig. 3a to the same energy level X.

The differential absorption spectra taken at different delay times between pump and probe pulses (horizontal cuts in Fig. 3a) are shown in Fig. 3b. One can see that along with the induced transmittance features E_1 and *X* there is a significant induced absorption signal around 1200 nm, labelled *T*.

The time evolution of E_1 and *X* energy levels are obtained as vertical cuts in Fig. 3a at 990 nm and 1140 nm and plotted as blue and red lines in Fig. 4, respectively. Thin noisy lines are experimental data, while the solid lines refer to bi-exponential fitting curves.

Although the *T* spectral feature is clearly observable at delay times exceeding 1 picosecond (green line in Fig. 2b), at shorter time delays it is buried under the strong induced transmittance signal *X* due to, inter alia, a lack of material homogeneity. Therefore, the time evolution of the *T*-associated energy level cannot be obtained

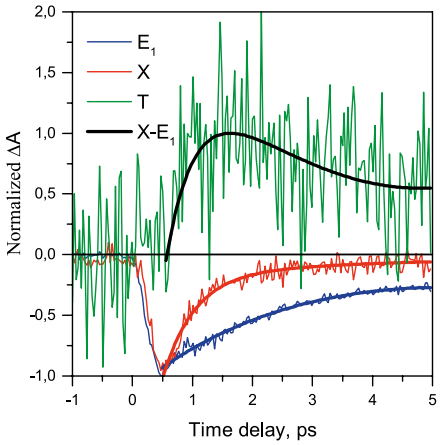

Figure 4. Measured dynamics of E (blue lines), X (red lines) and T energy level (green line). The black line shows the difference between X and E_1 dynamics.

simply from a vertical cut of Fig. 3a at 1200 nm, and the side slope signal of the *X* band should be subtracted with the necessary normalization.

Applying such a procedure, we obtain dynamics of the *T*-associated energy level (as shown by green line in Fig. 4). It is clearly seen that the formation of *T*-states occurs with a delay of about 1 ps after the formation of the ordinary E_1 exciton and *X* states. This finding signifies that the *T* spectral feature does not correspond to either *X* or E_1 energy levels, but is associated with another energy level (see Fig. 5).

Similar dynamics of the ordinary exciton and the doping-induced states was recently observed by Bai *et al.*[26] in highly electrically and geometrically homogeneous (6,5)-SWNTs non-covalently doped with K_2IrCl_6. Thus, here we confirm their findings for the case of less homogeneous (6,5)-SWNTs, doped with HCl.

The black line in Fig. 4 shows the difference in occupation of E_1 and *X* energy levels and indicates faster relaxation dynamics of the *X* energy level. The difference in relaxation dynamics of these two levels (black line in Fig. 4) precisely matches the dynamics of the *T* energy level (green line in Fig. 4). This original finding strongly supports the appearance of additional ultrafast energy relaxation channel of *X* states through the doping-induced energetically lower lying states, namely, the formation of the *T* states.

The absence of a distinct signal at 1200 nm in PL and linear optical absorption spectra indicates that optical transitions between the ground energy level (*Gr*) of the nanotubes and the T energy level ($Gr => T$ and $T => Gr$ transitions) have very low oscillator strength at 1200 nm compared to the oscillator strength of $Gr => X$ and $X => Gr$ transitions at 1140 nm. Thus, in our experimental conditions, the *T* states are formed via a nonradiative relaxation from the *X* energy level, but not via the direct optical transition from the *ground* energy level of nanotubes (see crossed-out arrow in Fig. 5).

We further speculate on the physical nature of *X* and *T* energy levels (see Fig. 5) and compare our results with those obtained in previous works. The authors who attributed the *X* energy level to trion[5,8–14], did not observed a second doping-induced level *T*, as we do in this work. In contrast, in works where two different doping-induced levels were observed[24–26], and also in several other works[15–20], the *X* energy level is ascribed either to a defect-localized exciton or to a hole-polaron-dressed exciton. Since we do not observe a rise of the "defective" D-mode in the Raman spectra with HCl added (see Fig. 2), we reject the hypothesis of defect-localized excitonic states[12]. However, both theoretical[21] and experimental[22] studies have shown that excitons may localize due to the impact of ions adsorbed on the surface of SWNTs, even without covalent bonds. Thus, one should ascribe the *X* energy level either to the hole-polaron-dressed exciton or to the excitons localized on the sites of physically adsorbed H^+ ions. Due to the theoretical support, we are inclined to favour the latter hypothesis, although further experimental studies, such as Fourier-transform infrared spectroscopy and x-ray photoelectron spectroscopy measurement, should be done to clearly specify the physical nature of the *X* energy level.

Regarding interpretation of the second doping-induced level *T*, located energetically below the X level, we follow previous works and ascribe it to the trion energy level[24–26]. However, in contradiction to some other works[24,25], but in consonance with Bai *et al.*[26], we find that the $Gr => T$ and $T => Gr$ transitions are optically inactive. This discrepancy might be caused by specific doping techniques and environmental circumstances. Following Bai *et al.*[26], we attribute the *T* transient absorption spectral feature around 1200 nm to the $T => T^*$ optical transition, where T^* denote an excited trion state (see Fig. 5). Such an interpretation is in agreement with theoretical work[31], claiming that not only one but rather a set of trion levels exist in SWNTs.

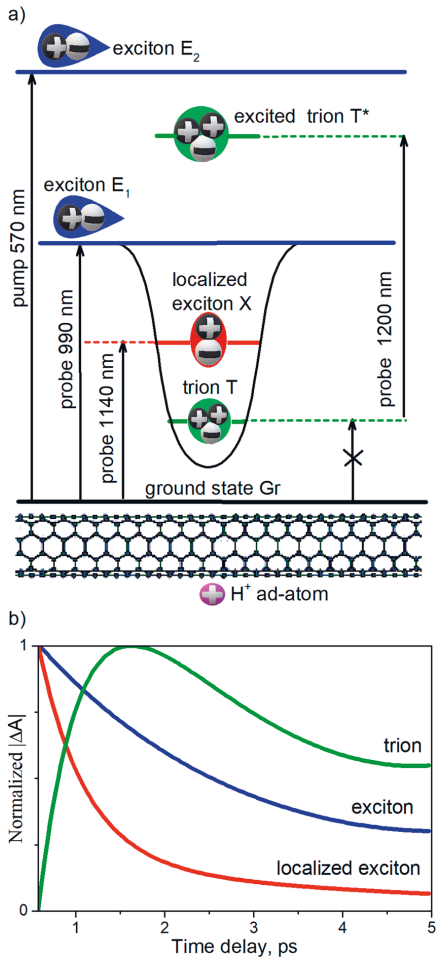

Figure 5. (**a**) Proposed simplified scheme of energy structure of SWNTs doped with HCl. (**b**) Established dynamics of main energy levels in the system (**b**).

Conclusion

To summarize, we provide new physical insight on the energy structure of SWNTs doped with hydrochloric acid and on the physical nature and behaviour of the corresponding many-particle excitations in such modified nanomaterial. We observed two doping-induced energy levels *X* and *T* in HCl-doped (6,5)-SWNTs, which we cautiously ascribe to the exciton, localized on the physisorbed H + ion, and to the trion, respectively. We present an original finding showing that the dynamics of the trion states matches the difference between the dynamics of the ordinary exciton E_1 and the exciton *X*, localized on the physisorbed ion. Thus, our results strongly suggest that the SWNT trion energy level *T* in HCl-doped (6,5)-SWNTs is occupied via relaxation from the *X* energy level, but not via a direct optical excitation from the ground energy level of nanotube. These findings significantly contribute to understanding the energy structure of doped SWNTs and many-body interactions in low-dimensional materials, although further studies should be aimed at the accurate attribution of energy levels in SWNTs, doped by different methods.

Materials and Methods

A powder of (6,5)-enriched CoMoCat single-walled carbon nanotubes (Sigma-Aldrich) was dissolved in an aqueous 2% solution of SDS in concentration of 0.05 μg/ml involving 4 hours of tip sonication. The obtained suspension was ultracentrifuged (120000 g) for 1 hour, and supernatant was collected for further research. Doping was performed by adding concentrated hydrochloric acid into a quartz cuvette containing 1 ml of the suspension. The

linear optical absorption and PL measurements dealt with the quartz cuvette, while for the pump-probe measurements the suspension was placed between two glass windows, making the optical length of the sample of 2 mm.

The linear optical absorption measurements were done using a two-channel PerkinElmer Lambda 950 spectrophotometer. For PL measurements a "Nanolog-4" spectrofluorimeter (*Horiba*) was used, with a xenon lamp as the excitation light source and a nitrogen-cooled InGaAs matrix as the detector. The installation has already been used in our previous studies[32,33].

To perform the time-resolved measurements and to reveal the ultrafast dynamics of different relaxation channels in initial and HCl doped SWNT we employed a multicolor transient absorption pump−probe setup based on Ti:sapphire 40 fs laser. A detailed description of the method and setup we reported previously and can be found elsewhere[34,35]. The femtosecond pulses with a central wavelength tunable in the 1000–1700 nm range and a femtosecond continuum were employed as pump and probe, respectively. The pump pulses were delivered by an optical parametric amplifier (OPA), which was excited by a Ti:sapphire regenerative femtosecond amplifier (800 nm wavelength, 40 fs pulse duration, 1 kHz repetition rate). The probe continuum pulses were generated by focusing the beam (at the wavelength of 800 nm and with an average power of 100 mW) in a sapphire crystal. The diameter of the pump beam at the sample surface was about 500 μm. The femtosecond continuum was used to probe the absorbance change (ΔA) in a wide spectral range spanning from 900 nm up to 1300 nm. The visible part of the continuum generated in the sapphire crystal was removed from the probe channel using a long-pass filter. The pump and probe beams were polarized collinearly. The time delay between the probe and the pump pulses was controlled by a rapid motorized delay line. The pump-induced change of the probe absorption was detected with an IR-spectrometer (CDP ExciPro 2012). All measurements were performed at room temperature.

Data availability

The datasets generated and analysed during the current study are available in the Google Drive repository via the following link: https://drive.google.com/file/d/1C-OrsueR7Y_cxvAkLPVPYJEnJ1p_TVUm/view?usp=sharin.

Received: 19 April 2019; Accepted: 6 September 2019;
Published online: 18 October 2019

References

1. Wang, F. The Optical Resonances in Carbon Nanotubes Arise from Excitons. *Science (80-).* **308**, 838–841 (2005).
2. Miyauchi, Y. Photoluminescence studies on exciton photophysics in carbon nanotubes. *J. Mater. Chem. C* **1**, 6499–6521 (2013).
3. Dresselhaus, M. S., Dresselhaus, G., Saito, R. & Jorio, A. Exciton Photophysics of Carbon Nanotubes. *Annu. Rev. Phys. Chem.* **58**, 719–747 (2007).
4. Rønnow, T. F., Pedersen, T. G. & Cornean, H. D. Correlation and dimensional effects of trions in carbon nanotubes. *Phys. Rev. B - Condens. Matter Mater. Phys.* **81**, 1–7 (2010).
5. Matsunaga, R., Matsuda, K. & Kanemitsu, Y. Observation of charged excitons in hole-doped carbon nanotubes using photoluminescence and absorption spectroscopy. *Phys. Rev. Lett.* **106**, 1–4 (2011).
6. Santos, S. M. *et al*. All-optical trion generation in single-walled carbon nanotubes. *Phys. Rev. Lett.* **107**, 187401 (2011).
7. Yuma, B. *et al*. Biexciton, single carrier, and trion generation dynamics in single-walled carbon nanotubes. *Phys. Rev. B - Condens. Matter Mater. Phys.* **87**, 1–10 (2013).
8. Koyama, T., Shimizu, S., Miyata, Y., Shinohara, H. & Nakamura, A. Ultrafast formation and decay dynamics of trions in p-doped single-walled carbon nanotubes. *Phys. Rev. B - Condens. Matter Mater. Phys.* **87**, 3–8 (2013).
9. Nishihara, T., Yamada, Y., Okano, M. & Kanemitsu, Y. Trion formation and recombination dynamics in hole-doped single-walled carbon nanotubes. *Appl. Phys. Lett.* **103**, 023101 (2013).
10. Hartleb, H., Spath, F. & Hertel, T. Evidence for Strong Electronic Correlations in the Spectra of Gate-Doped Single-Wall Carbon Nanotubes. *ACS Nano* **9**, 10461–10470 (2015).
11. Park, J. S. *et al*. Observation of negative and positive trions in the electrochemically carrier-doped single-walled carbon nanotubes. *J. Am. Chem. Soc.* **134**, 14461–14466 (2012).
12. Eremin, T. & Obraztsova, E. Optical Properties of Single-Walled Carbon Nanotubes Doped in Acid Medium. *Phys. Status Solidi Basic Res.* **255**, 1700272 (2018).
13. Yoshida, M., Popert, A. & Kato, Y. K. Gate-voltage induced trions in suspended carbon nanotubes. *Phys. Rev. B - Condens. Matter Mater. Phys.* **93**, 1–5 (2016).
14. Jakubka, F., Grimm, S. B., Zakharko, Y., Gannott, F. & Zaumseil, J. Trion Electroluminescence from Semiconducting Carbon Nanotubes. *ACS Nano* **8**, 1–7 (2014).
15. Akizuki, N., Aota, S., Mouri, S., Matsuda, K. & Miyauchi, Y. Efficient near-infrared up-conversion photoluminescence in carbon nanotubes. *Nat. Commun.* **6**, 1–6 (2015).
16. Harutyunyan, H. *et al*. Photoluminescence from disorder induced states in individual single-walled carbon nanotubes. *Phys. Status Solidi* **246**, 2679–2682 (2009).
17. Iwamura, M. *et al*. Nonlinear Photoluminescence Spectroscopy of Carbon Nanotubes with Localized Exciton States. *ACS Nano* **8**, 11254–11260 (2014).
18. He, X. *et al*. SUPPLEMENTARY Tunable room-Temperature single-photon emission at telecom wavelengths from sp 3 defects in carbon nanotubes. *Nat. Photonics* **11**, 577–582 (2017).
19. Ghosh, S., Bachilo, S. M., Simonette, R. A., Beckingham, K. M. & Weisman, R. B. Oxygen doping modifies near-infrared band gaps in fluorescent single-walled carbon nanotubes. *Science (80-).* **330**, 1656–1659 (2010).
20. Kwon, H. *et al*. Molecularly Tunable Fluorescent Quantum Defects. *J. Am. Chem. Soc.* **138**, 6878–6885 (2016).
21. Tayo, B. O. & Rotkin, S. V. Charge impurity as a localization center for singlet excitons in single-wall nanotubes. *Phys. Rev. B - Condens. Matter Mater. Phys.* **86**, 1–8 (2012).
22. Eckstein, K. H., Hartleb, H., Achsnich, M. M., Schöppler, F. & Hertel, T. Localized Charges Control Exciton Energetics and Energy Dissipation in Doped Carbon Nanotubes. *ACS Nano* **11**, 10401–10408 (2017).
23. Mouri, S., Miyauchi, Y., Iwamura, M. & Matsuda, K. Temperature dependence of photoluminescence spectra in hole-doped single-walled carbon nanotubes: Implications of trion localization. *Phys. Rev. B - Condens. Matter Mater. Phys.* **87**, 1–4 (2013).
24. Brozena, A. H., Leeds, J. D., Zhang, Y., Fourkas, J. T. & Wang, Y. Controlled defects in semiconducting carbon nanotubes promote efficient generation and luminescence of trions. *ACS Nano* **8**, 4239–4247 (2014).
25. Shiraishi, T., Shiraki, T. & Nakashima, N. Substituent Effects on the Redox States of Locally Functionalized Single-Walled Carbon Nanotubes Revealed by *in situ* Photoluminescence Spectroelectrochemistry. *Nanoscale* **9**, 16900–16907 (2017).

26. Bai, Y., Olivier, J.-H., Bullard, G., Liu, C. & Therien, M. J. Dynamics of charged excitons in electronically and morphologically homogeneous single-walled carbon nanotubes. *Proc. Natl. Acad. Sci.* 201712971, https://doi.org/10.1073/pnas.1712971115 (2018).
27. Ma, Y. Z., Valkunas, L., Dexheimer, S. L., Bachilo, S. M. & Fleming, G. R. Femtosecond spectroscopy of optical excitations in single-walled carbon nanotubes: Evidence for exciton-exciton annihilation. *Phys. Rev. Lett.* **94**, 1–4 (2005).
28. Vora, P. M., Tu, X., Mele, E. J., Zheng, M. & Kikkawa, J. M. Chirality dependence of the K -momentum dark excitons in carbon nanotubes. *Phys. Rev. B - Condens. Matter Mater. Phys.* **81**, 1–9 (2010).
29. Kadria-Vili, Y., Bachilo, S. M., Blackburn, J. L. & Weisman, R. B. Photoluminescence Side Band Spectroscopy of Individual Single-Walled Carbon Nanotubes. *J. Phys. Chem. C* **120**, 23898–23904 (2016).
30. Miyauchi, Y. *et al*. Dependence of exciton transition energy of single-walled carbon nanotubes on surrounding dielectric materials. *Chem. Phys. Lett.* **442**, 394–399 (2007).
31. Deilmann, T., Drüppel, M. & Rohlfing, M. Three-particle correlation from a Many-Body Perspective: Trions in a Carbon Nanotube. *Phys. Rev. Lett.* **116**, 1–6 (2016).
32. He, M., Chernov, A. I., Fedotov, P. V. & Obraztsova, E. D. Predominant (6, 5) Single-walled Carbon Nanotube Growth on a Copper Promoted Iron Catalyst. *J. Am. Chem. Soc.* **132**, 13994–13996 (2010).
33. Chernov, A. I. *et al*. Optical Properties of Graphene Nanoribbons Encapsulated in Single-Walled Carbon Nanotubes. 6346–6353 (2013).
34. Obraztsov, P. A. *et al*. Broadband light-induced absorbance change in multilayer graphene. *Nano Lett.* **11**, 1540–1545 (2011).
35. Obraztsov, P. A. *et al*. Coherent Detection of Terahertz Radiation with Graphene. *ACS Photonics* **6**, 1780–1788 (2019).

Acknowledgements
This work was supported by RFBR projects 17-302-50008 and 19-02-00859_A. The work was partially supported by Russian Science Foundation grant #17-72-10303 (in part of pump-probe measurements) and Academy of Finland Grant #318596. T.V.S. appreciates the partial support by the Russian Science Foundation (project # 19-12-00273).

Author contributions
T.V.E. and V.A.V. prepared the samples and carried out photoluminescence, static absorption, and Raman measurements. P.A.O. carried out pump-probe measurements. T.V.E. and P.A.O. analyzed the data. T.V.S. and E.D.O. supervised the project. T.V.E. wrote the main part of the manuscript. All authors discussed the results and reviewed the manuscript.

Competing interests
The authors declare no competing interests.

Additional information
Correspondence and requests for materials should be addressed to T.V.E.

Reprints and permissions information is available at www.nature.com/reprints.

Publisher's note Springer Nature remains neutral with regard to jurisdictional claims in published maps and institutional affiliations.

ARTICLE II

Eremin, T., Eremina, V., Svirko, Y., & Obraztsov, P. (2023). Over Two-Fold Photoluminescence Enhancement from Single-Walled Carbon Nanotubes Induced by Oxygen Doping. *Nanomaterials*, *13*(9), 1561.

nanomaterials

MDPI

Article

Over Two-Fold Photoluminescence Enhancement from Single-Walled Carbon Nanotubes Induced by Oxygen Doping

Timofei Eremin, Valentina Eremina, Yuri Svirko and Petr Obraztsov *

Department of Physics and Mathematics, Center for Photonics Sciences, University of Eastern Finland, Yliopistokatu 2, 80101 Joensuu, Finland; timofei.eremin@uef.fi (T.E.)
* Correspondence: petr.obraztsov@uef.fi

Abstract: Covalent functionalization of single-walled carbon nanotubes (SWCNTs) is a promising way to improve their photoluminescent (PL) brightness and thus make them applicable as a base material for infrared light emitters. We report as high as over two-fold enhancement of the SWCNT PL brightness by using oxygen doping via the UV photodissociation of hypochlorite ions. By analyzing the temporal evolution of the PL and Raman spectra of SWCNTs in the course of the doping process, we conclude that the enhancement of SWCNTs PL brightness depends on the homogeneity of induced quantum defects distribution over the SWCNT surface.

Keywords: photoluminescence; carbon nanotubes; doping; quantum defects

Citation: Eremin, T.; Eremina, V.; Svirko, Y.; Obraztsov, P. Over Two-Fold Photoluminescence Enhancement from Single-Walled Carbon Nanotubes Induced by Oxygen Doping. *Nanomaterials* **2023**, *13*, 1561. https://doi.org/10.3390/nano13091561

Academic Editors: Jian Zhou, Ruifeng Lu, Jianing Chen, Bin Yang and Kun Zhao

Received: 10 April 2023
Revised: 28 April 2023
Accepted: 4 May 2023
Published: 6 May 2023

1. Introduction

Single-walled carbon nanotubes (SWCNTs) are hollow cylindrical carbon structures with a nanometer-scale diameter and length ranging from a few tens of nanometers to tens of microns [1]. One of the most intriguing properties of SWCNTs is their stable excitonic near-infrared photoluminescence (PL), which depends on their diameter and chirality [2]. This has generated great interest in the development of SWCNT-based infrared light emitters, including single-photon sources [3], LEDs, and bioimaging probes [4]. However, a very low quantum yield [5], which is suppressed by exciton quenching on defective SWCNT sites [6] due to free exciton diffusion, essentially limits the application range of SWCNTs light emitters in practice. Another critical factor that suppresses the PL quantum yield is the presence of dark excitons. Being energetically downshifted compared with bright excitons, they provide an additional pathway for the nonradiative relaxation of photoexcitation [7].

These limitations can be overcome by introducing traps along the SWCNT by covalent sp^3 functionalization, which is a promising way to improve the PL brightness. Specifically, this can be completed by adding functional groups capable to create "bright" sp^3 defects, in the vicinity of which the trapped excitons will radiatively recombine before quenching on intrinsic SWCNT defects [8–15]. The energy level of such a trapped exciton might be energetically downshifted compared to the dark exciton level thus preventing the quantum yield suppression. Eventually, such sp^3 functionalization of SWCNTs may lead to an improvement in the PL brightness of the SWCNTs by a factor of 4.2 [16]. Furthermore, doping SWCNT with sp^3 not only results in a substantial enhancement in the PL brightness but also induces photon antibunching, enabling the use of sp^3doped SWCNT as single-photon emitters even at room temperature [17,18]. This phenomenon can be explained by the localization of excitons near artificially induced defects, where the trapping potentials are deep enough to prevent thermal de-trapping even at room temperature. Nevertheless, it should be noted that the sp^3 doping process for SWCNT is complex and time-consuming, involving multiple steps that may take from several hours [14] to several days [16].

Oxygen doping provides an alternative method for creating zero-dimensional traps in SWCNTs. Oxygen adducts in oxygen-doped carbon nanotubes can take on several

chemical configurations, including the formation of an epoxide bond between an oxygen atom and two adjacent sp^3 carbon atoms and the formation of an ether bond between an oxygen atom and two sp^2 carbon atoms nearly parallel (ether-l) or perpendicular (ether-d) to the nanotube axis through C-O-C bonds [19]. The most stable configuration, ether-d, is primarily responsible for the changes observed in the optical properties of the SWCNTs resulting from oxygen doping [20]. Oxygen defects in SWCNT structure also enable deep trapping of excitons providing efficient single-photon emission [17] and also possess good perspectives for spectrally-resolved bioimaging [4]. The conventional oxygen doping technique is also quite a time-consuming procedure, which involves the exposure of SWCNT to ozone with subsequent UV irradiation of up to 16 h [4,20–24]. However, it has been recently demonstrated [25] that boosting PL brightness by a factor of 1.36 on a minute timescale can be achieved by a very simple method of SWCNT oxygen doping based on the photodissociation of hypochlorite ions. The technological simplicity, efficiency, and scalability of this method make it highly promising for the development of IR light emitters based on oxygen-doped SWCNTs (O-SWCNTs) provided a higher brightness enhancement factor will be achieved.

Here, we report a modification of the oxygen doping method based on hypochlorite ion photodissociation, which provides a record high—by more than a factor of 2—enhancement of the SWCNT PL brightness. By analyzing the defect formation in the structure of SWCNTs during oxygen doping, we revealed that the homogeneity of the oxygen atom distribution along the SWCNT surface is of crucial importance for achieving the bright PL of oxygen-doped SWCNTs.

2. Materials and Methods

The commercially available (6,5)-enriched CoMoCat SWCNT purchased from Merk was suspended in a concentration of 0.1 mg/mL in Sodium dodecyl sulfate (SDS) solution (2%) by 4-h tip-sonication (model Hielsher UP200, manufacturer Hielscher Ultrasonics GmbH (Teltow, Germany), integrated power 200 W, on/off cycle ratio 0.1, volume of the treated suspension 50 mL), followed by 1 h ultracentrifugation (125,000$\times$ *g*). Approximately 80% of the supernatant was collected and used for further research. Before doping, the SWCNT suspension was diluted 10 times with water to reduce the SDS concentration to 0.2%.

The employed doping procedure is a modification of the method reported in [25]. NaOCl solution (2 mg/L) was added to the SWCNT suspension at a concentration of 50 µL/mL. Subsequently, an open quartz cuvette (10 $\times$ 10 $\times$ 35 mm) with 2 mL of SWCNT suspension was centered right under the UVC mercury lamp (model UVL-10 Ozone, manufacturer LLC "UVL" (Istra, Russia), max intensity at 254 nm, power density 27 µW/cm^2). The distance between the lamp and the surface of the suspension was approximately 15 mm. Doping was performed by exposing the suspension to UV light for a certain period of time. This method allowed us to temporarily suspend doping and perform spectroscopic measurements.

To perform Raman measurements, the cuvette was inclined and the sample was excited through the cuvette wall with a laser beam focused 2–3 mm below the cuvette edge. A diode laser with a wavelength of 532 nm was utilized as the excitation source, and the signal was collected in a backscattering configuration.

The suspensions were subjected to spectroscopic measurements using the same cuvette used for the doping. PL maps were obtained by exciting the samples with a Xe lamp for visible range excitation and a tunable CW titanium-sapphire laser for NIR excitation. The reported PL spectra were acquired under excitation with an 840 nm wavelength Ti:sapphire laser (model 3900s, manufacturer Spectra-Physics, Milpitas, CA, USA), unless stated otherwise. The excitation beam was defocused on the sample (diameter of the beam was 2–3 mm) and the PL signal was detected using an InGaAs array.

A two-channel spectrophotometer (model Lambda 900, manufacturer Perkin Elmer, Waltham, MA, USA) was used to measure the optical absorption spectra. The thickness of the optical path was 10 mm.

3. Results

Figure 1a displays the excitation-emission PL map of a pristine SWCNT suspension. The color scale is normalized based on the maximum intensities for the 475–720 nm and 720–1000 nm spectral regions, separately. This normalization was required because different excitation sources, the Xe lamp and CW Ti:sapphire laser, were used for these regions with varying power levels. The main observed PL features are indicated with notation $(n,m)^{em}_{abs}$, where (n,m) refers to the chiral indices of the corresponding SWCNT, which describe the crystalline structure of the SWCNT, including diameter and chirality, and thus the energy of excitonic transitions. The subscript and superscript indices describe absorptive and emissive energy levels during the PL process, respectively. Therefore, the predominant spectral feature $(6,5)^{11}_{22}$ corresponds to light absorption by the E_{22} exciton of (6,5)-SWCNT and subsequent light emission by the E_{11} exciton of SWCNT with (6,5) chirality.

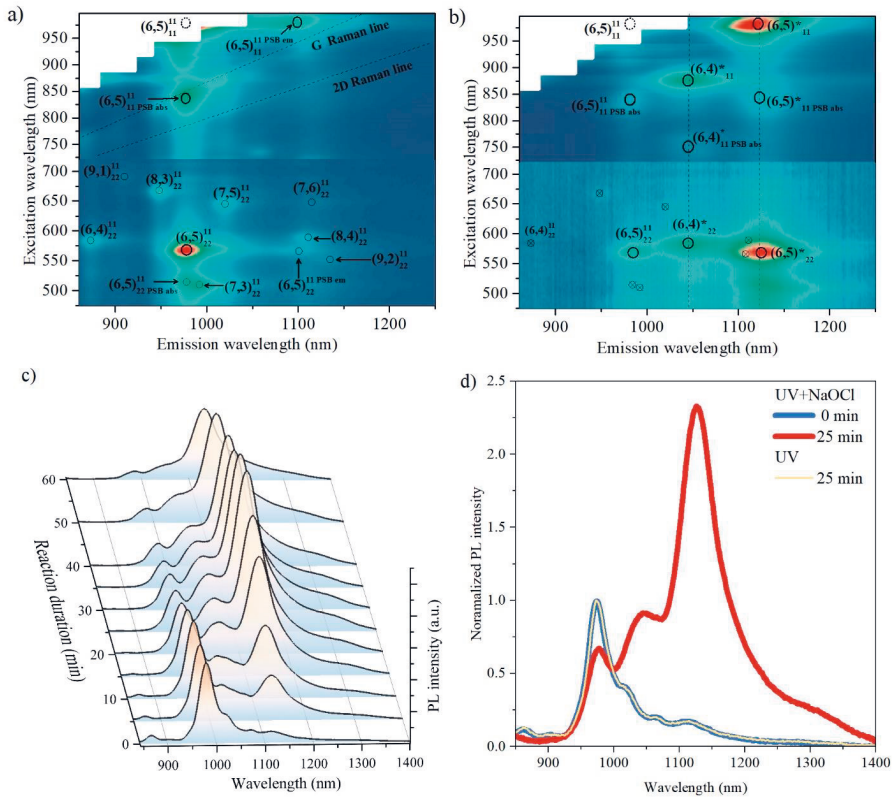

Figure 1. Excitation-emission photoluminescence (PL) maps of pristine single-walled carbon nanotubes (SWCNTs) (**a**) and O-doped SWCNTs (**b**). A contrast horizontal lines at 720 nm separate maps obtained using different excitation source (Xe lamp for visible and Ti:sapphire laser for NIR), color scale normalized separately for each part (blue for 0 and red for 1). New spectral features appeared due to the oxygen doping are marked with * sign. (**c**) Evolution of PL spectra of SWCNTs during the doping procedure. (**d**) Comparison of SWCNT PL spectra before O-doping and at the optimum doping concentration. The excitation wavelength is 840 nm.

Other optical features correspond to residual PL of SWCNTs having (6,4), (8,3), (7,5), (8,4), and (7,3) chiralities. The assignment of the optical features to SWCNT chiralities is based on the dataset published in [2].

The diameters of SWCNTs in the suspension range from 0.69 nm to 0.84 nm. The length of SWCNTs cannot be accurately estimated using the employed spectroscopic methods, but it is expected to be on the order of a few hundred nanometers based on the employed manufacturing of the samples [26].

For purposes of the further discussion we note here the observation of emission and absorption phonon-side bands (PSB), which result from the involvement of a phonon in the process of exciton recombination and excitation, respectively. For example, the $(6,5)^{11}_{11PSBabs}$ spectral feature with a resonant excitation wavelength of 840 nm and an emission wavelength of 980 nm, corresponds to the simultaneous excitation of a K-momentum dark exciton from the E_{11} manifold and the band-edge phonon with subsequent light emission by bright E_{11} exciton [5]. Taking into account spectral positions of the $(6,5)^{11}_{11PSBabs}$ and $(6,5)^{11PSBem}_{11}$ phonon-side bands to determine the position of the $(6,5)^{11}_{11}$ spectral feature which is marked with a dashed circle. This is not observable in the performed experiment due to huge scattering of laser excitation line (brown rectangles in Figure 1a,b)

Upon doping the SWCNTs with NaOCl and exposing them to UV light, significant changes in the PL map were observed, as shown in Figure 1b. Specifically, new emission bands appeared at approximately 1145 nm and 1130 nm, which are indicated by dashed vertical lines, whereas, the original spectral features were partially suppressed (see Figure S1 in the Supplementary Materials for the comparison of peak intensities).The new spectral feature with an emission wavelength centered at 1130 nm has several resonant excitation wavelengths, namely, 568 nm, 840 nm, and 980 nm, which perfectly match the resonance conditions of $(6,5)^{11}_{22}$, $(6,5)^{11}_{11PSBabs}$, and $(6,5)^{11}_{11}$, respectively (see Figure 1b). Based on this observation, we attribute the emission band at 1130 nm to the emission from (6,5)-SWCNT. Similarly, the emission line centered at 1045 nm should be associated with the (6,4)-SWCNT. No new emission bands associated with SWCNTs of other chiralities were observed because of their low concentration in the sample.

The emission wavelengths of the new spectral features are close to previously reported values for the recombination energy of excitons localized in the vicinity of O atoms in oxygen-doped carbon nanotubes [20]. This confirms efficient oxygen doping of SWCNTs via interaction with NaOCl under UV exposure and allows the determination of the physical nature of the new emission bands as a result of the radiative recombination of these zero-dimensional excitons. The localized exciton energy level is marked with a '*' sign.

Figure 1c shows the evolution of the SWCNTs PL spectrum during the doping procedure. To focus on SWCNT with predominant (6,5) chirality, we used an excitation wavelength of 840 nm, which coincides with the absorbance PSB resonance of (6,5) SWCNT and is spectrally well-separated from the absorption resonances of SWCNT with other chiralities. Further, we omit the detailed notation of the PL spectral features and use a short designation (6,5) instead of $(6,5)^{11}_{11PSBabs}$ and (6,5)* instead of $(6,5)^{*11}_{11PSBabs}$. As the UV exposure time increased, the intensity of the (6,5) band decreased monotonically.The behavior of the (6,5)* band in the PL spectrum is more complicated; the intensity of the new band increases until it reaches its maximum after approximately 20–25 min of UV exposure. The subsequent UV exposure led to a decrease in the intensity of the (6,5)* band.

Figure 1d shows the PL spectrum of the doped SWCNT with the maximum PL signal (25 min of UV exposure, red line), along with the PL spectrum of the pristine SWCNT (blue line). The maximum peak intensity of the (6,5)* band in the PL spectrum of the oxygen-doped SWCNT is more than two times higher than that of the (6,5) band in the PL spectrum of the pristine SWCNT. It should be noted that we performed a control experiment in which SWCNT were irradiated by UV light under the same conditions, but without NaOCl (deionized water instead of NaOCl solution was added to the SWCNT suspension in the same volume), and we did not observe any signs of the (6,5)* and (6,4)* peaks in the PL

spectrum. (yellow reference line in Figure 1d). Further, there were no significant changes in the PL spectrum of SWCNTs after 10 h of interaction with NaOCl at the same concentration without UV exposure. This confirms that both NaOCl and UV light are necessary for effective oxygen doping of the SWCNT.

To additionally characterize the doping reaction and track any possible changes in the morphology of SWCNT in the suspension, we performed UV-vis-NIR optical absorption spectroscopy measurements. Figure 2 compares the optical absorption spectra of the SWCNT suspension before and after doping for different reaction durations. It is seen that both E11 optical transitions in the spectral region of 800–1200 nm and E22 optical transitions in the spectral region 400–800 nm are suppressed though changes in the E11 spectral region are more prominent. A similar effect was previously reported for SWCNT doped with other methods and is commonly explained in terms of the suppression of the exciton oscillator strength due to the depletion of electron states in the valence band of SWCNT [27,28]. In all other aspects, the optical absorption spectrum remains almost unchanged, suggesting the absence of any drastic changes in the SWCNT morphology. Moreover, no changes in the background spectral shape related to scattering indicate a similar suspendability for the pristine and oxygen-doped SWCNT.

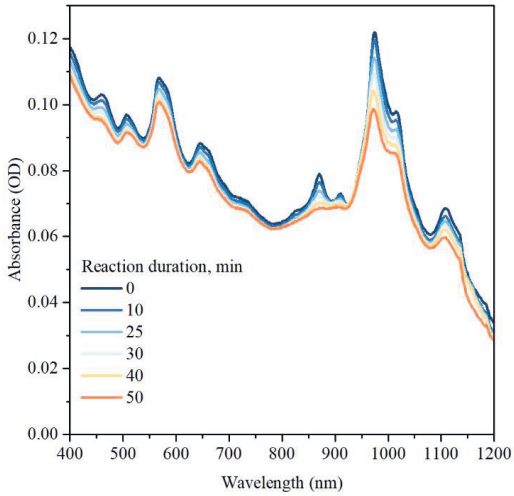

Figure 2. UV-vis-NIR optical absorption spectra of pristine and doped SWCNT.

Now we proceed to the comparison of the achieved PL enhancement with previously published results. The most physically meaningful way to do so is to consider the relative changes in PL quantum yield which might be calculated as:

$$\frac{QY(doped)}{QY(pristine)} = \frac{I_{doped}^{(6,5*)}}{I_{pristine}^{(6,5)}} \quad (1)$$

where $I_{doped}^{(6,5*)}(6,5)^*$—is the integrated intensity of the (6,5)* peak in the spectrum of doped SWCNT and $I_{pristine}^{(6,5)}(6,5)$—is the integrated intensity of the (6,5) peak in the spectrum of *pristine* SWCNT. Applying spectra deconvolution to separate PL peaks and integration (see Figure S2), we estimated that oxygen doping enhances the PL QY by at least 6 ± 0.6 times. Note that this is a lower-bound estimation because formula (1) is accurate for the case of the same optical density of the sample at the excitation wavelength. In fact, the optical density of the sample at 840 nm is slightly decreased due to oxygen doping (see Figure 1d)

meaning that the real enhancement factor of the PL QY is higher than 6. However, a direct comparison of this value with the results published in the literature is not possible because of the lack of published data on spectral deconvolution and integrated peak intensity values.

Instead, we define the PL brightening coefficient ϑ as:

$$\vartheta = \frac{A_{doped}^{(6,5)*}}{A_{pristine}^{(6,5)}} \quad (2)$$

where $A_{doped}^{(6,5*)}$ is the amplitude (maximum intensity) of the (6,5)* band in the PL spectrum of O-doped SWCNTs and $A_{pristine}^{(6,5)}$ is the amplitude of the (6,5) band in the PL spectrum of pristine SWCNT (before doping). The higher ϑ value means the higher $\frac{QY(doped)}{QY(pristine)}$ value, although from a practical point of view, such as the application of O-SWCNTs as IR light emitters, the comparison of ϑ values is more meaningful since it reflects changes in PL brightness under the same excitation conditions. Furthermore, the previously published literature may provide accurate ϑ values that can be extracted from PL spectra.

In this work, we achieved a highly reproducible ϑ value of 2.12 ± 0.11 (Figure 1d). Table 1 compares the ϑ values among all of the published literature on the oxygen doping of SWCNT. As shown in Table 1, our method demonstrates the highest PL emission enhancement.

Table 1. A comparison of the photoluminescence (PL) brightening coefficient ϑ achieved employing oxygen doping of single-walled carbon nanotubes (SWCNT).

Ref.	PL Brightening Coefficient ϑ	Chirality	Synthesis Method and Dealer	Note on O-Doping Method
This work	2.12	(6,5)	CoMoCat, Merk (former Sigma-Aldrich, St. Louis, MO, USA)	NaOCl + light
(Chiu et al.) [29]	1.65	(6,5)	CoMoCat, Sigma-Aldrich	treatment with polyunsaturated fatty acids
(Lin et al.) [25]	1.35	(6,5)	CoMoCat, Sigma-Aldrich	NaOCl + light
(Miyauchi et al.) [21]	0.86	(6,5)	CoMoCat, dealer unknown	O_3 + light
(Ghosh et al.) [20]	0.68	(6,5)	unknown	O_3 + light
(Iwamura et al.) [22]	0.61	(6,5)	CoMoCat, Sigma-Aldrich and Southwest Nanotechnologies (Norman, OK, USA)	O_3 + light
(Iizumi et al.) [4]	0.51	(6,5)	unknown	O_3 + light
(Akizuki et al.) [23]	0.33	(6,5)	CoMoCat, Southwest Nanotechnologies	O_3 + light

4. Discussion

Let us now discuss the reason for such an advanced PL intensity enhancement observed in this work in comparison to the previously published results. Note that the SWCNTs used in this study are similar to those used in most of the papers listed in Table 1, indicating that the reported variance in θ values is mainly caused by the details of the oxygen doping procedure.

The higher ϑ values obtained in this work compared to the previously published results obtained in [4,20–24,29] can easily be ascribed to the principal differences in the employed chemical reactions. Indeed, oxygen doping of SWCNT via ozonization occurs in several steps, including the formation of an ozonide adduct on the surface of SWCNT, subsequent loss of O_2 with the formation of an epoxide adduct, and photoisomerization of the epoxide adduct into either one [20]. Each stage of this reaction occurs on the surface of

the SWCNT and may eventually lead not only to the formation of bright excitonic states but also to the formation of dark trapping defects, thus preventing the conversion of diffusive (6,5) excitons into localized (6,5)* and limiting the resulting PL brightness [13]. In contrast, in the NaOCl-based approach, the formation of oxygen defects on the surface of SWCNT occurs in a single-step reaction of carbon walls with atomic oxygen previously produced at a distance from the SWCNT surface during photodissociation of the hypochlorite ion. This difference in reaction mechanisms explains the higher ratio of bright and dark defects in the case of using NaOCl as an oxygen source, and therefore, higher PL brightening coefficients.

In our study, we used the same doping reaction as in [25], which involves the photodissociation of hypochlorite ions. However, we found that the resulting ϑ values obtained in this work and in [25] vary significantly. To determine the reason for this difference, we utilized Raman spectroscopy to investigate the details of the defect formation during oxygen doping.

The evolution of the Raman spectra is shown in Figure 3a. A gradual decrease in the tangential G-mode intensity was observed during the doping reaction, which is consistent with the changes in the intensity of the (6,5) PL band (Figure 3b). The intensity of the radial breathing mode (RBM) in the Raman spectra also monotonically decreased with increasing UV exposure duration (See Figure S3). Simultaneous suppression of the RBM and G modes in the Raman spectrum can be considered as a fingerprint of the effective doping of SWCNT [30–32]. The absence of other drastic changes in the RBM spectral region of the Raman spectrum during oxygen doping suggests that the morphology of the SWCNT in the sample remains unchanged. Based on the Raman shift of the RBM mode (275 cm^{-1}), we estimated the diameter of the investigated SWCNT as 0.86 nm which is consistent with the data obtained using PL mapping.

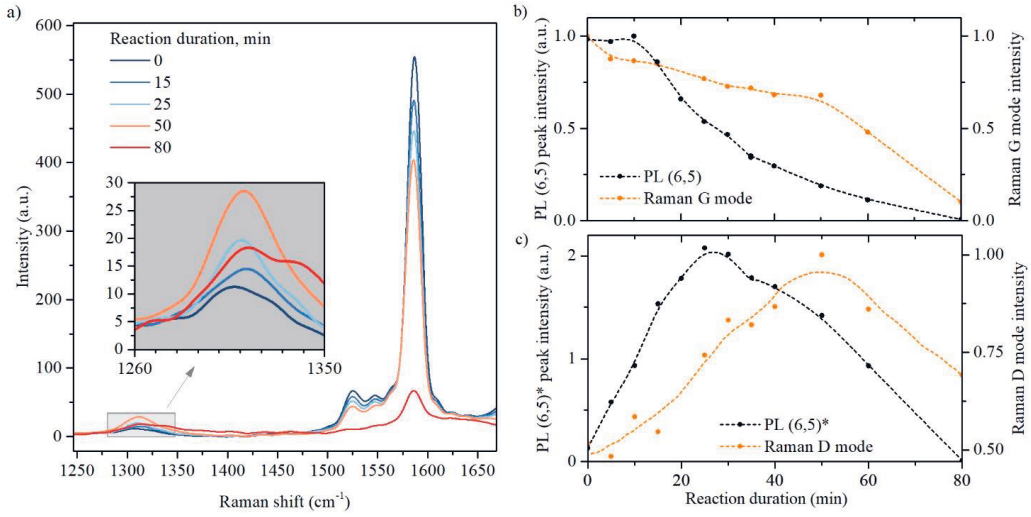

Figure 3. (**a**) Raman spectra of pristine and oxygen-doped SWCNTs; (**b**) the dependence of the PL (6,5) and Raman G-mode intensity on the duration of the doping reaction; (**c**) the dependence of the PL (6,5)* and Raman D-mode intensity on the duration of the doping reaction. Dashed lines are a guide-to-the-eye.

Information about defects formation in SWCNT can be obtained by analyzing the changes in the spectral region of the so-called "defective" (D) mode (inset in Figure 3a). The intensity of the D-mode increased during the first 50 min of the reaction and then began to decrease, resembling the (6,5)* PL peak behavior (Figure 3c). The density of defects in SWCNT can be estimated from the ratio of the integrated intensities of the D and G bands

using the calibration curve reported in [33]. Thus, for moderately doped SWCNT (25 min of UV exposure), the density of oxygen defects is estimated as 30 μm^{-1}.

This observation confirms that the (6,5)* PL peak appears owing to defect formation by the covalent bonding of oxygen atoms to the SWCNTs walls. However, when the UV exposure time exceeded 25 min, the intensity of the (6,5)* peak in the PL spectrum began to decrease, although the intensity of the D-mode continued to increase. This cannot be explained by the amorphization of the SWCNTs crystalline structure due to a large number of oxygen defects because the shapes of the D and G bands do not demonstrate any signs of amorphization until 50 min of UV exposure. Indeed the disruption of the SWCNTs structure progresses only after 50 min of UV illumination, which is accompanied by an abrupt drop in both the D and G band intensities, a sharp increase in the D/G intensity ratio, and distinctive changes in the shape of the D-band in the Raman spectrum (violet line in Figure 3a).

To exclude the suppression of the (6,5)* PL peak due to consumption of NaOCl reactant during the first 25 min [25] we performed addition measurement. By adding an extra portion of non-irradiated NaOCl to the SWCNTs suspension in the middle of the O-doping process (30 min of UV irradiation), we did not reverse the downward trend of the (6,5)* peak intensities versus time of UV irradiation (see Figure S4). This result declines a scarcity of NaOCl reactant as a limiting factor of the (6,5)* peak growth.

We propose that the proximity of O-defects might interfere with the localizing potential and electronic structure of O-doped sites, which may prevent effective radiative emission and thus limit the growth of the (6,5)* peak intensity despite the increase in the total number of oxygen defects. This means that the homogeneity of doping is a critical issue for achieving bright emissions from the O-doped sites of SWCNTs.

This assumption can explain the higher PL brightening coefficient ϑ achieved in this work compared with previously published results. Indeed, the use of prolonged (25 min) and gentle (27 $\mu W/cm^2$) UV exposure in this work should provide more uniform O-doping than in the case of brief (40 s) and rough (29 mW/cm^2) UV exposure, which was applied in [25] and resulted in a striking difference in ϑ value (2.12 in this work and 1.36 in [25] with almost the same D/G intensity ratio).

Employing SWCNT doped with oxygen using NaOCl and prolonged and gentle UV exposure as bioimaging probes may provide better contrast in tissue images than those obtained using conventional methods. In the context of single-photon sources, this approach may provide a higher emission frequency. Nevertheless, for successful industrial applications of O-SWCNT IR light emitters, including bioimaging probes and single-photon emitters, as well as IT LED and IR nanolasers, the brightness of O-SWCNT PL should be further increased. The results obtained in this work suggest an efficient way to do so by adjusting the duration and intensity of UV exposure, thus improving the homogeneity of the SWCNTs O-doping. This approach is a promising way to overcome the brightness of sp_3-doped SWCNTs while maintaining the simplicity and rapidity of O-doping technology.

5. Conclusions

The demonstrated modification of the SWCNT oxygen doping method results in the appearance of a red-shifted PL band with a peak intensity that is more than twice that of the peak intensity of the PL band in the undoped sample. The PL brightening coefficient of 2.12 ± 0.11 obtained in this work is the highest value among all published works using the O-doping approach. The Raman spectroscopy study of defect formation suggests that this is achieved owing to a more homogeneous distribution of oxygen atoms along the SWCNTs due to prolonged and gentle UV exposure. We propose that further optimization of the O-doping method by adjusting the duration and intensity of UV exposure is a promising way to increase the brightness of O-SWCNT photoluminescence while maintaining the other advantages of this approach, such as technological simplicity and rapidity, which satisfy the requirements of technological applications such as IR LEDs, IR nanolasers, IR single-photon sources, and bioimaging probes.

Supplementary Materials: The following supporting information can be downloaded at: https://www.mdpi.com/article/10.3390/nano13091561/s1, Figure S1. PL spectra of pristine and doped SWCNT suspension under excitation wavelength 570 nm.; Figure S2: Deconvolution of PL spectra; Figure S3. Raman spectra of pristine and doped SWCNT in the RBM spectral region.; Figure S4: Control experiment denying consumption of NaOCl as a limiting factor of PL intensity growth.

Author Contributions: Conceptualization, T.E. and P.O.; methodology, T.E. and V.E.; validation, T.E., V.E. and P.O.; formal analysis, T.E.; investigation, T.E. and V.E.; resources, P.O. and Y.S.; data curation, T.E.; writing—original draft preparation, T.E.; writing—review and editing, T.E., V.E., Y.S. and P.O.; visualization, T.E.; supervision, P.O. and Y.S.; project administration, Y.S.; funding acquisition, P.O. All authors have read and agreed to the published version of the manuscript.

Funding: This research was funded by the Academy of Finland (decision numbers 340831 (UPHYPE), 320166 (PREIN Flagship), 346576 and 343393) and Horizon 2020 RISE project DiSeTCom (Project No. 823728).

Institutional Review Board Statement: Not applicable.

Informed Consent Statement: Not applicable.

Data Availability Statement: Publicly available datasets were analyzed in this study. This data can be found here: https://drive.google.com/file/d/156TeiFf7ahVhYjm__CdkiKDSUIpEtHdg/view?usp=sharing (accessed on 3 May 2023).

Conflicts of Interest: The authors declare no conflict of interest. The funders had no role in the design of the study; in the collection, analyses, or interpretation of data; in the writing of the manuscript; or in the decision to publish the results.

References

1. Dresselhaus, M.S.; Dresselhaus, G.; Saito, R.; Jorio, A. Raman Spectroscopy of Carbon Nanotubes. *Phys. Rep.* **2005**, *409*, 47–99. [CrossRef]
2. Weisman, R.B.; Bachilo, S.M. Dependence of Optical Transition Energies on Structure for Single-Walled Carbon Nanotubes in Aqueous Suspension: An Empirical Kataura Plot. *Nano Lett.* **2003**, *3*, 1235–1238. [CrossRef]
3. He, X.; Htoon, H.; Doorn, S.K.; Pernice, W.H.P.; Pyatkov, F.; Krupke, R.; Jeantet, A.; Chassagneux, Y.; Voisin, C. Carbon Nanotubes as Emerging Quantum-Light Sources. *Nat. Mater.* **2018**, *17*, 663–670. [CrossRef]
4. Iizumi, Y.; Yudasaka, M.; Kim, J.; Sakakita, H.; Takeuchi, T.; Okazaki, T. Oxygen-Doped Carbon Nanotubes for near-Infrared Fluorescent Labels and Imaging Probes. *Sci. Rep.* **2018**, *8*, 6272. [CrossRef] [PubMed]
5. Miyauchi, Y. Photoluminescence Studies on Exciton Photophysics in Carbon Nanotubes. *J. Mater. Chem. C* **2013**, *1*, 6499–6521. [CrossRef]
6. Hertel, T.; Himmelein, S.; Ackermann, T.; Stich, D.; Crochet, J. Diffusion Limited Photoluminescence Quantum Yields in 1-D Semiconductors: Single-Wall Carbon Nanotubes. *ACS Nano* **2010**, *4*, 7161–7168. [CrossRef]
7. Dresselhaus, M.S.; Dresselhaus, G.; Saito, R.; Jorio, A. Exciton Photophysics of Carbon Nanotubes. *Annu. Rev. Phys. Chem.* **2007**, *58*, 719–747. [CrossRef]
8. Settele, S.; Berger, F.J.; Lindenthal, S.; Zhao, S.; Ali, A.; Yumin, E.; Zorn, N.F.; Asyuda, A.; Zharnikov, M.; Högele, A.; et al. Synthetic Control over the Binding Configuration of Luminescent Sp3-Defects in Single-Walled Carbon Nanotubes. *Nat. Commun.* **2021**, *12*, 2119. [CrossRef]
9. Gifford, B.J.; Kilina, S.; Htoon, H.; Doorn, S.K.; Tretiak, S. Controlling Defect-State Photophysics in Covalently Functionalized Single-Walled Carbon Nanotubes. *Acc. Chem. Res.* **2020**, *53*, 1791–1801. [CrossRef]
10. Shiraki, T.; Miyauchi, Y.; Matsuda, K.; Nakashima, N. Carbon Nanotube Photoluminescence Modulation by Local Chemical and Supramolecular Chemical Functionalization. *Acc. Chem. Res.* **2020**, *53*, 1846–1859. [CrossRef]
11. He, X.; Sun, L.; Gifford, B.J.; Tretiak, S.; Piryatinski, A.; Li, X.; Htoon, H.; Doorn, S.K. Intrinsic Limits of Defect-State Photoluminescence Dynamics in Functionalized Carbon Nanotubes. *Nanoscale* **2019**, *11*, 9125–9132. [CrossRef]
12. Kim, Y.; Velizhanin, K.A.; He, X.; Sarpkaya, I.; Yomogida, Y.; Tanaka, T.; Kataura, H.; Doorn, S.K.; Htoon, H. Photoluminescence Intensity Fluctuations and Temperature-Dependent Decay Dynamics of Individual Carbon Nanotube Sp^3 Defects. *J. Phys. Chem. Lett.* **2019**, *10*, 1423–1430. [CrossRef]
13. Gifford, B.J.; He, X.; Kim, M.; Kwon, H.; Saha, A.; Sifain, A.E.; Wang, Y.; Htoon, H.; Kilina, S.; Doorn, S.K.; et al. Optical Effects of Divalent Functionalization of Carbon Nanotubes. *Chem. Mater.* **2019**, *31*, 6950–6961. [CrossRef]
14. Sykes, M.E.; Kim, M.; Wu, X.; Wiederrecht, G.P.; Peng, L.; Wang, Y.H.; Gosztola, D.J.; Ma, X. Ultrafast Exciton Trapping at Sp3 Quantum Defects in Carbon Nanotubes. *ACS Nano* **2019**, *13*, 13264–13270. [CrossRef] [PubMed]
15. Nutz, M.; Zhang, J.; Kim, M.; Kwon, H.; Wu, X.; Wang, Y.; Högele, A. Photon Correlation Spectroscopy of Luminescent Quantum Defects in Carbon Nanotubes. *Nano Lett.* **2019**, *19*, 7078–7084. [CrossRef] [PubMed]

16. Piao, Y.; Meany, B.; Powell, L.R.; Valley, N.; Kwon, H.; Schatz, G.C.; Wang, Y. Brightening of Carbon Nanotube Photoluminescence through the Incorporation of Sp^3 Defects. *Nat. Chem.* **2013**, *5*, 840–845. [CrossRef] [PubMed]
17. He, X.; Hartmann, N.F.; Ma, X.; Kim, Y.; Ihly, R.; Blackburn, J.L.; Gao, W.; Kono, J.; Yomogida, Y.; Hirano, A.; et al. Tunable Room-Temperature Single-Photon Emission at Telecom Wavelengths from Sp^3 Defects in Carbon Nanotubes. *Nat. Photonics* **2017**, *11*, 577–582. [CrossRef]
18. Saha, A.; Gifford, B.J.; He, X.; Ao, G.; Zheng, M.; Kataura, H.; Htoon, H.; Kilina, S.; Tretiak, S.; Doorn, S.K. Narrow-Band Single-Photon Emission through Selective Aryl Functionalization of Zigzag Carbon Nanotubes. *Nat. Chem.* **2018**, *10*, 1089–1095. [CrossRef] [PubMed]
19. Ma, X.; Adamska, L.; Yamaguchi, H.; Yalcin, S.E.; Tretiak, S.; Doorn, S.K.; Htoon, H. Electronic Structure and Chemical Nature of Oxygen Dopant States in Carbon Nanotubes. *Nat. Nanotechnol.* **2015**, *7*, 126–132. [CrossRef]
20. Ghosh, S.; Bachilo, S.M.; Simonette, R.A.; Beckingham, K.M.; Weisman, R.B. Oxygen Doping Modifies Near-Infrared Band Gaps in Fluorescent Single-Walled Carbon Nanotubes. *Science* **2010**, *330*, 1656–1659. [CrossRef]
21. Miyauchi, Y.; Iwamura, M.; Mouri, S.; Kawazoe, T.; Ohtsu, M.; Matsuda, K. Brightening of Excitons in Carbon Nanotubes on Dimensionality Modification. *Nat. Photonics* **2013**, *7*, 715–719. [CrossRef]
22. Iwamura, M.; Akizuki, N.; Miyauchi, Y.; Mouri, S.; Shaver, J.; Ga, Z.; Cogne, L.; Louni, B.; Matsuda, K.; Gao, Z.; et al. Nonlinear Photoluminescence Spectroscopy of Carbon Nanotubes with Localized Exciton States. *ACS Nano* **2014**, *8*, 11254–11260. [CrossRef] [PubMed]
23. Akizuki, N.; Aota, S.; Mouri, S.; Matsuda, K.; Miyauchi, Y. Efficient Near-Infrared up-Conversion Photoluminescence in Carbon Nanotubes. *Nat. Commun.* **2015**, *6*, 8920. [CrossRef]
24. Shiraishi, T.; Juhász, G.; Shiraki, T.; Akizuki, N.; Miyauchi, Y.; Matsuda, K.; Nakashima, N. Determination of Precise Redox Properties of Oxygen-Doped Single-Walled Carbon Nanotubes Based on in Situ Photoluminescence Electrochemistry. *J. Phys. Chem. C* **2016**, *120*, 15632–15639. [CrossRef]
25. Lin, C.W.; Bachilo, S.M.; Zheng, Y.; Tsedev, U.; Huang, S.; Weisman, R.B.; Belcher, A.M. Creating Fluorescent Quantum Defects in Carbon Nanotubes Using Hypochlorite and Light. *Nat. Commun.* **2019**, *10*, 2874. [CrossRef]
26. Pagani, G.; Green, M.J.; Poulin, P.; Pasquali, M. Competing Mechanisms and Scaling Laws for Carbon Nanotube Scission by Ultrasonication. *Proc. Natl. Acad. Sci. USA* **2012**, *109*, 11599–11604. [CrossRef]
27. Eremin, T.V.; Obraztsov, P.A.; Velikanov, V.A.; Shubina, T.V.; Obraztsova, E.D. Many-Particle Excitations in Non-Covalently Doped Single-Walled Carbon Nanotubes. *Sci. Rep.* **2019**, *9*, 14985. [CrossRef]
28. Hartleb, H.; Spath, F.; Hertel, T. Evidence for Strong Electronic Correlations in the Spectra of Gate-Doped Single-Wall Carbon Nanotubes. *ACS Nano* **2015**, *9*, 10461–10470. [CrossRef]
29. Chiu, C.F.; Saidi, W.A.; Kagan, V.E.; Star, A. Defect-Induced Near-Infrared Photoluminescence of Single-Walled Carbon Nanotubes Treated with Polyunsaturated Fatty Acids. *J. Am. Chem. Soc.* **2017**, *139*, 4859–4865. [CrossRef]
30. Eremin, T.; Obraztsova, E. Optical Properties of Single-Walled Carbon Nanotubes Doped in Acid Medium. *Phys. Status Solidi* **2017**, *255*, 1700272. [CrossRef]
31. Fedotov, P.V.; Tonkikh, A.A.; Obraztsova, E.A.; Nasibulin, A.G.; Kauppinen, E.I.; Chuvilin, A.L.; Obraztsova, E.D. Optical Properties of Single-Walled Carbon Nanotubes Filled with CuCl by Gas-Phase Technique. *Phys. Status Solidi* **2014**, *251*, 2466–2470. [CrossRef]
32. Kalbac, M.; Kavan, L.; Dunsch, L. Changes in the Electronic States of Single-Walled Carbon Nanotubes as Followed by a Raman Spectroelectrochemical Analysis of the Radial Breathing Mode. *J. Phys. Chem. C* **2008**, *112*, 16759–16763. [CrossRef]
33. Sebastian, F.L.; Zorn, N.F.; Settele, S.; Lindenthal, S.; Berger, F.J.; Bendel, C.; Li, H.; Flavel, B.S.; Zaumseil, J. Absolute Quantification of Sp^3 Defects in Semiconducting Single-Wall Carbon Nanotubes by Raman Spectroscopy. *J. Phys. Chem. Lett.* **2022**, *13*, 3542–3548. [CrossRef] [PubMed]

ARTICLE III

Eremin, T., Dhama, R., Caglayan, H., & Obraztsov, P. (2024). Ultrafast exciton trapping dynamics in oxygen-functionalized single-walled carbon nanotubes. *Carbon*, 220, 118837.

Carbon 220 (2024) 118837

Contents lists available at ScienceDirect

Carbon

journal homepage: www.elsevier.com/locate/carbon

Ultrafast exciton trapping dynamics in oxygen-functionalized single-walled carbon nanotubes

Timofei Eremin [a,*], Rakesh Dhama [b], Humeyra Caglayan [b], Petr Obraztsov [a]

[a] Department of Physics and Mathematics, Center for Photonics Sciences, University of Eastern Finland, Yliopistokatu 2, 80101, Joensuu, Finland
[b] Faculty of Engineering and Natural Science, Photonics, Tampere University, 33720, Tampere, Finland

ARTICLE INFO

Keywords:
Single-walled carbon nanotubes
Exciton trapping
pump−probe spectroscopy
Zero-dimensional quantum defects

ABSTRACT

Artificial zero-dimensional quantum defects within single-walled carbon nanotubes hold immense promise for diverse optoelectronic applications such as bioimaging, near-infrared light emission, nanolasing, and single-photon generation. This study delves into the temporal behavior of excitons within oxygen-functionalized single-walled carbon nanotubes, employing ultrafast transient absorption spectroscopy. Our investigation unveils the emergence of functionalization-induced excitonic states, distinguished by a long-lasting induced transmittance signal. Remarkably, even at low degree of functionalization, we observe a reduction in the lifetime of band-edge excitons. In contrast, the population dynamics of deep-band excitons exhibit resilience against low and moderate functionalization degrees, with a pronounced reduction manifesting only at high degrees of functionalization. Our findings align closely with a kinetic model that accounts for an additional relaxation channel prompted by functionalization. This empirical evidence provides a significant breakthrough, establishing that the formation of functionalization-induced excitonic states within oxygen-functionalized single-walled carbon nanotubes is a consequence of the diffusive trapping of free band edge excitons, while interaction of deep band excitons with oxygen defect sites rather yields in exciton recombination. These insights shed light on the intricate dynamics of excitons within single-walled carbon nanotube with artificially embedded quantum defects, advancing our understanding and potential applications in the realm of optoelectronics.

1. Introduction

Covalent functionalization of single-walled carbon nanotubes (SWCNTs) offers a way to fine-tune their electronic structure and optical properties, enabling various applications in photonics and optoelectronics. Recent research indicates that introducing specific artificial defects into the structure of SWCNTs leads to the emergence of new optically active excitonic states that are energetically downshifted compared to the ordinary free diffusive exciton E_{11} of pristine SWCNTs [1,2]. These functionalization-induced excitons, often referred to as E_{11}*, exhibit significantly brighter red-shifted photoluminescence (PL) emissions, hinting at their potential suitability as compact on-chip infrared light emitters [3,4]. Also, the photoluminescence emission of E_{11}* excitons in covalently functionalized SWCNTs shows less spectral overlap with the optical absorption bands as compared to the case of pristine SWCNTs, making covalently functionalized SWCNTs promising candidates as bioimaging probes [5]. Furthermore, single-photon emission is another exciting application of covalently functionalized SWCNTs, which has even been demonstrated at room temperature [6–8]. Additionally, it is also possible to design nanolasers based on SWNTs utilizing a three-level structure, where the finctionalization-induced excitonic state E_{11}* serves as the emitting level and one of the higher-energy pristine excitonic states (E_{11} or E_{22}) is used for pumping.

There are two main approaches to engineering artificial emissive defects in SWCNTs. The first approach is usually referred to as sp^3 functionalization and involves attaching a large functional group (aryl, alkyl etc.) to a carbon atom on the SWCNT surface [2,7,9–16]. This attachment changes the hybridization of the carbon atom from sp^2 to sp^3 without breaking the C–C bonds with the surrounding carbon atoms. The second approach is based on introducing oxygen atoms that bridge between two adjacent carbon atoms in the SWCNT lattice, with or without breaking the C–C bond, depending on the specific defect configuration [1,5,17–25]. While most research is focused on sp^3-functionalized SWCNTs (sp^3-SWCNTs) due to their tendency to provide brighter emission, some recent studies have demonstrated the promising potential of a technologically simple oxygen-functionalization method

* Corresponding author.
E-mail address: timofei.eremin@uef.fi (T. Eremin).

https://doi.org/10.1016/j.carbon.2024.118837
Received 27 October 2023; Received in revised form 31 December 2023; Accepted 15 January 2024
Available online 21 January 2024

Abbreviations

SWCNTs	single-walled carbon nanotubes
NIR	near-infrared
PL	photoluminescence
TA	transient absorption
OPA	optical parametric amplifier
UV	ultraviolet
SDS	sodium dodecyl sulfate

to create emissive defects [4,5]. This method holds perspectives for further improving the final brightness of SWCNTs and poses a worthy competition to the sp^3 approach. Additionally, oxygen-functionalized SWCNTs (O-SWCNTs) hold more promise for bioimaging than sp^3-SWCNTs, as functionalization-induced excitons in O-SWCNTs are less absorptive, resulting in less spectral overlap between emission and absorption bands [5].

Successful industrial applications of the advanced physical properties of SWCNTs with quantum defects demand a deep understanding of fundamental processes, such as the conversion of ordinary exciton states E_{11} and E_{22} to the functionalization-induced excitonic state E_{11}^*, including the formation and recombination dynamics of these states. Over the last decade, persistent efforts have been made to unveil these topics. Investigations utilizing time-resolved photoluminescence (TR PL) spectroscopy have demonstrated that the lifetime of functionalization-induced excitons in sp^3-SWCNTs is on the order of several tens of picoseconds, significantly higher than the measured lifetime of pristine band-edge excitons, while the lifetime of band-edge excitons is shortened in sp^3-SWCNTs compared to pristine SWCNTs [12, 14,15,26] These observations have been considered as an evidence that functionalization-induced excitons are localized in the vicinity of artificial defects and populate as a result of the diffusive trapping of free band-edge excitons. Investigations of sp^3-SWCNTs employing ultrafast transient absorption (TA) spectroscopy have allowed the examination of this hypothesis at shorter timescales and reaffirmed that the exciton trapping channel in sp^3-SWCNTs leads to the formation of defect-localized excitons [13]. Notably, similar phenomena were also observed in non-covalently doped SWCNT, where the potential is modified due to physiosorbed charges [27–29].

The understanding of exciton dynamics in SWCNTs functionalized through the widely used and promising approach of oxygen functionalization is currently not as well-established as in the case of sp^3-SWCNTs. To date, only one published study has investigated the time-domain behavior of excitons in O-SWCNTs [25]. That study utilized TR PL spectroscopy, revealing that in O-SWCNTs, the lifetime of excitons induced by functionalization is significantly longer compared to the lifetime of free excitons. This behavior is reminiscent of what is observed in sp^3-SWCNTs. However, no significant impact of oxygen functionalization on the lifetime of free excitons themselves was reported [25]. This lack of observation may be attributed to limitations in the time resolution of the equipment used. Therefore there is currently no available data on the ultrafast exciton dynamics in O-SWCNTs. Consequently, there has been no thorough investigation into whether the emissive excitonic states induced by functionalization in O-SWCNTs are defect-localized in nature and whether they are populated through the diffusive trapping of free excitons. Furthermore, none of the published studies have explored the impact of embedding artificial defects on the dynamics of E_{22} excitons. This is relevant for both sp^3-and O- functionalization, with existing research primarily focusing on changes in the E_{11} exciton manifold.

In this paper, we address a critical knowledge gap in the field of exciton dynamics within O-SWCNTs using ultrafast pump-probe spectroscopy. Our study reveals several unprecedented phenomena in O-SWCNTs, including a gradual reduction in the lifetime of the free band-edge E_{11} exciton and abrupt changes in the deep-band E_{22} exciton lifetime as degree of functionalization increase. Additionally, we report a previously unobserved red-shifted functionalization-induced transmittance signal as a consequence of embedding of oxygen defects in SWCNTs, attributed to the emergence of a novel excitonic state E_{11}^*. Our analysis of the interplay between E_{11}^*, E_{11}, and E_{22} exciton dynamics and their dependency on degree of functionalization provides valuable insights. Particularly, we find that E_{11}^* states are formed during the trapping of diffusive E_{11} excitons, while interaction of E_{22} excitons with defects site yields in exciton recombination rather than trapping. These findings significantly advance our understanding of formation and population of defect-trapped excitonic states. This knowledge is pivotal for developing a comprehensive framework for defect state photophysics and their potential applications in photonics.

2. Materials and methods

Sample preparation. SWCNT powder with predominant (6,5) chirality was purchased from Merk (Product No. 773735). Water suspensions of high optical quality we prepared by dissolving SWCNT in 2 % SDS solution in a primary concentration of 0.1 mg/mL followed by ultrasonication (4h, suspension volume 50 mL, integrated power 200W, on/off cycle ratio 0.1). Detailed description of oxygen functionalization procedure [4] and underlying mechanism of chemical reaction might be found elsewhere [5]. In brief, the SWCNT suspension was first mixed with a water solution of NaOCl, and then it was exposed to UVC irradiation for a duration ranging from 5 to 50 min. The concentration of SWCNTs in suspensions prepared for oxygen functionalization step is estimated as 0.1 mg/L based on the absorbance at E_{11} transition (Fig. 1).

Ultrafast transient absorption spectroscopy: Ultrafast time-resolved pump-probe spectroscopy *measurements* were conducted by employing an amplified Ti: sapphire laser system equipped with an optical parametric amplifier (OPA). This system generated 100 fs (fs) pulses at a frequency of 1.00 kHz (kHz) with a central wavelength of 800 nm. Most of the output (approximately 90 %) was directed towards the OPA to generate tunable pump pulses spanning the UV–Visible to near-infrared spectral ranges, to excite the samples at the desired wavelengths. The pump wavelength for all the measurements was set to 400 nm, and the energy density in the pulse is estimated as 1.5 mJ/cm^2. The remaining 10 % of the output power was sent towards the delay-line to allow the precise control of the time delay between the pump and probe pulses and transformed into a broadband probe beam to interrogate the dispersed SWCNTs at normal incidence in transmission mode. At the same time, the chopper-modulated pump pulse was spatially as well as temporally overlapped with the probe beam on the samples. Meanwhile, the detector is triggered to detect every probe pulse and calculate the absorption spectrum. Repetition rates of the pump and probe beams turn out to be 500 Hz and 1 kHz, respectively. Consequently, the effect of the pump beam will be observed only in one of the two consecutive probe beams.

3. Results and discussion

The effectiveness of oxygen functionalization of SWCNT was verified by changes observed in the PL and Raman spectra of SWCNT. After the oxygen-functionalization procedure, a new emissive band appeared at 1130 nm in the PL spectrum (see Fig. 1a), indicating alterations in the excitonic structure of SWCNT. Additionally, a rise of D mode in the Raman spectrum (Fig. 1b) indicated the formation of oxygen defects in the crystalline structure of SWCNT sidewalls. The degree of functionalization was controlled by the duration of functionalization reaction. The integrated intensity of D mode in the Raman spectra was used to estimate the density of embedded defects on SWCNTs according to the calibration curve reported in Ref. [30]. Alternations in steady-state optical absorption spectrum are shown in Fig. 1c.

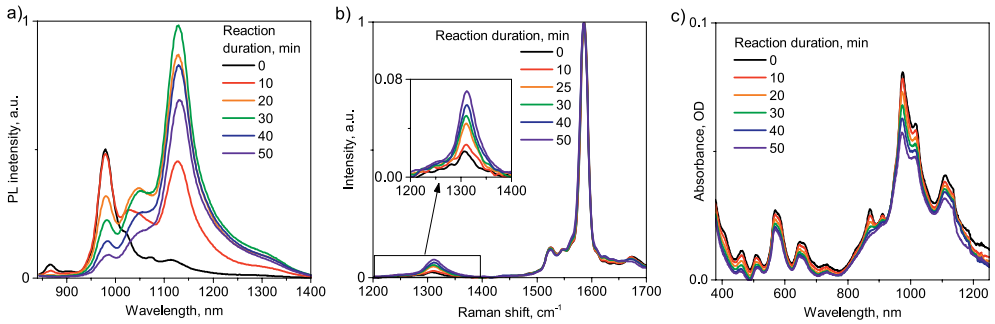

Fig. 1. PL(a) and Raman(b) spectra of pristine SWCNT suspension (black line) and oxygen-functionalized SWCNT (red line). The excitation wavelengths are 565 nm for PL measurements and 532 nm for Raman measurements.

Fig. 2 presents two-dimensional color map of TA in the pristine SWCNT suspension, with probe wavelength covering the NIR and visible spectral regions and the pump wavelength set to 400 nm. Induced transmittance (negative TA) spectral features corresponding to exciton population in SWCNT of different chiralities are denoted with dashed lines and the E_{ii}(n,m) notations, in which (n,m) refer to SWCNT chirality while subscripts ii defines the type of excitonic transition (E_{11} for the band-edge and E_{22} for the deep-band excitons) [31]. The assignment of chiral indexes (n,m) to the TA features is done according to the previously published photoluminescence data [4]. One can also observe other basic TA features of SWCNTs, such as the biexciton formation signal at ~1060 nm, which we leave beyond the scope of this study. In the present research, we focus on the SWCNTs of the predominant chirality (6,5) which provide the most intensive photo response. These nanotubes are characterized by induced transmittance features centered at 980 nm and 565 nm, corresponding to E_{11} and E_{22} excitonic transitions [32]. The population dynamics of E_{11} and E_{22} can be obtained as a time dependence of measured TA signal at corresponding wavelengths. We note that this remains valid even considering that TA response of SWCNTs in E_{11} spectral region is actually a superposition of spectrally shifted positive and negative TA signals since the ratio of amplitudes of these signal does not demonstrate strong time dependence [33,34].

Fig. 3a and b depict the dependence of the induced transmittance signal at specific wavelengths (980 and 565 nm, respectively) on the time delay between the pump and probe pulses for suspensions of SWCNTs with varying density of embedded oxygen-defects (distinguished by different durations of the oxygen-functionalization reaction). These figures illustrate the influence of oxygen functionalization on the population dynamics of E_{11} and E_{22} excitons. Notably, the dynamics of E_{11} undergo adverse alterations even at low degrees of functionalization, whereas the dynamics of E_{22} remains almost unchanged until the duration of functionalization exceeds 25 min.

We shift our focus to quantitative characterization of the changes in the dynamics of E_{11} and E_{22} excitons. Previously it was shown by Sykes et al. that the ultrafast dynamics of excitons in sp^3-SWCNTs can be adequately modeled by global analysis of the entire spectral range considering several decay channels of different natures, including first-order exciton decay, exciton-exciton annihilation, Auger recombination, and trapping by defects etc. [13] While this approach is effective for monochiral SWCNT suspensions, the presence of SWCNTs with different chiralities renders it impractical due to a significantly increased number of fitting parameters. To address this challenge, we propose a simplified approach according to which the exciton dynamics in oxygen-functionalized SWCNTs are considered as a convolution of the complex exciton dynamics in pristine SWCNTs and a hypothetical functionalization-induced exciton relaxation channel as follows:

$$N_{11}^{d}(t) = A_{11} * e^{-\frac{t}{\tau_{11}}} + (1 - A_{11}) * N_{11}^{p}(t) \quad (1)$$

$$N_{22}^{d}(t) = A_{22} * e^{-\frac{t}{\tau_{22}}} + (1 - A_{22}) * N_{22}^{p}(t) \quad (2)$$

Here, t represents the time delay between the pump and probe pulses. $N_{nn}^{d}(t)$ denotes the population dynamics of E_{nn} excitons in O-SWCNT, while $N_{nn}^{p}(t)$ represents the population dynamics of E_{nn} excitons in pristine SWCNT. The fitting parameters, A_{nn} and τ_{nn} capture the contribution and lifetime, respectively, of an additional decay channel resulting from oxygen functionalization. The factor $(1 - A_{nn})$ signifies the reduction in the relative contribution of decay channels typical for pristine SWCNTs due to oxygen functionalization. We note that our usage of a model considering an exponential law of exciton decay rather than the power law is in alignment with prior literature. Indeed, the power decay law was reported for ultrapure monochiral SWCNT suspensions [34], while exponential decay law is more typical for the SWCNT samples processing several SWCNT chiralities [35–37].

By employing this model to fit the experimental data on exciton dynamics, we have determined the values of fitting parameters A_{nn} and τ_{nn} for SWCNTs with varying degrees of oxygen functionalization (refer

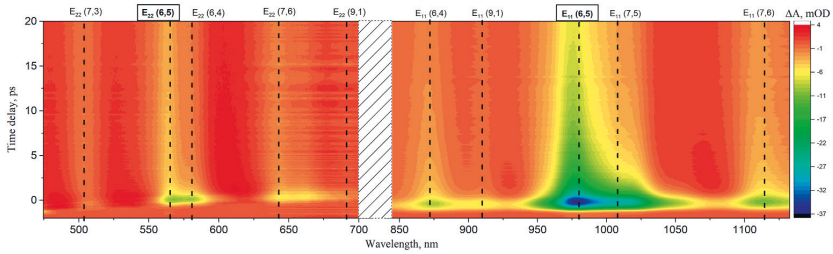

Fig. 2. Two-dimensional color maps illustrating the dependence of the pump-induced TA in the suspension of pristine SWCNT on the probe wavelength and time delay between the pump and probe pulses. E_{ii} (n,m) notations refers to SWCNT's chirality and type of optical transition. Pump wavelength is 400 nm.

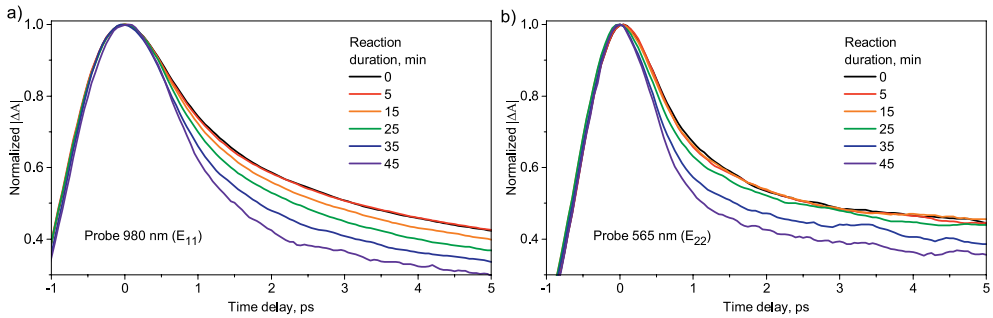

Fig. 3. Kinetic profiles at 980 nm (a) and 565 nm (b) probe wavelengths for SWCNT and O-SWCNT with different degree of oxygen functionalization. Pump wavelength is 400 nm.

to Fig. S2 for representative fitting results). Fig. 4a and b depict the dependencies of the relative contributions A_{nn} and the lifetime τ_{22} of the functionalization-induced decay channel on the duration of the reaction. Notably, striking differences emerge in the evolution of the additional decay channel for E_{11} and E_{22} excitons. Specifically, for the E_{11} exciton case, the amplitude A_{11} of the additional decay channel consistently increases from the start of the reaction. On the other hand, the functionalization-induced decay channel in the dynamics of the E_{22} exciton only becomes active after approximately 25–30 min of the reaction, followed by an increase. The lifetime of the additional decay channel exhibits a step-like dependence on the degree of functionalization. At low degree of functionalization, when the amplitude of the functionalization-induced decay channel is negligibly small, the lifetime remains in the order of several picoseconds, reflecting minimal impact on the dynamics. However, once the additional channel is activated, its lifetime decreases, fluctuating within the range of 400–600 fs for the E_{11} exciton and 100–150 fs for the E_{22} exciton.

We suggest that the alterations observed in the dynamics of E_{11} and E_{22} excitons, as the degree of functionalization varies, can be attributed to the interaction between diffusive excitons and oxygen defects, resulting in the emergence of a functionalization-induced decay channel. This explanation finds support in the distinct behaviors of E_{11} and E_{22} excitons. E_{22} excitons initially possess a rapid relaxation channel to the energetically lower E_{11} state through phonon scattering [38]. However, due to their belonging to the lowest exciton manifold of pristine SWCNTs, E_{11} excitons do not experience fast phonon relaxation and can diffuse over longer distances along SWCNTs. Consequently, at low degree of functionalization, photoexcited excitons are more likely to reach oxygen defects while in the E_{11} state than in the E_{22} state. In contrast, at high degrees of functionalization, the proximity of oxygen defects becomes so pronounced that diffusive E_{22} excitons have a greater likelihood of reaching the defects before they relax to the E_{11} manifold. These considerations offer a qualitative explanation for why the amplitude of the functionalization-induced channel of E_{11} excitons starts to increase at lower degrees of functionalization compared to the activation of the functionalization-induced decay channel of E_{22} excitons (see Fig. 4). This reasoning supports attributing the functionalization-induced channel to the interaction between diffusive excitons and oxygen defects.

The interaction of excitons with defects may lead to the shortening of exciton lifetimes, either through exciton trapping by defective potentials or exciton recombination induced by scattering on the defects. To determine which of these processes takes place, we analyzed the evolution of TA spectra with the increasing degree of functionalization at fixed pump-probe delay times of 0 and 10 ps (Fig. 5a and b respectively). It can be observed that at zero delay time (see Fig. 5a), the amplitude of the TA signal decreases monotonically with rising degree of functionalization. Importantly, this is relevant for the entire spectrum, encompassing excitonic transitions in SWCNTs of all chiralities (see insert at Fig. 5a). At a delay time of 10 ps the suppression of excitonic transitions is also noticeable with increasing degree of functionalization. However, this pattern doesn't extend to the region of 1100–1170 nm, where some changes in the shape of the band and even a rise in the induced transmittance signal with the reaction duration are observed (see insert at Fig. 5b).

This indicates the appearance of a new functionalization-induced negative TA spectral feature, which we denote as E_{11}*, within the 1100–1170 nm region. However, this feature partially overlaps with the spectral feature of the E_{11} excitonic transition in (7,6)-SWCNT, centered at 1115 nm (see Fig. 2). To extract the signal of the functionalization-induced spectral feature, we conducted subtraction of the signal arising from (7,6)-SWCNT (while accounting of the impact of

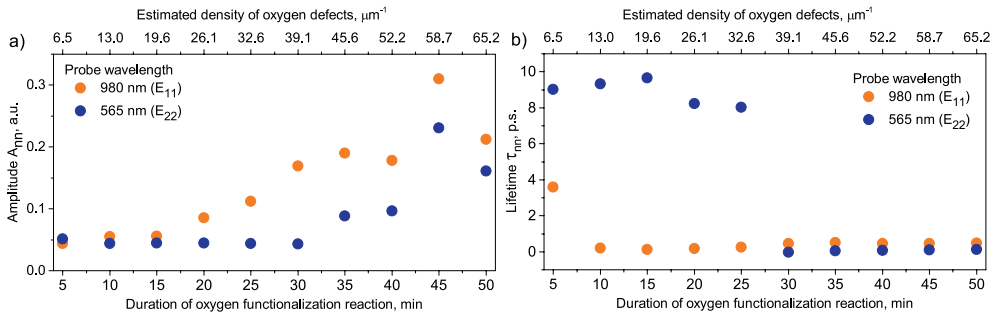

Fig. 4. Evaluated amplitudes (a) and lifetimes (b) of the functionalization-induced decay channel of E_{11} (orange) and E_{22} (blue) excitons in dependence on the duration of the functionalization reaction. Density of oxygen defects is estimated according to [29].

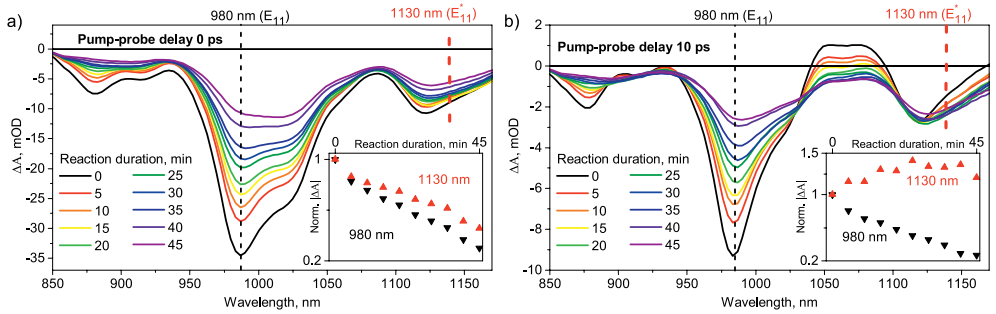

Fig. 5. TA spectra of SWCNT suspensions with varying degree of oxygen functionalization at 0 ps (a) and 10 ps (b) of time delay between probe and pump pulses. Pump wavelength is 400 nm. Inserts: dependence of the normalized amplitudes of the TA signals at 980 nm and 1130 nm.

functionalization on its dynamics) from the measured data.

Fig. 6a displays a two-dimensional color plot of the evaluated E_{11}^* spectral feature, which is centered around 1130 nm, aligning with the emission wavelength of the functionalization-induced PL band observed in the PL spectra of O-SWCNTs (see Fig. 1a) [1,4,5,24,25]. We note that there is no sign of a corresponding peak around 1130 nm in steady-state absorption spectra of oxygen-functionalized SWCNT (see Fig. 1c). This is one of the key distinctions between O-SWCNT and sp^3-SWCNT, since sp^3-SWCNTs exhibit a distinct red-shifted absorption peak in steady-state absorption spectra [3,9,10], whereas works dedicated to O-SWCNTs do not report observation of such a peak [1,22,25]. Similarly, a distinct E_{11}^* spectral feature in TA spectra of sp^3-SWCNTs was previously observed by Sykes et al. [13], but up to now, there have been no reports concerning this issue in O-SWCNT. We thus cover this knowledge gap by observation of E_{11}^* spectral feature in TA spectra of O-SWCNT (see Fig. 6a). It is also worth mentioning that the E_{11}^* spectral feature exhibits time-domain characteristics similar to those previously reported for defect-localized excitons (see Fig. 6b): a formation time on the order of several picoseconds, akin to what was unveiled by pump-probe spectroscopy of sp^3- SWCNTs [13], and a decay time on the order of several tens or hundreds of picoseconds, akin to that uncovered by time-resolved PL spectroscopy of both O-SWCNTs and sp^3-SWCNTs [12,14,15,26]. These observations indicate that E_{11}^* spectral feature corresponds to the formation of excitons localized by the deep trap potentials of oxygen defects.

The dependence of E_{11}^* spectral feature amplitude on the duration of functionalization reaction provides valuable insights concerning differences in the interaction of E_{11} and E_{22} excitons with embedded oxygen defects. (see Fig. 6b). The E_{11}^* amplitude increases with the rising degree of oxygen functionalization until the duration of the reaction reaches 30 min (see Fig. 6b). At the same time, as was previously discussed and demonstrated in Figs. 3 and 4, these degrees of functionalization yield in shortening of E_{11} exciton lifetime with no sufficient impact on the E_{22} exciton lifetime. These observations lead us to the conclusion that the functionalization-induced decay channel in the dynamics of E_{11} arises from exciton trapping, resulting in the subsequent population of the defect-localized excitonic state E_{11}^*. We also note that when the degree of functionalization becomes high enough to impact the dynamics of E_{22} excitons (duration of the reaction exceeds 30 min, see Figs. 3 and 4), the dependence of the amplitude of E_{11}^* spectral feature on the degree of functionalization changes its trend demonstrating weak decrease instead of rise. (see Fig. 6b). This observation indicates that trapping of deep-band E_{22} excitons is much less effective than the trapping of band-edge E_{11} excitons. The shortening of the lifetime of E_{22} exciton with increasing degree of functionalization thus can be attributed to exciton recombination via scattering on oxygen defects similar to exciton quenching on natural nonradiative defects [39]. We assume that these unexpected differences in the interaction of E_{11} and E_{22} excitons with oxygen defect sites, which were not addressed in prior literature, are due to differences in the exciton wave functions and spectra of excitonic states in E_{11} and E_{22} manifolds [31].

The findings we present in this study hold significant implications for the practical applications of SWCNTs with artificially embedded quantum defects, including nanolasers, single-photon sources, LEDs, and bioimaging probes. Particularly, when designing devices like these based on SWCNTs, the precise selection of the concentration and distribution of quantum defects within the SWCNT structure emerges as a critical determinant of achieving optimal performance. Our discovery of the mechanism governing the population of level E_{11}^* during the capture of excitons unveils that the ideal density of quantum defects is intricately linked to the mean free path of excitons E_{11} and E_{22}. Furthermore, this relationship can be influenced by a range of factors, including the

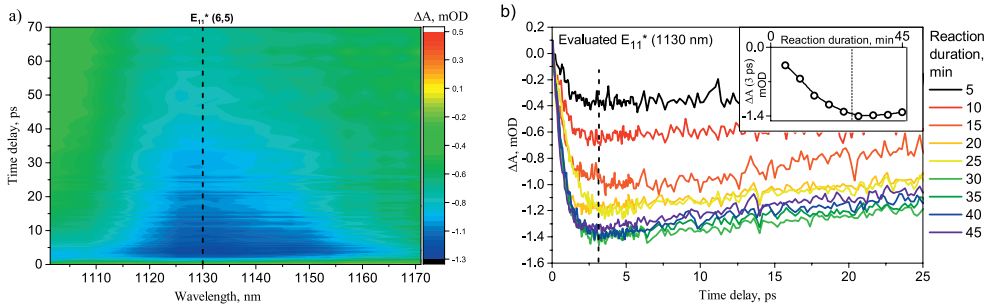

Fig. 6. a) Two-dimensional color map of evaluated TA signal corresponding to E_{11}^* exciton population in oxygen doped SWCNT (reaction duration25 min). b) evaluated dynamics of E_{11}^* exciton in SWCNT with different oxygen doping levels. Inset: dependence of the amplitude of E_{11}^* feature at the delay of ps on the duration of the functionalization reaction.

SWCNT's diameter, local environment, the presence of non-emissive defects, SWCNT length, and more. These complex interdependencies underscore the necessity for a nuanced and comprehensive approach when customizing functionalized SWCNTs for specific applications.

4. Conclusions

In this study, we delved into the intricacies of exciton dynamics within O-SWCNT by employing ultrafast pump-probe spectroscopy. We report the emergence of defect-localized excitonic states, distinguished by their long-lasting induced transmittance spectral features with a pronounced red-shift. We demonstrated that the population of these excitonic states is primarily a consequence of the trapping of diffusive band-edge E_{11} excitons by oxygen defects. Concurrently, we made the intriguing discovery that the interaction between deep band E_{22} excitons and defect sites occurs predominantly at high degrees of functionalization and yields in exciton recombination rather that exciton trapping.

These findings not only broaden our understanding of the intricate processes of exciton diffusion and trapping within SWCNTs featuring quantum defects but also hold immense promise for practical applications. Specifically, they provide a solid foundation for the development of O-SWCNTs for use in infrared light-emitting diodes, bioimaging probes, and single-photon emitters.

Role of the funding source

The sponsors did not influence the study's design, data collection, analysis, data interpretation, manuscript preparation, or the decision to publish the findings.

CRediT authorship contribution statement

Timofei Eremin: Conceptualization, Data curation, Formal analysis, Investigation, Software, Visualization, Writing – original draft, Writing – review & editing, Methodology. **Rakesh Dhama:** Data curation, Investigation, Methodology, Resources, Validation, Writing – review & editing. **Humeyra Caglayan:** Funding acquisition, Methodology, Project administration, Resources, Supervision, Validation, Writing – review & editing. **Petr Obraztsov:** Conceptualization, Funding acquisition, Investigation, Methodology, Project administration, Resources, Supervision, Validation, Writing – review & editing.

Declaration of competing interest

The authors declare that they have no known competing financial interests or personal relationships that could have appeared to influence the work reported in this paper.

Acknowledgements

This research was funded by the Academy of Finland (project UPHYPE (340831, 346576), PREIN Flagship (320165, 320166)), H2020 Programme (RISE project Chartist (101007896), MSCA TERASSE (823878)), Horizon 2020 ERC Starting Grant project aQUARiUM (802986).

Appendix A. Supplementary data

Supplementary data to this article can be found online at https://doi.org/10.1016/j.carbon.2024.118837.

References

[1] S. Ghosh, S.M. Bachilo, R.A. Simonette, K.M. Beckingham, R.B. Weisman, Oxygen doping modifies near-infrared band gaps in fluorescent single-walled carbon nanotubes, Science 330 (2010) 1656–1659, https://doi.org/10.1126/science.1196382.

[2] T. Shiraki, T. Shiraishi, G. Juhász, N. Nakashima, Emergence of new red-shifted carbon nanotube photoluminescence based on proximal doped-site design, Sci. Rep. 6 (2016) 28393, https://doi.org/10.1038/srep28393.

[3] Y. Piao, B. Meany, L.R. Powell, N. Valley, H. Kwon, G.C. Schatz, Y. Wang, Brightening of carbon nanotube photoluminescence through the incorporation of sp 3 defects, Nat. Chem. 5 (2013) 840–845, https://doi.org/10.1038/nchem.1711.

[4] T. Eremin, V. Eremina, Y. Svirko, P. Obraztsov, Over two-fold photoluminescence enhancement from single-walled carbon nanotubes induced by oxygen doping, Nanomaterials 13 (2023), https://doi.org/10.3390/nano13091561.

[5] C.W. Lin, S.M. Bachilo, Y. Zheng, U. Tsedev, S. Huang, R.B. Weisman, A.M. Belcher, Creating fluorescent quantum defects in carbon nanotubes using hypochlorite and light, Nat. Commun. 10 (2019), https://doi.org/10.1038/s41467-019-10917-3.

[6] A. Högele, C. Galland, M. Winger, A. Imamoğlu, Photon antibunching in the photoluminescence spectra of a single carbon nanotube, Phys. Rev. Lett. 100 (2008) 5–8, https://doi.org/10.1103/PhysRevLett.100.217401.

[7] X. He, N.F. Hartmann, X. Ma, Y. Kim, R. Ihly, J.L. Blackburn, W. Gao, J. Kono, Y. Yomogida, A. Hirano, T. Tanaka, H. Kataura, H. Htoon, S.K. Doorn, Tunable room-Temperature single-photon emission at telecom wavelengths from sp 3 defects in carbon nanotubes, Nat. Photonics 11 (2017) 577–582, https://doi.org/10.1038/nphoton.2017.119.

[8] A. Saha, B.J. Gifford, X. He, G. Ao, M. Zheng, H. Kataura, H. Htoon, S. Kilina, S. Tretiak, S.K. Doorn, Narrow-band single-photon emission through selective aryl functionalization of zigzag carbon nanotubes, Nat. Chem. 10 (2018) 1089–1095, https://doi.org/10.1038/s41557-018-0126-4.

[9] S. Settele, F.J. Berger, S. Lindenthal, S. Zhao, A. Ali, E. Yumin, N.F. Zorn, A. Asyuda, M. Zharnikov, A. Högele, J. Zaumseil, Synthetic control over the binding configuration of luminescent sp3-defects in single-walled carbon nanotubes, Nat. Commun. (2021) 1–10, https://doi.org/10.1038/s41467-021-22307-9.

[10] W. Zheng, N.F. Zorn, M. Bonn, J. Zaumseil, H.I. Wang, Probing carrier dynamics in sp3-functionalized single-walled carbon nanotubes with time-resolved terahertz spectroscopy, ACS Nano 16 (2022) 9401–9409, https://doi.org/10.1021/acsnano.2c02199.

[11] B.J. Gifford, S. Kilina, H. Htoon, S.K. Doorn, S. Tretiak, Controlling defect-state photophysics in covalently functionalized single-walled carbon nanotubes, Acc. Chem. Res. 53 (2020) 1791–1801, https://doi.org/10.1021/acs.accounts.0c00210.

[12] Y. Kim, K.A. Velizhanin, X. He, I. Sarpkaya, Y. Yomogida, T. Tanaka, H. Kataura, S. K. Doorn, H. Htoon, Photoluminescence intensity fluctuations and temperature-dependent decay dynamics of individual carbon nanotube sp ^{3} defects, J. Phys. Chem. Lett. 10 (2019) 1423–1430, https://doi.org/10.1021/acs.jpclett.8b03732.

[13] M.E. Sykes, M. Kim, X. Wu, G.P. Wiederrecht, L. Peng, Y.H. Wang, D.J. Gosztola, X. Ma, Ultrafast exciton trapping at sp3 quantum defects in carbon nanotubes, ACS Nano 13 (2019) 13264–13270, https://doi.org/10.1021/acsnano.9b06279.

[14] X. He, K.A. Velizhanin, G. Bullard, Y. Bai, J.-H. Olivier, N.F. Hartmann, B. J. Gifford, S. Kilina, S. Tretiak, H. Htoon, M.J. Therien, S.K. Doorn, Solvent- and wavelength-dependent photoluminescence relaxation dynamics of carbon nanotube sp ^{3} defect states, ACS Nano (2018), https://doi.org/10.1021/acsnano.8b02909 acsnano.8b02909.

[15] N.F. Hartmann, K.A. Velizhanin, E.H. Haroz, M. Kim, X. Ma, Y. Wang, H. Htoon, S. K. Doorn, Photoluminescence dynamics of aryl sp3 defect states in single-walled carbon nanotubes, ACS Nano 10 (2016) 8355–8365, https://doi.org/10.1021/acsnano.6b02986.

[16] N.F. Hartmann, S.E. Yalcin, L. Adamska, E.H. Hároz, X. Ma, S. Tretiak, H. Htoon, S. K. Doorn, Photoluminescence imaging of solitary dopant sites in covalently doped single-wall carbon nanotubes, Nanoscale 7 (2015) 20521–20530, https://doi.org/10.1039/c5nr06343d.

[17] N. Akizuki, S. Aota, S. Mouri, K. Matsuda, Y. Miyauchi, Efficient near-infrared up-conversion photoluminescence in carbon nanotubes, Nat. Commun. 6 (2015) 1–6, https://doi.org/10.1038/ncomms9920.

[18] X. Ma, J.K.S. Baldwin, N.F. Hartmann, S.K. Doorn, H. Htoon, Solid-state approach for fabrication of photostable, oxygen-doped carbon nanotubes, Adv. Funct. Mater. 25 (2015) 6157–6164, https://doi.org/10.1002/adfm.201502580.

[19] X. Ma, L. Adamska, H. Yamaguchi, S.E. Yalcin, S. Tretiak, S.K. Doorn, H. Htoon, Electronic structure and chemical nature of oxygen dopant states in carbon nanotubes, Nat. Nanotechnol. 7 (2015) 1–6, https://doi.org/10.1038/nnano.2011.227.

[20] T. Shiraishi, G. Juhász, T. Shiraki, N. Akizuki, Y. Miyauchi, K. Matsuda, N. Nakashima, Determination of precise redox properties of oxygen-doped single-walled carbon nanotubes based on in situ photoluminescence electrochemistry, J. Phys. Chem. C 120 (2016) 15632–15639, https://doi.org/10.1021/acs.jpcc.5b07841.

[21] C.F. Chiu, W.A. Saidi, V.E. Kagan, A. Star, Defect-induced near-infrared photoluminescence of single-walled carbon nanotubes treated with polyunsaturated fatty acids, J. Am. Chem. Soc. 139 (2017) 4859–4865, https://doi.org/10.1021/jacs.7b00390.

[22] Y. Iizumi, M. Yudasaka, J. Kim, H. Sakakita, T. Takeuchi, T. Okazaki, Oxygen-doped carbon nanotubes for near-infrared fluorescent labels and imaging probes, Sci. Rep. 8 (2018) 1–6, https://doi.org/10.1038/s41598-018-24399-8.

[23] F.J. Berger, Luminescent Defects in Polymer-Wrapped Carbon Nanotubes, 2021.

[24] M. Iwamura, N. Akizuki, Y. Miyauchi, S. Mouri, J. Shaver, Z. Ga, L. Cogne, B. Louni, K. Matsuda, Z. Gao, L. Cognet, B. Lounis, K. Matsuda, Y. Ohno, S. Maruyama, M. Takashi, M. Iwamura, N. Akizuki, Y. Miyauchi, S. Mouri, J. Shaver, Z. Gao, L. Cognet, B. Lounis, K. Matsuda, Z. Ga, L. Cogne, B. Louni, K. Matsuda, Nonlinear photoluminescence spectroscopy of carbon nanotubes with localized exciton states, ACS Nano 8 (2014) 11254–11260, https://doi.org/10.1021/nn503803b.

[25] Y. Miyauchi, M. Iwamura, S. Mouri, T. Kawazoe, M. Ohtsu, K. Matsuda, Brightening of excitons in carbon nanotubes on dimensionality modification, Nat. Photonics 7 (2013) 715–719, https://doi.org/10.1038/nphoton.2013.179.
[26] X. He, L. Sun, B.J. Gifford, S. Tretiak, A. Piryatinski, X. Li, H. Htoon, S.K. Doorn, Intrinsic limits of defect-state photoluminescence dynamics in functionalized carbon nanotubes, Nanoscale 11 (2019) 9125–9132, https://doi.org/10.1039/c9nr02175b.
[27] T.V. Eremin, P.A. Obraztsov, V.A. Velikanov, T.V. Shubina, E.D. Obraztsova, Many-particle excitations in non-covalently doped single-walled carbon nanotubes, Sci. Rep. 9 (2019) 1–8, https://doi.org/10.1038/s41598-019-50333-7.
[28] Y. Bai, J.-H. Olivier, G. Bullard, C. Liu, M.J. Therien, C. Liu, G. Bullard, J.-H. Olivier, Dynamics of charged excitons in electronically and morphologically homogeneous single-walled carbon nanotubes, Proc. Natl. Acad. Sci. USA 115 (2018) 674, https://doi.org/10.1073/pnas.1712971115, 679.
[29] K.H. Eckstein, P. Kunkel, M. Voelckel, F. Sch, T. Hertel, Trions, Exciton Dynamics, and Spectral Modifications in Doped Carbon Nanotubes: A Singular Defect-Driven Mechanism, 2023, https://doi.org/10.1021/acs.jpcc.3c04889.
[30] F.L. Sebastian, N.F. Zorn, S. Settele, S. Lindenthal, F.J. Berger, C. Bendel, H. Li, B. S. Flavel, J. Zaumseil, Absolute Quantification of Sp 3 Defects in Semiconducting Single- Wall Carbon Nanotubes by Raman Spectroscopy, 2022, https://doi.org/10.1021/acs.jpclett.2c00758.
[31] M.S. Dresselhaus, G. Dresselhaus, R. Saito, A. Jorio, Exciton photophysics of carbon nanotubes, Annu. Rev. Phys. Chem. 58 (2007) 719–747, https://doi.org/10.1146/annurev.physchem.58.032806.104628.
[32] R.B. Weisman, S.M. Bachilo, Dependence of optical transition energies on structure for single-walled carbon nanotubes in aqueous suspension: an empirical Kataura plot, Nano Lett. 3 (2003) 1235–1238, https://doi.org/10.1021/nl034428i.
[33] L. Lüer, G. Lanzani, J. Crochet, T. Hertel, J. Holt, Z.V. Vardeny, Ultrafast dynamics in metallic and semiconducting carbon nanotubes, Phys. Rev. B Condens. Matter 80 (2009) 4–8, https://doi.org/10.1103/PhysRevB.80.205411.
[34] Z. Zhu, J. Crochet, M.S. Arnold, M.C. Hersam, H. Ulbricht, D. Resasco, T. Hertel, Pump-probe spectroscopy of exciton dynamics in (6,5) carbon nanotubes, J. Phys. Chem. C 111 (2007) 3831–3835, https://doi.org/10.1021/jp0669411.
[35] G.N. Ostojic, S. Zaric, J. Kono, M.S. Strano, V.C. Moore, R.H. Hauge, R.E. Smalley, Interband recombination dynamics in resonantly excited single-walled carbon nanotubes, Phys. Rev. Lett. 92 (2004) 117402–1, https://doi.org/10.1103/PhysRevLett.92.117402.
[36] L. Huang, H.N. Pedrosa, T.D. Krauss, Ultrafast ground-state recovery of single-walled carbon nanotubes, Phys. Rev. Lett. 93 (2004) 1–4, https://doi.org/10.1103/PhysRevLett.93.017403.
[37] D.J. Styers-Barnett, S.P. Ellison, B.P. Mehl, B.C. Westlake, R.L. House, C. Park, A. Kristopher E Wise, J.M. Papanikolas, Exciton dynamics and biexciton formation in single-walled carbon nanotubes studied with femtosecond transient absorption spectroscopy, J. Phys. Chem. C 112 (2008) 4507–4516, https://doi.org/10.1021/jp7099256.
[38] A.R. Amori, Z. Hou, T.D. Krauss, Excitons in single-walled carbon nanotubes and their dynamics, Annu. Rev. Phys. Chem. 69 (2018) 81–99, https://doi.org/10.1146/annurev-physchem-050317-014241.
[39] D.K. Singh, P.K. Giri, P.K. Iyer, Evidence for defect-enhanced photoluminescence quenching of fluorescein by carbon nanotubes, J. Phys. Chem. C 115 (2011) 24067–24072, https://doi.org/10.1021/jp207392d.

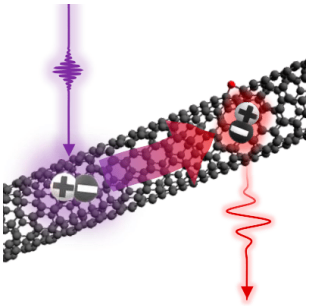

TIMOFEI EREMIN

Single-walled carbon nanotubes hold great promise for applications in optoelectronics, telecommunications, and quantum technologies due to their broad light emission and absorption capabilities. However, their low photoluminescence efficiency remains a significant challenge. This thesis focuses on enhancing photoluminescence brightness by localizing photoexcited excitons in artificial traps within the nanotubes, investigating the energy level structures of these traps, and examining exciton-trap interactions on the sub-picosecond timescale.

UNIVERSITY OF
EASTERN FINLAND

uef.fi

PUBLICATIONS OF
THE UNIVERSITY OF EASTERN FINLAND
Dissertations in Science, Forestry and Technology

ISBN 978-952-61-5368-1
ISSN 2954-131X